

THE ROLE OF SINGLY-CHARGED PARTICLES IN MICROELECTRONICS  
RELIABILITY

By

Brian Sierawski

Dissertation

Submitted to the Faculty of the  
Graduate School of Vanderbilt University  
in partial fulfillment of the requirements  
for the degree of

DOCTOR OF PHILOSOPHY

in

Electrical Engineering

December, 2011

Nashville, Tennessee

Approved:

Ronald D. Schrimpf

Robert A. Reed

Marcus H. Mendenhall

Robert A. Weller

James H. Adams

© Copyright by Brian Sierawski 2012

All Rights Reserved

## DEDICATION

This dissertation is dedicated to my family in appreciation of their support and patience. To my wife Heather, thank you for your sacrifice during my academic pursuits. Your important and sometimes unseen role in my accomplishments has been substantial. To my children Carter and Jenna, I hope that my efforts inspire you to use your abilities to the fullest. To my parents David and Patricia and my brother Jeff, thank you for the beginnings of what has turned out to be a rewarding career in electronics.

## ACKNOWLEDGEMENTS

I would like to acknowledge the individuals and agencies that have made this research possible. My committee members have been valuable resources in guiding the data collection, simulation, and analysis performed in this dissertation. My coworkers at the Institute for Space and Defense Electronics including Kevin Warren and Michael Alles have also provided valuable conversations. Further, Jonathan Pellish and Ken LaBel with the NASA Electronic Parts and Packaging Program and the Defense Threat Reduction Agency and have provided much appreciated support to pursue this topic. I would like to thank our corporate partners for their contributions namely Robert Baumann at Texas Instruments, Shi-Jie Wen and Richard Wong at Cisco Systems, and Nelson Tam at Marvell Semiconductor. Finally, Michael Trinczek and Ewart Blackmore from TRIUMF also provided exceptional experimental support that was essential to this research.

## TABLE OF CONTENTS

	Page
DEDICATION . . . . .	iii
ACKNOWLEDGEMENTS . . . . .	iv
LIST OF TABLES . . . . .	viii
LIST OF FIGURES . . . . .	ix
Chapter	
I. INTRODUCTION . . . . .	1
High-Reliability Applications . . . . .	2
Quantitative Assessment of Reliability . . . . .	4
Requirements on Reliability . . . . .	5
SEU Mechanisms . . . . .	6
Mitigation . . . . .	9
Background Work . . . . .	10
Trend in Single Event Sensitivity . . . . .	17
The Onset of Proton Direct Ionization Upsets . . . . .	19
Conclusions . . . . .	21
II. PHYSICAL PROCESSES . . . . .	22
Electronic Interactions . . . . .	23
Electronic Stopping . . . . .	23
Electron Stripping . . . . .	25
Range . . . . .	26
Nuclear Interactions . . . . .	27
Coulomb Scattering . . . . .	28
Nuclear Elastic Scattering . . . . .	28
Nuclear Inelastic Scattering . . . . .	29
Spallation . . . . .	29
Pion Production . . . . .	29
Capture . . . . .	30
Decay . . . . .	30
Pion Decay . . . . .	30
Muon Decay . . . . .	31
Conclusions . . . . .	31

III. RADIATION ENVIRONMENTS . . . . .	33
Extraterrestrial Environments . . . . .	34
Interplanetary Space . . . . .	34
Near Earth . . . . .	36
Terrestrial Environments . . . . .	40
Neutron Component . . . . .	43
Proton Component . . . . .	43
Muon Component . . . . .	44
Conclusions . . . . .	46
IV. ACCELERATED TESTING . . . . .	48
Devices Under Test . . . . .	50
Heavy Ion Accelerated Tests . . . . .	51
Accelerated Test Setup . . . . .	51
Accelerated Test Results . . . . .	52
Proton Accelerated Testing . . . . .	55
Accelerated Test Setup . . . . .	55
Accelerated Test Results . . . . .	56
Muon Accelerated Testing . . . . .	61
Accelerated Test Setup . . . . .	61
Experimental Validation . . . . .	64
Accelerated Test Results . . . . .	66
Effect of technology . . . . .	69
Hardness Assurance Methods . . . . .	72
Recommendations . . . . .	72
Low-Energy Proton Testing with a Cyclotron . . . . .	77
Conclusions . . . . .	79
V. RATE PREDICTION ANALYSES . . . . .	82
Traditional Approaches . . . . .	82
TCAD and SPICE Analysis . . . . .	83
Radiation Transport Modeling . . . . .	86
Single Event Upset Predictions . . . . .	91
Proton Response . . . . .	91
Rate Predictions . . . . .	93
Conclusions . . . . .	97
VI. IMPLICATIONS FOR FUTURE DEVICES . . . . .	99
Charge Collection Models . . . . .	102
On-Orbit Single Event Upsets . . . . .	104
Terrestrial Single Event Upsets . . . . .	107
Conclusions . . . . .	112

VII. CONCLUSIONS . . . . .	113
APPENDIX A: EXPACS GENERATED FLUX SPECTRA . . . . .	116
REFERENCES . . . . .	126

## LIST OF TABLES

Table	Page
1. Physical properties for singly-charged particles . . . . .	23
2. Coulomb Barrier Potentials for Common Semiconductor Materials . . . . .	29
3. Device Under Test . . . . .	50
4. Baseline error counts characterized versus bias for 65 nm SRAM . . . . .	51
5. Texas Instruments 65 nm Experimental Ion Species and Energies . . . . .	52
6. Texas Instruments 45 nm Experimental Ion Species and Energies . . . . .	52
7. Facilities Offering Muon Sources . . . . .	61
8. Single event upset counts for 65 nm SRAM . . . . .	70
9. Critical Charge Estimates . . . . .	86
10. Positive Muon Flux at Sea Level in NYC . . . . .	116
11. Negative Muon Flux at Sea Level in NYC . . . . .	118
12. Proton Flux at Sea Level in NYC . . . . .	120
13. Neutron Flux at Sea Level in NYC . . . . .	122

## LIST OF FIGURES

Figure	Page
1. Circuit level schematic diagram of a six transistor SRAM . . . . .	7
2. Cross sectional device level view of an inverter . . . . .	7
3. RC equivalent model used to explain a single event transient . . . . .	8
4. Estimated error rates for devices . . . . .	12
5. The differential flux of cosmic rays transported through 10 cm of concrete	13
6. Prediction of device upset rates . . . . .	14
7. Critical charge trend with technology scaling . . . . .	18
8. The trend in SRAM single bit SER as a function of technology node . .	19
9. Single event upset counts for low-energy protons . . . . .	20
10. Mass stopping power for protons, pions, muons, and positrons in Si . .	25
11. Range in Si for protons, pions, muons, and positrons . . . . .	27
12. The Near-Earth Interplanetary particle flux spectra during solar minimum	35
13. The Near-Earth Interplanetary particle flux spectra during solar maximum	36
14. The Near-Earth Interplanetary particle flux spectra during the worst day scenario . . . . .	37
15. AP8MIN omnidirectional proton flux with energy $\geq 0.1$ MeV . . . . .	39
16. The International Space Station particle flux spectra . . . . .	39
17. Illustration of cosmic ray interactions in the atmosphere generating showers of daughter particles . . . . .	41
18. Sea level environment . . . . .	42
19. Correlation between the solar activity and counts reported by the Climax Neutron Monitor and Nagoya Muon Station [69]. . . . .	44
20. Differential proton momentum spectrum at sea level . . . . .	45
21. Differential muon momentum spectrum at sea level . . . . .	45

22.	The rate of stopping muons measured at various depth underground . . . . .	47
23.	Heavy ion single event upset cross sections for the Texas Instruments 65 nm SRAM measured at LBNL and TAMU. . . . .	53
24.	Heavy ion single event upset cross sections for the Texas Instruments 45 nm SRAM measured at LBNL . . . . .	54
25.	The low-energy proton spectrum at the Lawrence Berkeley National Laboratory . . . . .	57
26.	Simulated kinetic energy spectra . . . . .	58
27.	Texas Instruments 65 nm SRAM in the beam line at Lawrence Berkeley National Laboratories . . . . .	58
28.	Proton single event upset cross-section curve for the Texas Instruments 65 nm SRAM . . . . .	60
29.	Proton single event upset cross-section curve for the Texas Instruments 45 nm SRAM . . . . .	60
30.	The surface muon momentum produced by the M20B beamline at TRIUMF	62
31.	The M20 beam line at TRIUMF . . . . .	63
32.	The Texas Instruments 65 nm SRAM in the M20B beamline at TRIUMF	64
33.	The surface barrier detector in the M20B beamline at TRIUMF . . . . .	65
34.	Experimental and simulated energy deposition counts in surface barrier detector . . . . .	66
35.	Simulated muon kinetic energy distributions and measured error counts for 65 nm, 45 nm, and 40 nm SRAMs . . . . .	68
36.	Error counts for 65 nm SRAM versus supply voltage . . . . .	69
37.	Experimental muon-induced single event upset probability for each device under test operated at nominal supply voltage . . . . .	71
38.	A comparison of experimental and calculated mass stopping power for hydrogen on silicon. . . . .	73
39.	Simulated kinetic energy spectra of a 65 MeV proton beam after degrading	78
40.	Prediction of measured proton SEU cross sections using various degraders in a 65 MeV beam . . . . .	80
41.	TCAD model of a 65 nm bulk CMOS SRAM . . . . .	84

42. Heavy ion single event upset cross sections measured at LBNL and TAMU	88
43. The weighted sensitive volume model used to model the response of a 65 nm CMOS SRAM cell . . . . .	90
44. Simulated single event upset cross sections of a 65 nm SRAM cell as a function of collected charge . . . . .	91
45. Simulated and experimental proton cross sections of a 65 nm SRAM cell	92
46. Events causing single event upsets in a 65 nm SRAM cell for 1.4, 4.6, and 32.5 MeV incident protons . . . . .	92
47. Simulated 65 nm SRAM error rate as a function of critical charge for CREME96 International Space Station orbit, AP8MIN, magnetic quiet, solar minimum, with 100 mils of aluminum shielding . . . . .	94
48. Simulated 65 nm SRAM error rate as a function of critical charge for CREME96 geosynchronous orbit, worst day, with 100 mils of aluminum shielding . . . . .	95
49. Simulated 65 nm SRAM error rate as a function of critical charge for CREME96 geosynchronous orbit, solar minimum, with 100 mils of aluminum shielding . . . . .	96
50. Simulated 65 nm SRAM error rate due to direct ionization from protons as a function of critical charge for CREME96 International Space Station orbit, AP8MIN, magnetic quiet, solar minimum, with 100, 400, and 1000 mils of aluminum shielding . . . . .	97
51. Three dimensional device model used to investigate the charge collection depth for a bulk FinFET drain . . . . .	103
52. Device simulation results for single event strike into fin . . . . .	104
53. Estimated worst day proton dE/dx error rate versus critical charge curves for 32, 22, and 16 nm bulk CMOS representative sensitive volumes . . .	105
54. Estimated worst day proton dE/dx error rate versus critical charge curves for 32, 22, and 16 nm bulk FinFET representative sensitive volumes . .	106
55. Estimated worst day proton dE/dx error rate versus critical charge curves for 32, 22, and 16 nm SOI representative sensitive volumes . . . . .	106
56. Estimated NYC muon-induced error rate versus critical charge curves for 32, 22, and 16 nm bulk CMOS representative sensitive volumes . .	109
57. Estimated NYC proton-induced error rate versus critical charge curves for 32, 22, and 16 nm bulk CMOS representative sensitive volumes . .	109

58. Estimated NYC muon-induced error rate versus critical charge curves for 32, 22, and 16 nm bulk FinFET representative sensitive volumes . .	110
59. Estimated NYC proton-induced error rate versus critical charge curves for 32, 22, and 16 nm bulk FinFET representative sensitive volumes . .	110
60. Estimated NYC muon-induced error rate versus critical charge curves for 32, 22, and 16 nm SOI representative sensitive volumes . . . . .	111
61. Estimated NYC proton-induced error rate versus critical charge curves for 32, 22, and 16 nm SOI representative sensitive volumes . . . . .	111

# CHAPTER I

## INTRODUCTION

In this dissertation, I propose that the emergence of direct-ionization induced single event upsets from singly-charged particles will significantly contribute to the error rate of deep-submicron microelectronics operating in nearly all environments. The implication of this susceptibility will be an additional source of errors in microelectronics along with those currently anticipated by rate prediction methods. The objective of this work is to advance the methods and models to address this mechanism.

In the remainder of Chapter I the issues of reliability, single event effects, and previous published works are discussed. The history of microelectronics susceptibility to ionizing radiation is recounted beginning with the predictions by reliability pioneers that singly-charged particles would one day represent an insurmountable obstacle to continued progress in the fabrication of microelectronics. Chapter II addresses matters of energy loss from ionizing radiation specifically focusing on the processes that are of relevance to single event effects. Chapter III reviews the radiation environments in which microelectronics are deployed. Chapter IV details the experimental procedures performed and results obtained that demonstrate ionization in semiconductor materials from a singly-charged particle, namely a proton or muon, can cause errors in memories. By extension, these events will also be capable of producing effects in other types of sequential circuits and logic. Experimental results are used to develop a model for single event upset in Chapter V. The implications of this increased sensitivity inherently introduced by improvements in fabrication and lithography are

examined in Chapter VI.

As a result of these data and analyses, it is recommended that future high-reliability microelectronics be evaluated for their susceptibility to erroneous operation from singly-charged particles. Such an undertaking will require experience with these mechanisms and support from proton facilities. In addition, the development of methods will be required to advise on matters of testing. To complete the analyses, suitable models or procedures must be proposed to evaluate a part's use in space or on Earth based on results obtained in accelerated environments.

### High-Reliability Applications

The reliability of microelectronics such as memories, controllers, etc. is a primary concern for terrestrial and space applications. The natural ionizing radiation environment poses a significant threat to the operation of these devices. The interactions of ionizing radiation with the materials constituting a solid state device can cause parametric shifts in operation, destructive failures, or transient errors. Under the umbrella of radiation effects, the interaction of individual radiation quanta with electronics is termed single event effects (SEE). These are events which result in the transient or catastrophic failure of a solid-state device. One effect, termed a single event upset (SEU) occurs as the result of radiation-induced charge carriers that cause a sequential circuit to change data state. Single event effects on-orbit have been attributed to heavy ions and proton-induced nuclear reaction events. In terrestrial environments, neutrons and alpha emitting contaminants have been associated with errors. In particular, static random access memories (SRAMs), registers, latches, and flip-flops are all vulnerable to SEU. Following an upset the altered circuit's state may

be propagated, but not necessarily recognized, as an erroneous data or control value.

High-reliability applications place stringent requirements on the frequency of SEU. These requirements are often motivated by acceptable levels of risk and the cost of operating in an otherwise unprotected manner. Modern devices have increased packing density and speed, decreased power dissipation and capacitance, and are more cost effective than previous generations. The same trends in device scaling that these applications leverage are the cause of increased susceptibility to upset.

Satellites and exploration vehicles, costing hundreds of millions of dollars each, are exposed to a wide range of ionizing particle species and energies in space. Certain systems such as data collection may permit the occasional corruption of data; however, errors in critical systems such as control could result in mission failure. These high budget missions have the luxury of funding and using radiation tolerant devices when required. Even so, commercial-off-the-shelf (COTS) electronics are appealing to designers as an avenue to reduce mass, volume, power, and ultimately the cost of launching and operating the satellite. However, Bendel and Petersen, both well known individuals in the radiation effects community once made the forward-looking statement that

*A device sensitive to the ionization in a proton track would be grossly unfit for spacecraft use.[1]*

Suborbital aviation systems use COTS parts more heavily than their orbiting counterparts. Because of cost, the aerospace industry faces the challenge of selecting parts that have been designed for other applications and still ensuring reliable operation. Historically, avionic design has ignored SEE and assumed that the level of

fault tolerance built into the system will prevent calamity. However, recent reports of in-flight anomalies in avionics have captured the attention of the industry.

Computing servers, routers, and communication systems provide the backbone for commerce and other critical systems to modern society. The proliferation of these systems and the increased reliance placed on them underscores our need for them to operate correctly. Expectations for these commodity parts to work flawlessly put pressure on designing resilient systems. It is therefore important to understand and anticipate the SEU mechanisms and to have the capability to test for these effects in a manner that yields accurate predictions of the field failure rate.

### Quantitative Assessment of Reliability

One metric of reliability is the frequency at which a part will fail. For many systems this is expressed as the mean time between failures (MTBF). Reliability can also be expressed as the inverse of MTBF, the number of failures in a specified time period. The particular unit of reporting varies with the community.

For space-bound parts, the error rates are typically expressed as the number of upsets per bit per day in memories, or more generally as upsets per device per day. This may also be calculated on shorter time periods to evaluate the instantaneous error rate observed when encountering periods of high particle flux.

The terrestrial semiconductor community has adopted the unit of FIT (Failures in Time) or failures per 1 billion hours of operation. Memory devices are often normalized to their (Mbit) capacity. This is colloquially referred to as the soft error rate.

These values are only valid under the associated operating conditions and radiation

environment. A useful relationship to bridge the two communities is:

$$1 \text{ FIT/Mbit} = 2.4 \times 10^{-14} \text{ upsets/bit/day} \quad (1)$$

### Requirements on Reliability

As part of NASA's single event effects criticality analysis (SEECA) on spacecraft, different parts of the craft have different reliability requirements according to the risk presented to the mission. In [2], LaBel et al. make the following recommendation for space-faring vehicles that are using commercial off-the-shelf (COTS) components.

"Wherever practical, procure SEU immune devices. In devices which are not SEU-immune, the improper operation caused by an SEU must be reduced to acceptable levels, and may not cause performance anomalies or outages which require ground intervention to correct. Additionally, analysis for SEU rates and effects must take place based on the experimentally determined  $\text{LET}_{\text{th}}$  and  $\sigma$  of the candidate; if such device test data does not exist, ground testing is required."

LaBel et al. also note in [3] that while the test documents such as the JEDEC standards [4, 5] are good guidelines, the increase in device complexity has introduced new phenomena and traditional approaches to testing must be updated to reflect this. Further, as of yet, there are no such guidelines for proton or muon testing.

The International Technology Roadmap for Semiconductors (ITRS) is a forward looking assessment of the direction of the fabrication process with emphasis on identifying challenges and establishing requirements [6]. The reliability requirements are

implicitly provided for terrestrial environments. In reports prior to the 2009 edition, the SRAM soft error rate requirement was indicated as 1000-2000 FIT/Mbit (although 2006 and prior years were not properly normalized by capacity). The 2009 edition inexplicably increases the error rate to 11,000 FIT/Mbit. The relevant value, of course, is ultimately determined by the application.

### SEU Mechanisms

A single event upset occurs as the result of carrier generation near an active region of a sequential circuit. The mechanisms of energy deposition and charge generation will be covered in Chapter II, whereas this chapter discusses the circuit effects. Although upsets can occur in any type of sequential circuit, the following descriptions of the mechanism will be discussed for an SRAM cell without any loss of generality. The six transistor (6T) SRAM cell is one of the most basic sequential circuits. Figure 1 captures the basic design. The cell stores a logic value in a feedback loop maintained by a pair of coupled inverters. These four transistors, M1, M2, M3, and M4, act to reinforce a stable logic state. When the cell is storing a 0, M1 and M4 are both off. For reasons explained at the device level, this makes their drain diffusions sensitive to upset. In practice, the access transistors M5 and M6 are also both off while the cell is holding data but typically are designed as a shared diffusion with the adjacent NMOS device.

A device level diagram of the M1–M2 inverter is shown in Figure 2. The process illustrated is a bulk CMOS process. The explanation of an upset when the logic state of the cell, Q, is low is given for an event at M1. Events at other reverse-biased nodes are also capable of initiating upsets in a similar fashion. In this state the PMOS

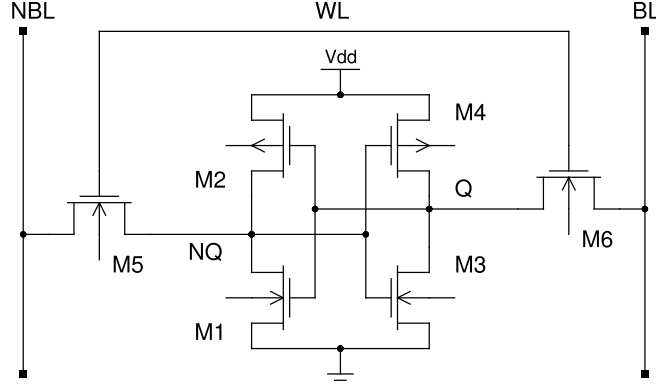


Figure 1: Circuit level schematic diagram of a six transistor SRAM

transistor M2 is on and the NMOS transistor M1 is off. The shared circuit node NQ is maintained high and drives the M3–M4 inverter. Because M1 is off, the full supply voltage is dropped across the drain depletion region setting up an electric field. Carriers generated from an ionizing particle are swept up by the electric field and alter the potential on NQ.

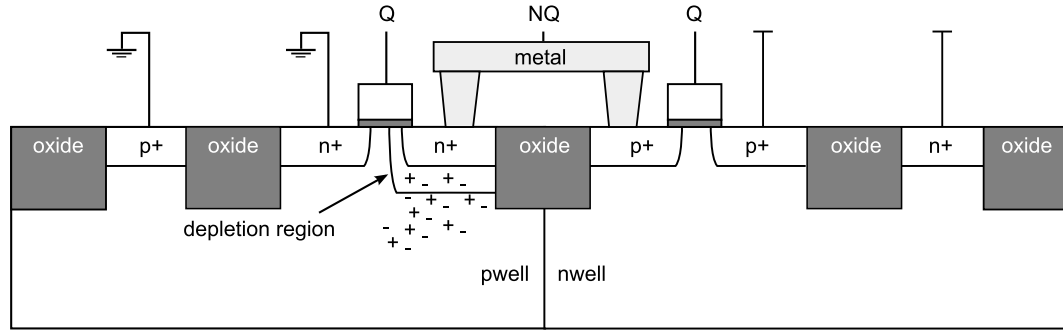


Figure 2: Cross sectional device level view of an inverter fabricated in a bulk CMOS process and illustrating single event photocurrent.

For the purposes of explaining the circuit response, consider that the cell may be represented by an equivalent RC circuit in Figure 3. Here, M2 is represented by a resistor with resistance  $R_{on,M2}$ . Capacitive loads are attached to the NQ contact representing the total gate capacitance of M3 and M4. In addition, resistors are

placed at appropriate locations to represent the resistance to a contact through the well.

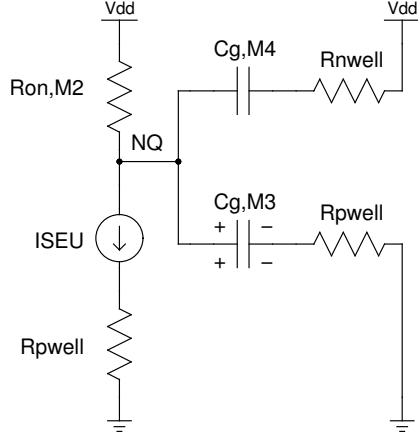


Figure 3: RC equivalent model used to explain a single event transient in the M1–M2 inverter of an SRAM.

To first order, the charge carriers generated by the single event may be represented as an independent current source  $I_{SEU}$  at M1. As current flows through the M1 drain-to-body junction, an equal current must flow into the drain from M2 and the M3 and M4 gates. Initially, charge is stored on the M3 gate capacitor. During the event, the capacitor will discharge and the M4 gate capacitor will charge. The amount of current that the capacitors can supply to NQ (at that instantaneous voltage) dictates the current required to flow through M2. This current creates a potential drop across M2. Therefore the capacitive loads help to maintain the state of the cell.

If the photocurrent at M1 is sufficiently high and maintained for a long enough time, the capacitors will not be able to hold the potential at NQ and it will drop to ground. When this begins to happen, the M3–M4 inverter will switch. The cell then enters a stable, but errant, state with Q high and NQ low.

Once the charge generated by the event recombines or is swept away, the current source will shut off. If the circuit has not yet flipped, either because the amount

of charge was insufficient to do so or the feedback time in the circuit is too long compared to the event, the potentials will be restored and the cell will return to the correct data state.

### Mitigation

A number of techniques are available to mitigate SEUs; from altering the local radiation environment to modifying the circuit design, but each have associated drawbacks. For applications required to use COTS parts, modification of the circuit or creating a custom design is not an option.

In the simplest case, shielding surrounding the device can reduce the energy and flux of incident particles. Although the device sensitivity does not change, the frequency of SEU-inducing particles in the local environment arriving at the active electronics may be reduced and the error rate improved proportionally. It is also possible that the shielding may make the local environment worst by contributing to the low-energy portion of the spectra. This solution has the obvious drawback that heavy shielding may be required to make any significant difference in the local environment seen by the part. Particularly for space missions, adding otherwise unnecessary mass is an undesirable proposition.

Radiation-hardened-by-design techniques can be used to decrease the sensitivity of a cell to ionizing radiation through redundant elements in a circuit or the use of structures designed to minimize charge collection. Similarly, redundancy at the system, architecture, or logical level can be effective at filtering errors in one portion of the design. These techniques necessarily have area and power costs that have prevented them from being used on a wide scale.

For certain portions of an integrated chip, such as an SRAM, error correcting codes (ECC) are often used to detect and correct errors within a data word. These codes are effective against occasional single bit errors but cannot easily be used for sparse sequential elements such as latches and flip-flops. The extra circuitry also introduces delay into read accesses.

Often a combination of well-selected techniques is needed to protect an integrated circuit against errors. Mitigation will reduce, but cannot eliminate the possibility of radiation-induced errors.

### Background Work

In 1962, three years before the now infamous prediction by Gordon Moore regarding the yearly industry growth in the number of components in an integrated function, one of the first doomsday predictions on microelectronics scaling was published by Wallmark and Marcus [7]. This publication made the case that scaling in the fledgling industry would soon cease because of fundamental physical limitations. In addition to photolithographic resolution, excess heat generation, and fluctuations in doping concentration, the authors cited cosmic rays as one of the fundamental phenomena to limit the minimum size of integrated circuits. The analysis considered the hard and soft components of the terrestrial environment, specifically pointing out what were then known as  $\mu$ -mesons. Just like the many predictions that would follow in the footsteps [8], the limits to Moore's law have not yet come to pass and the industry has far exceeded both predictions of minimum feature size and reliability.

The argument was that the flux of cosmic rays passing through an arbitrary cube was so great that a computer with  $10^5$  components each  $10 \mu\text{m}^3$  would suffer a mean

time to failure of one month ( $10^7$  FIT/Mbit). The calculation, performed for only two classes, lightly and highly ionizing particles, assumed that any terrestrial cosmic ray particle passing through a cell was sufficient to cause a soft error. Although in hindsight, the limits were premature, the fundamental arguments are applicable and soft errors from cosmic rays are still a threat to reliability.

A little over ten years later, evidence of single event effects began to appear. The first report to implicate ionizing radiation as the source of anomalous errors came in 1975. In this report, Binder et al. attributed the frequency of failures to the event rate of impinging iron ions on one of 40 JK flip-flops used on-board a communications satellite [9]. In 1978, May and Woods identified alpha emissions from uranium and thorium contaminants in packaging materials as a source for soft errors [10].

Shortly after the initial reports, Ziegler and Lanford published a thorough survey on the terrestrial particle environment and interactions that lead to charge generation in semiconductors [11]. In the analysis, burst-generation curves are used to evaluate the frequency of particle events of a given energy. The analysis of the relative contribution to the error rate for selected parts includes the effects due to electrons, muons, protons, and neutrons through consideration of the ionization wake, recoil, alpha emission, and capture mechanisms. Fig 4 summarizes the analysis presenting the error rate which would be observed if the circuit could be upset by a given level of charge ( $Q_{\text{crit}}$ ). In this plot, devices with thresholds greater than  $8 \times 10^5$  electrons (128 fC) are dominated by muon capture and nuclear reactions, which includes neutron-on-silicon effects. Below this threshold, alpha particles are expected to dominate the error rate. Finally, the authors predicted, although with limited

environmental measurements, that CCDs and future devices with extremely low critical charge values ( $< 16$  fC), would be susceptible to upset from the muon ionization wake. This susceptibility would increase the error rate by orders of magnitude.

The thresholds are not general, but are specific to the device geometry assumed in this analysis. Over the years of technology scaling, devices have been subject to upset from neutron-induced nuclear reactions and alpha particles have grown to become a large concern as well. A sensitivity to muons never materialized in the single event effects literature. This is in part due to the changing dimensions of microelectronics and the dominance of the other mechanisms. The works of [7] and [11] established a warning however, that muons could have a tremendously negative effect on reliability.

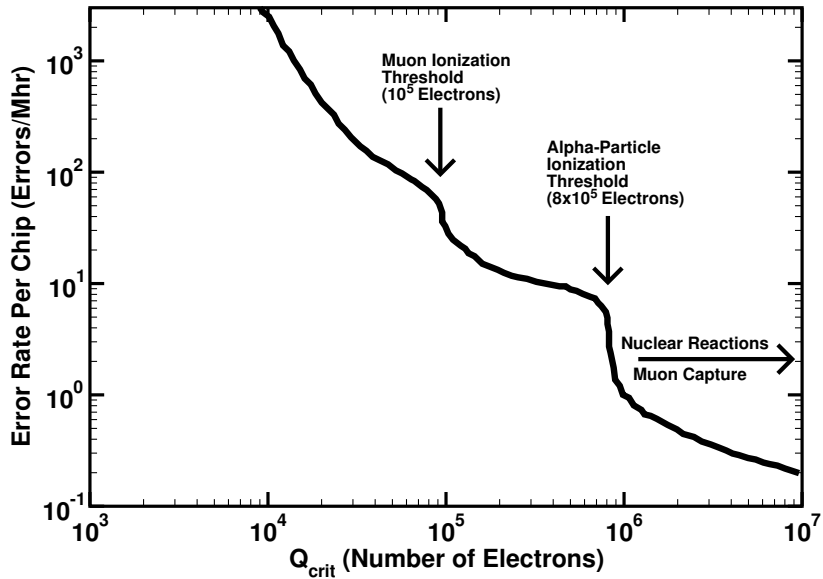


Figure 4: Estimated error rates for devices with critical charge values related to the threshold for different mechanisms of charge generation. Reproduced from [11].

Following the establishment of a rate prediction methodology for the raw sea level environment, Ziegler examined the effect of concrete shielding on the error rate of a few particular devices. Using simple range calculations, he showed that while shielding reduces the overall primary particle flux, increasing levels of concrete shielding does

not guarantee a decreased particle flux over the entire energy range [12]. In particular, the electromagnetic force will shift the energy distribution of charged particles to lower energy because of interactions with electrons in the shielding. The nuclear force will stop some of the hadrons and ions in the shielding, producing secondary particles in the process. This effect will act on neutrons, protons, and ions, but not muons. The final result is that high-energy particles are slowed down and additional particles may be produced. Ignoring secondary particle cascades, the particle fluxes under 10 cm of concrete are shown in Figure 5. Ziegler expected the muon capture and distributed charge burst rate to increase beneath one meter of concrete. The muon component in these calculations was estimated to be 99.8% of the entire particle flux. It was determined that ten meters of concrete were needed to attenuate the muon flux. In a final analysis of the failure rate of a dynamic memory, it was concluded that parts with a high critical charge will see a decrease in error rate due to shielding, but for sensitive parts, the error rate will increase.

Silberberg contended that the rate predictions by [11] failed to consider the heavy nuclear spallation products [13]. Therefore, adopting the burst generation rate computations, he repeated the calculations and produced Figure 6 indicating the terrestrial error rate versus the device critical charge. Of interest is the sea-level contribution from muons, protons, and neutrons. The analysis shows the error rate for devices with critical charge values less than 5 fC are dominated by muons and protons similar to Ziegler and Lanford. It should be noted, however, that the frequency of upsets ( $4 \times 10^8$  FIT/Mbit) is unbelievably high and puts this particular computation in doubt.

Experimental investigations in the early 1980's by Dicello et al. compare muon and pion error counts in accelerated tests and estimate the contribution to the sea level

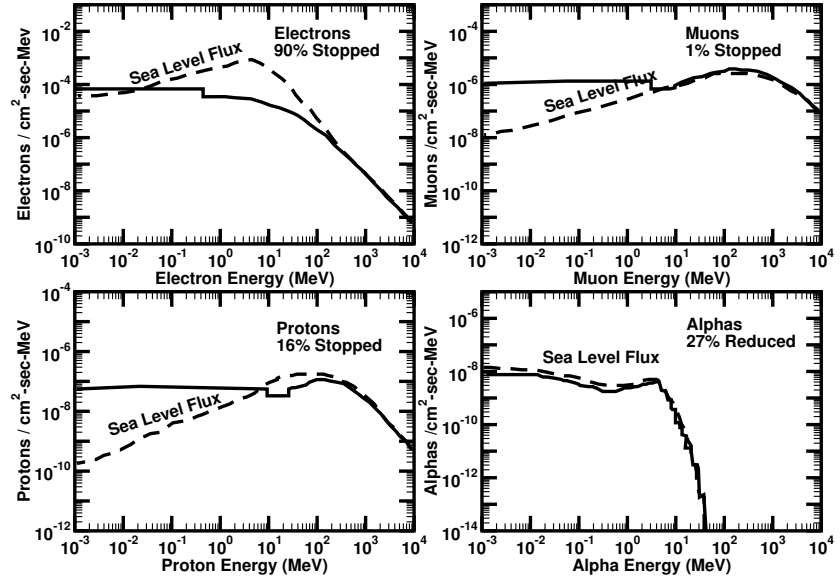


Figure 5: The differential flux of cosmic rays transported through 10 cm of concrete. Dashed lines indicated the original sea level flux for each particle. Solid lines indicate the attenuated flux. Reproduced from [12].

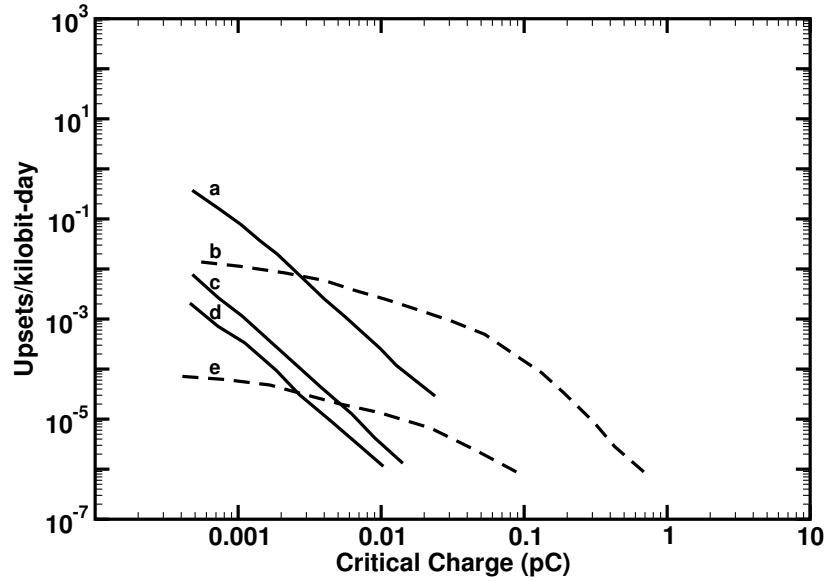


Figure 6: Prediction of device upsets rates at an altitude of 55,000 ft from (a) slow protons, (b) neutrons and sea-level from (c) muons, (d) slow protons, and (e) neutrons. Reproduced from [13].

error rate [14, 15, 16, 17]. The experiments used a cloud muon beam produced by pion decay to obtain error counts. In [14], the authors report on error counts measured with a 4K NMOS SRAM at the now decommissioned Los Alamos Meson Physics Facility (LAMPF). In the experiments, a 164 MeV/c pion beam was able to generate nearly 1000 errors at a fluence of  $2 \times 10^{10} \pi^- / \text{cm}^2$ . Alternatively, a 109 MeV/c muon beam only produced 3 errors at  $4 \times 10^{11} \mu^+ / \text{cm}^2$  and no errors for  $8 \times 10^{10} \mu^- / \text{cm}^2$ . The muon errors were attributed to pion contaminants however. Dicello concluded in this work that pions may be a non-negligible component of the sea level error rate.

In [15] the authors obtained similar data, but using a lucite degrader in the beam-line. The pion-induced error counts decreased with increasing degrader thickness until the device entered the stopping region in which the  $\pi^-$  error counts increased over the  $\pi^+$  by a factor of 7 because of  $\pi^-$  capture.

By placing the device in the stopping region, the authors were able to measure three errors due to  $\mu^-$  over the course of 24 hours in [17]. No errors were observed due to  $\mu^+$  or energetic muons of either charge. Dicello provided an estimate of SEU error rates at sea level and 10 km based on exposure of an NMOS SRAM to pions and muons. From this experiment, the error rate due to stopping muons was estimated at 2% of the total rate due to all terrestrial species. However, the authors also admit that there are large uncertainties in the relative particle fluences.

Further analysis of contributions to the overall error rate are presented in [18] where Srinivasan et al. describe the modeling capability provided by IBM's Soft Error Monte Carlo Model (SEMM). In this work, the models are described and an analysis of the potential for pions to cause single event upsets is provided. The authors show results from their nuclear spallation reaction model NUSPA that the alpha

differential production cross section from pions in silicon is greater than from protons at 250 MeV. They also speculate that the moderately larger production cross section may be significant for terrestrial and especially high-altitude error rates.

In [19] the SEU cross section of DRAM memories exposed to 150 MeV  $\pi^-$  were experimentally measured approximately 4 times greater than for protons of the same energy. Similar results can be found in [20]. Duzellier et al. measured SEU cross sections for  $\pi^+$  at 58, 147 and 237 MeV and protons for both SRAMs (0.5 to 0.8  $\mu\text{m}$  processes) and DRAMs (0.35 to 0.5  $\mu\text{m}$  processes) in [21] and found that protons were slightly more capable of causing SEU than pions. These results in both cases suggest that pions upset devices in a similar fashion as p–Si interactions.

Tang expounded on the NUSPA software system in [22]. He concluded that the effect from pions would be a small correction to sea level error rate predictions because the flux is lower than the flux of neutrons, but that it should be included in any analysis at higher altitudes. He also asserted that muons are not a concern for single event effects. The reasoning behind this argument is that slow positive muons ( $< 1 \text{ MeV}$ ) will capture an electron forming muonium and result in a pair of gammas through a decay and annihilation. These processes will be discussed in Chapter II. Fast muons are too lightly ionizing and unable to cause SEE.

Normand demonstrated in [23] that the dominant component of the terrestrial cosmic ray environment causing SEU was high-energy neutrons. The correlation of measured chip failure rates with measurements made at the Los Alamos Weapons Neutron Research Facility essentially put to rest the debate over the dominant source of errors.

Ziegler and Puchner write that pion capture is well-known through geological

analysis and occurs at a rate of  $8.5/\text{cm}^3\text{-year}$  [24]. The subsequent fission event may release up to 22 nC. For a given chip volume of  $3 \times 10^{-5} \text{ cm}^3$ , and the large quantity of charge generated, pion capture contributes roughly 30 FIT even behind a couple of feet of concrete. Pions also interact through the strong force and the authors point out that in Leadville, CO, the proton and pion flux are sufficiently high that they must be considered in addition to neutrons.

Muons do not interact through the strong force so they can penetrate much farther through shielding. Muon capture rarely cause charge generation. In these rare cases the event could be a silicon recoil or emission of an alpha in total contributing to 70 FIT.

Duzellier et al. further studied the energy threshold for proton-induced SEU in [25]. The study examined a number of memories and showed the SEU cross section versus proton energy for each. The data set shows that while most parts have an energy threshold between 10 and 20 MeV, some were lower. The authors concluded that effects from electronic stopping were not evident, but could be if thresholds continued to decrease below 2 MeV.

### Trend in Single Event Sensitivity

Measured critical charge thresholds have been shown to decrease steadily with technology scaling. In [26, 27], Petersen et al. presented a collection of critical charge ( $Q_{\text{crit}}$ ) values for memories fabricated in various processes and feature sizes. As one would expect, the thresholds for upset is smaller according to feature size. Applying a least squares curve fit using a power law, the data can be used to extrapolate onset charge to smaller feature sizes. The data imply that moving to the next technology

node reduce the onset charge by nearly 50%. The implication for scaled devices is that they will naturally become more sensitive to the ionizing radiation in the surrounding environment.

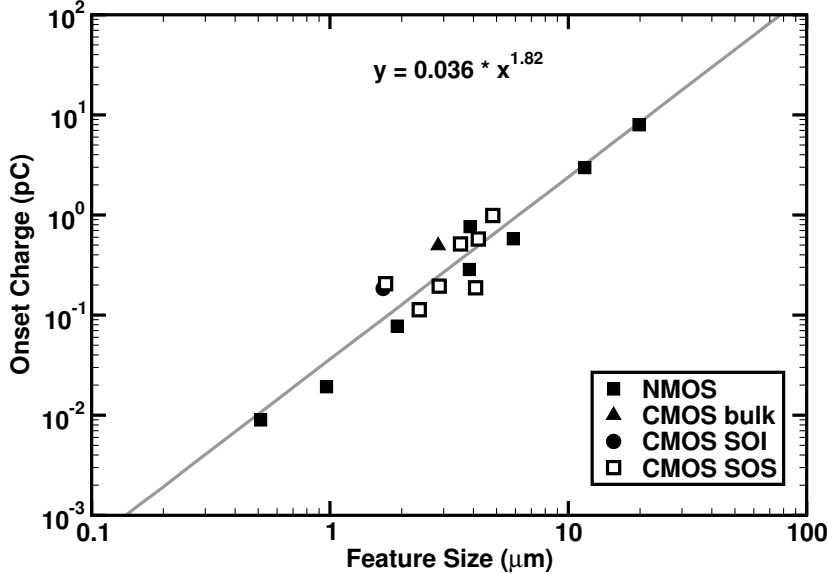


Figure 7: Critical charge trend with technology scaling. Reproduced from [27]. Power law fit shown in grey.

This trend in the upset threshold can also be justified by the previous section on SEU mechanisms and the basic device scaling suggested in [28]. Under the assumptions of constant field scaling moving from one technology node to another, the area of a transistor gate  $A$  scales by  $\kappa^{-2}$ , and the gate dielectric thickness  $t_{\text{ox}}$  and the operating voltage  $V$  by  $\kappa^{-1}$  for a scaling factor  $\kappa$ . Scaling between technology nodes is typically done according to  $\kappa = \sqrt{2}$ . Therefore, the charge stored on a transistor gate,  $Q = \epsilon A V / t_{\text{ox}}$ , will scale by  $\kappa^{-2}$ . If instead constant voltage scaling is assumed, only the gate area  $A$  scales maintaining the  $\kappa^{-2}$  scaling on  $Q$ . In practice, neither choice of scaling is strictly adhered to in order to maintain performance and avoid dielectric breakdown, but the theory offers useful insight into the effects of scaling on the critical charge for SEU and agrees well with the values reported by Petersen.

For terrestrial applications, the field error rates have only partially reflected this trend in sensitivity. Baumann presented data in [29] that show a steady increase in the soft error rate of memories according to smaller dimensions from  $0.5$  to  $0.25 \mu\text{m}$  technologies. The increase in frequency of errors is attributed to the reductions in operating voltage and node capacitance. After the elimination of borophosphosilicate glass in these memories following the  $0.25 \mu\text{m}$  nodes, the error rates have saturated. This latter constant trend is attributed to the lack of operating voltage scaling.

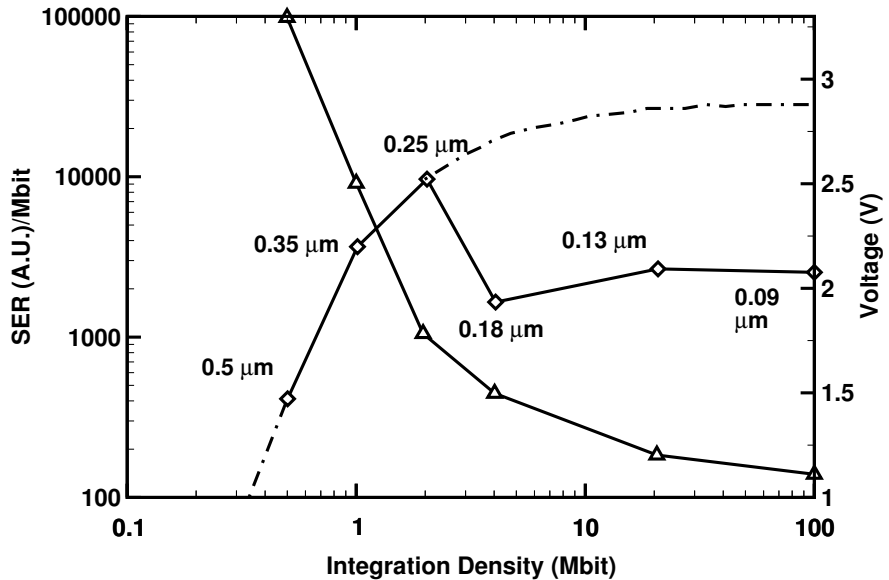


Figure 8: The trend in SRAM single bit SER as a function of technology node (open diamonds). Operating voltage as a function of technology node show in open triangles. Reproduced from [29].

### The Onset of Proton Direct Ionization Upsets

In an effort to explore test methods to measure the low-LET region of SEU cross section curves without resorting to high-energy ion facilities, Gerardin et al. measured the effects of a 2 MeV proton beam on SRAMs in [30]. Although the accumulated dose affected the measured cross sections, the data in this work suggest the onset of

proton direct ionization induced SEU in these technologies.

Heidel et al. later presented a model for determining the critical charge for latches and memory in [31]. By varying the angle of incidence of a monochromatic alpha beam, the sensitivity of various circuit designs fabricated in an IBM 65 nm SOI technology were determined and used to calculate the charge required for upset through geometric arguments. Estimates of the critical charge ranged from 0.5 to 1.0 fC.

The method presented by Heidel and the aforementioned report [30] prompted a test of the same IBM parts with a low-energy proton beam by Rodbell et al. [32]. These data, shown in Figure 9, demonstrate the increase in SRAM fails as the part is rotated in a proton beam. The errors at angle are the result of charge generated from the proton's extended path length through the device which exceed the critical charge. These data are now regarded as the first conclusive evidence of proton direct ionization induced SEU. The impact for on-orbit applications was later estimated in [33] by studying the ratio of the low-energy and high-energy proton environment and respective SEU cross sections.

Kobayashi et al. extended the impact of proton direct ionization from space to the terrestrial environment [34]. PHITS simulations indicate that terrestrial error rates will increase with technology scaling because low energy protons are secondaries from n–Si reactions. Although the general error rate trend with scaling decreases in this analysis, the proton sensitivity is predicted to cause the rate in sub 45 nm SRAMs to increase.

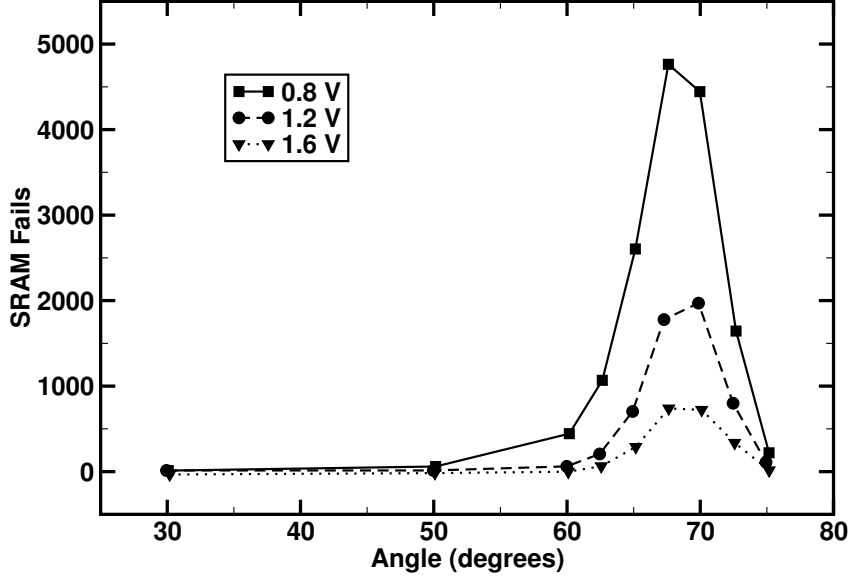


Figure 9: Single event upset counts for low-energy protons over angle of incidence for an IBM SOI 65 nm SRAM. Reproduced from [32].

### Conclusions

Reliability is an important issue for the designers of critical systems. The cost of radiation hardened parts both in monetary terms and the penalties of area, power, and weight discourage their use and make COTS parts appealing. However, the development of semiconductor processes is typically not performed with reliability as a first priority. In fact, the current industry drivers of power and performance are somewhat orthogonal to reliability.

Decades of development have brought semiconductor devices to the point where they have been shown to be sensitive to the direct ionization from a single charge – a proton. For both the space and terrestrial radiation effects communities, the consequences of this vulnerability are yet to be fully understood.

## CHAPTER II

### PHYSICAL PROCESSES

Radiation can generate charge in semiconductor devices through a variety of mechanisms. Energetic particles lose energy through interactions with matter and the nature of the interaction determines both the amount and spatial distribution of the energy. The particles considered in this section and their physical properties are presented in Table 1. The table does not represent an exhaustive list of singly-charged particles in the Standard Model, but only those with a mean lifetime greater than 1 ns. It is reasonable to believe that shorter lived particles will have virtually no impact on devices.

The interactions of these particles may be through electronic and nuclear stopping, elastic and inelastic nuclear scattering, Coulomb scattering, spallation, or capture. Further, unstable particles undergo decay. These processes are discussed in this section with an emphasis on energy deposition relevant for single particle induced transient behaviors. Each of these processes must be understood to accurately assess the radiation response of microelectronics in arbitrary radiation environments. The effects of accumulated dose and damage events are addressed elsewhere in literature and will not be recounted here.

The stopping power of a medium is the mean rate of energy loss ( $-dE/dx$ ) by an energetic particle through the material. The stopping power can be subdivided into electronic and nuclear components as the loss of kinetic energy is due to the Coulombic interactions with electrons and nuclei. For energetic particles the electronic stopping

power is substantially greater than the nuclear stopping power. These rates of energy loss are commonly normalized to the density of the medium and expressed in units of MeV-cm<sup>2</sup>/mg. The interactions are described in more detail here.

Table 1: Physical properties for singly-charged particles

Symbol	Particle	Mass (MeV/c <sup>2</sup> )	Mean Lifetime
$e$	electron / positron	0.510 998 910(13)	–
$\mu$	muon	105.658 367(4)	2.2 $\mu$ s
$\pi$	pion	139.570 18(35)	26 ns
$K$	kaon	493.667	12 ns
$p$	proton	938.272 013(23)	–

### Electronic Interactions

#### Electronic Stopping

The electronic stopping power arises from a particle's energy loss due to inelastic collisions with electrons in the target medium through the electromagnetic force. A portion of the energy loss will result in valence electrons being raised to an excited state in the conduction band. These electrons (and holes) contribute to the ion-induced photocurrent. High energy transfers to electrons provide kinetic energy to the electrons, resulting in delta rays that may distribute the energy away from the ion track and create additional electron-hole pairs. The maximum amount of energy transferred to an electron is denoted by  $T_{\max}$ .

The mean rate of energy loss, is described by the Bethe-Bloch equation. The form in Equation 2 is the first order Born approximation [35]. The formula contains terms for the electron charge  $e$ , mass of an electron  $m_e$ , speed of light  $c$ , the relative particle velocity  $\beta$ , and the particle charge unit  $z$ .  $K$ ,  $Z$ ,  $A$ , and  $I$  are properties

of the target medium. Details of the origins and higher-level corrections can also be found in [36, 37]. When including the corrections it is believed to accurately describe the stopping power for protons down to 1 MeV.

$$-\frac{dE}{dx} = Kz^2 \frac{Z}{A} \frac{1}{\beta^2} \left[ \frac{1}{2} \ln \frac{2m_e c^2 \beta^2 \gamma^2 T_{\max}}{I^2} - \beta^2 - \frac{\delta(\beta\gamma)}{2} \right] \quad (2)$$

From Equation 2 it can be observed that the energy loss in a given material depends heavily on the charge of the incident particle. Therefore all singly-charged particles will have approximately the same rate of energy loss at the same velocity  $\beta$ . For single event effects, these curves are typically parameterized over kinetic energy.

As the particle slows in the Bethe-Bloch region, the mass stopping power increases as shown in Figure 10. This continues until the stopping power reaches a maximum at low energy known as the Bragg peak. For protons, the Bragg Peak occurs at approximately 50 keV, depositing a little over 0.5 MeV-cm<sup>2</sup>/mg. Charged pions and muons reach the Bragg Peak at approximately 8 keV. Experimental data [38, 39, 40] have confirmed and refined these stopping power curves.

The mass stopping power curves for  $\mu^-$ ,  $\pi^-$ , and  $e^-$  are not shown in Figure 10. The curves follow the general shape of their antiparticle, but have slightly lower values of stopping power as described by the Barkas effect [35].

The ionizing energy lost to the target medium produces electron-hole pairs in semiconductors. For silicon this ionization energy has been empirically measured at 3.6 eV. From this value a convenient conversion for silicon is 22.5 MeV of ionizing energy deposition yields 1 pC of charge.

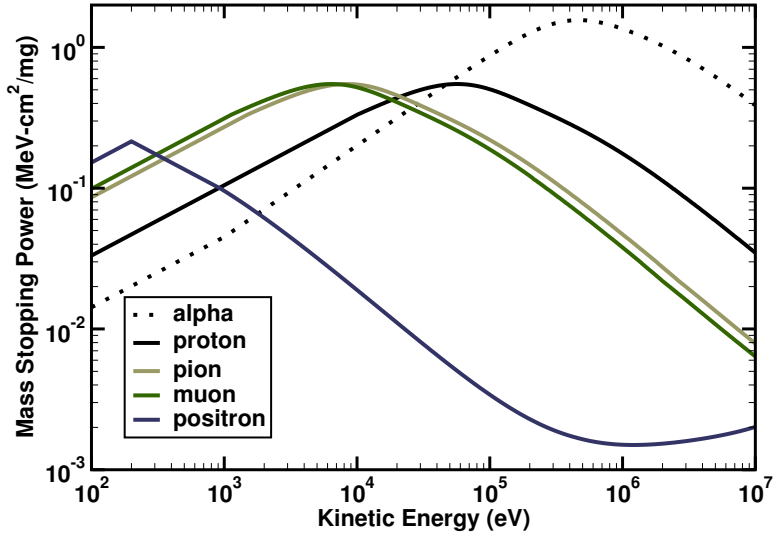


Figure 10: Mass stopping power extracted from Geant4 for protons, pions, muons, and positrons in silicon. Alpha particle stopping power shown for reference.

### Electron Stripping

As an element travels through a medium it is stripped of its electrons leaving an ionized particle. For the purposes of the Bethe-Bloch equation, the stopping power depends on the ionized state of the particle. This is sometimes referred to as the  $z_{\text{eff}}$ , a charge referring to the expected value of the particle's charge state. If a proton, muon, pion, or other elementary particle is accompanied by an electron, the element is charge neutral and therefore will not ionize the medium as it passes through. For single event effects from high-energy ions this process is irrelevant, however, it is addressed here as the following sections describe low-energy effects.

For heavy ions passing through a medium, the Thomas-Fermi velocity defines a rough border on which the majority of electrons are stripped from the nucleus [37]. However, according to Ziegler this threshold poorly predicts electron stripping for light ions. He asserts that stopping powers for low-energy protons have been experimentally measured below the Thomas-Fermi velocity and also alludes to arguments over

whether energetic protons could ever capture an electron due to the size of the electron's orbital diameter. If some of the protons are not stripped at these low-energies, then the refinements to the theory based on measurements of stopping power already reflect this. He argues that the Bethe-Bloch equation is being used outside of its validity in this regime anyhow. Therefore the stopping power of a single particle may be slightly larger than these models predict but it is unlikely that a large percentage have captured an electron.

A similar occurrence happens for muons. When an electron orbits a slow  $\mu^+$  particle, it creates a short-lived element similar to hydrogen known as muonium.

### Range

One metric for the range of a particle in a medium is the continuous slowing down approximation (CSDA). This approximation assumes that particles of a given energy will slow down in a straight path according to the stopping power calculation. The particle's ultimate range is dictated by an integration of the stopping power. Deflections and straggling are not accounted for in this model. This value is only appropriate where the range is much less than the nuclear interaction length. It is useful, however, for approximating the penetration depth of a beam and therefore has direct relevance to SEE and accelerated test planning. Figure 11 presents the CSDA range for a selection of particles of a given kinetic energy. Because the stopping power is lower for pions and muons than for protons, the range of the particles is slightly greater.

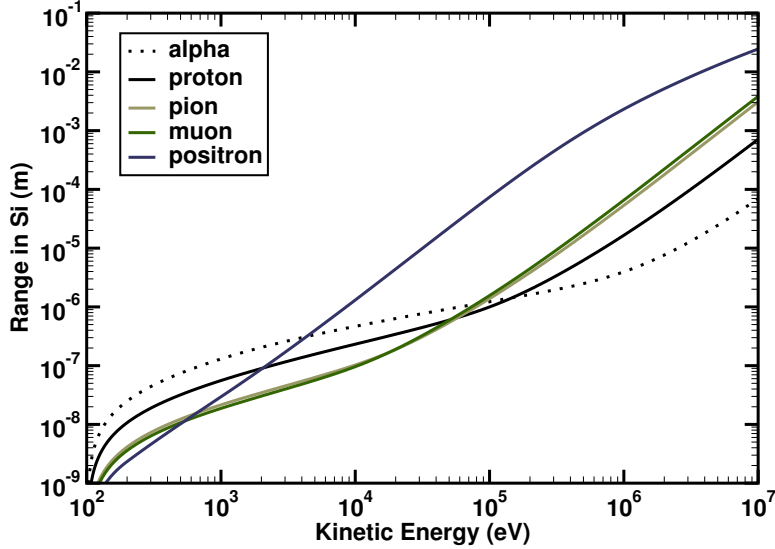


Figure 11: Range in silicon extracted from Geant4 for protons, pions, muons, and positrons. Alpha particle range shown for reference.

### Nuclear Interactions

In addition to electronic interactions, particles also interact with nuclei during their passage through the target medium. These relatively rare reactions can introduce substantial amounts of energy into a small volume compared with electronic stopping. Although the nuclear interactions can occur through a variety of channels, an approximate probability [41] for a neutron or proton of energy  $E$  to interact in a volume can be computed by the following equation

$$P(E) = 1 - e^{-n\sigma(E)t} \quad (3)$$

Here,  $n$  is the atomic density ( $5 \times 10^{22}$  atoms/cm<sup>3</sup> in silicon),  $\sigma(E)$  is the total cross section, and  $t$  is the thickness of the volume. This method can provide an order of magnitude estimation, but more accurate models are a complex interplay of mechanisms, secondary particle range, and track structure.

## Coulomb Scattering

Coulomb scattering occurs when an incident particle interacts with a nucleus in the target material through the electromagnetic force. Because kinetic energy is conserved, this mechanism is considered an elastic scatter. When the particle interacts with a nucleus in this manner, it may impart enough energy to break the atom free from a semiconductor crystal lattice. In this case, the recoiling nucleus can deposit energy as well.

## Nuclear Elastic Scattering

The elastic scattering process occurs when an incident particle interacts through the strong force with a nucleus in the target material, imparting some of the initial energy to the nucleus, and conserving total kinetic energy. The kinetic energy imparted to the recoiling nucleus can be computed according to Equation 4 given the initial particle kinetic energy  $E_p$  and mass  $m$  and the scattering angle  $\theta$  (in the center of mass frame) of the recoil with mass  $M$ .

$$E_{\text{recoil}} = \frac{4mM}{(m + M)^2} E_p \cos^2 \theta \quad (4)$$

In particular for neutrons, this process can occur for any incident kinetic energy. According to this equation, a 10 MeV neutron, which is a relevant threshold for electronics reliability, is capable of producing a 1.3 MeV silicon or 2.2 MeV oxygen recoiling nucleus.

The Coulomb barrier to overcome the electromagnetic force experienced by a charged particle is given by Equation 5 [42] and summarized for common elements in Table 2.

$$U_{\text{coul}} = 1.03 \times \frac{A_1 + A_2}{A_2} \times \frac{Z_1 Z_2}{A_1^{1/3} + A_2^{1/3}} \quad (5)$$

Table 2: Coulomb Barrier Potentials for Common Semiconductor Materials

Target Nucleus	Proton Energy (MeV)
<sup>16</sup> O	2.5
<sup>28</sup> Si	3.7
<sup>63</sup> Cu	6.1
<sup>184</sup> W	11.5

### Nuclear Inelastic Scattering

The inelastic scattering process occurs when an incident particle is absorbed by a nucleus of the target material and re-emitted with a lower kinetic energy. The process leaves the recoiling nucleus in an excited state and therefore total kinetic energy is not conserved. The nucleus will de-excite by emitting a gamma ray. The maximum energy of the recoil is therefore still governed by Equation 4.

### Spallation

Spallation is an inelastic event that occurs when a high-energy particle causes a nucleus to fragment or “spall” into several parts. These reactions typically produce several smaller fragments and often nucleons. Unlike elastic scattering where the heavy recoiling nucleus deposits the lost energy, the small fragments can deposit energy over a long range.

### Pion Production

Pions are produced as the result of a high-energy proton-proton collision. The energy threshold for this process is approximated by computing the incoming energy

of two protons in the center of mass frame, such that both stop during the collision and 135 MeV of kinetic energy is transformed into a  $\pi^0$ . The pion production threshold is 290 MeV in the lab frame.

### Capture

Negative pions and muons can become captured by a nucleus once they have sufficiently slowed down [43]. In this process the  $\pi^-$  or  $\mu^-$  begins to orbit the nucleus due to the Coulomb potential. Because these particles are over 200× as massive as an electron and have spiraled down to the 1s shell, they can interact and become captured by one of the nucleons. The process results in a large energy deposition event often referred to as star formation.

### Decay

#### Pion Decay

Charged pions are unstable and decay with a mean lifetime of 26 ns. Neutral pions have a much shorter lifetime ( $8.4 \times 10^{-17}$  s), only produce gammas, electrons, and positrons, and are therefore not considered in the following sections. Charged pions have two decay modes of which the most frequent modes (6) and (8) result in a muon and a neutrino. Conservation of energy and momentum dictate that the muon departs with a kinetic energy of 4.1 MeV. These decays are responsible for the terrestrial muonic component as will be discussed in Chapter III. In the less probable decay modes (7) and (9), the pion results in an electron and neutrino.

$$\pi^+ \rightarrow \mu^+ + \nu_\mu \quad (6)$$

$$\pi^+ \rightarrow e^+ + \nu_e \quad (7)$$

$$\pi^- \rightarrow \mu^- + \bar{\nu}_\mu \quad (8)$$

$$\pi^- \rightarrow e^- + \bar{\nu}_e \quad (9)$$

### Muon Decay

Muons are also unstable particles and decay with a mean lifetime is  $2.2 \mu s$ . The two decay modes transform muons into electrons or positrons and neutrinos according to (10) and (11). The daughters of this decay have very little consequence for microelectronics.

$$\mu^- \rightarrow e^- + \bar{\nu}_e + \nu_\mu \quad (10)$$

$$\mu^+ \rightarrow e^+ + \nu_e + \bar{\nu}_\mu \quad (11)$$

### Conclusions

The energy deposition from ionizing radiation is often modeled through chordlength models for heavy ion direct ionization and crude phenomenological models to fit neutron and proton-induced nuclear reactions. For many older technologies, these simple approximations have sufficed to evaluate a part. In some applications, these approximations have failed to capture an adequate set of physics to provide accuracy. Monte Carlo techniques to single event effects modeling which incorporate fidelity through physical process of radiation transport and energy loss have shown promise to address

the shortcomings of the existing approximations. Further, an understanding of the physical processes is important to develop test methods for singly-charged particles and understand the results.

## CHAPTER III

### RADIATION ENVIRONMENTS

Classically, error rate predictions for devices outside the Earth’s magnetosphere have focused on heavy ions, predictions at low Earth orbits focused on protons, and predictions of terrestrial soft errors have considered neutrons. It is worth noting that alpha emissions from impurities in the chip and packaging also contribute to the overall error rate of a part. This contribution may vary wildly depending on the purity of the processed materials. In this chapter we discuss a number of relevant natural environments in the context of single event effects.

In the following sections which address measurements of the particle environment, we will use the following definitions in accordance to [44]. The directional intensity  $I$  of a particle species in a given environment is presented as  $I d\Omega d\sigma dt$  for incident particles over a time  $dt$  upon an area  $d\sigma$ , from a solid angle  $d\Omega$ . The units are thus  $\text{cm}^{-2}\text{s}^{-1}\text{sr}^{-1}$ . Unless otherwise specified, these values are typically the vertical intensity of the environment. Intensity measurements are a common result of telescopic experiments and therefore a complete description, require information on the angular distribution of the environment.

The flux  $J_1 d\sigma dt$  measures the number of particles incident over a time  $dt$  upon an area  $d\sigma$  which originate from the upper hemisphere. The units of flux are given in  $\text{cm}^{-2}\text{s}^{-1}$ . It can be derived from the intensity integrated over  $d\Omega$  according to Equation 12 where  $\theta$  is the extent of the solid angle from the vertical direction.

$$J_1 = \int I \cos \theta d\Omega \quad (12)$$

## Extraterrestrial Environments

### Interplanetary Space

In the region of interstellar space outside of our sun's heliopause particles of unknown origins continuously stream into our solar system from all directions. These galactic cosmic rays (GCR) consist of ionized particles that are stripped of electrons by the stellar medium. The largest portion of the composition is hydrogen, although most atomic elements are present. The particles have been accelerated and traveled through the galactic magnetic field for possibly millions of years. Probes in interplanetary space and satellites in a geo-synchronous orbit (GEO, approx. 35,786 km altitude) will be primarily subject to the GCR spectra. The basic form of the differential energy spectra follows a power law of the form  $j_1(E) \propto E^{-\gamma}$  where  $\gamma$  is approximately 2.7 for energies between 1 GeV and  $10^6$  GeV [45]. The low-energy portion of the spectra is modulated in local interplanetary space by the solar wind. The cosmic ray flux is reduced during solar maximum as the solar wind resists the interstellar particles from entering the heliopause. This wind consists of particles emitted from the sun and therefore depends on solar activity. Both the GCRs which penetrate the heliosphere and solar energetic particles make up the interplanetary environment.

One popular model of the environment was proposed by Nymmik and has become an ISO standard [46]. The algorithm simplifies the complex interactions of cosmic ray propagation by relating the flux spectra with the Wolf (sunspot) number. In this way, the model tends to be predictive. Other codes such as the Badhwar–O'Neill model [47], that base the flux spectra off of correlated values from neutron monitors

are better suited for elucidative modeling. The Cosmic Ray Effects on Microelectronics (CREME96) codes [48] implement the GCR algorithm as specified in [49]. An updated version of the CREME96 GCR model conforms to the ISO draft most notably omitting the upturn in differential flux below 10 MeV/u seen in the previous model. Figures 12 and 13 show these spectra as computed by the original CREME96 codes. Hydrogen, the most abundant element in the universe, has the highest flux in these environments. Helium and other light ions are typically one or more orders of magnitude lower in flux.

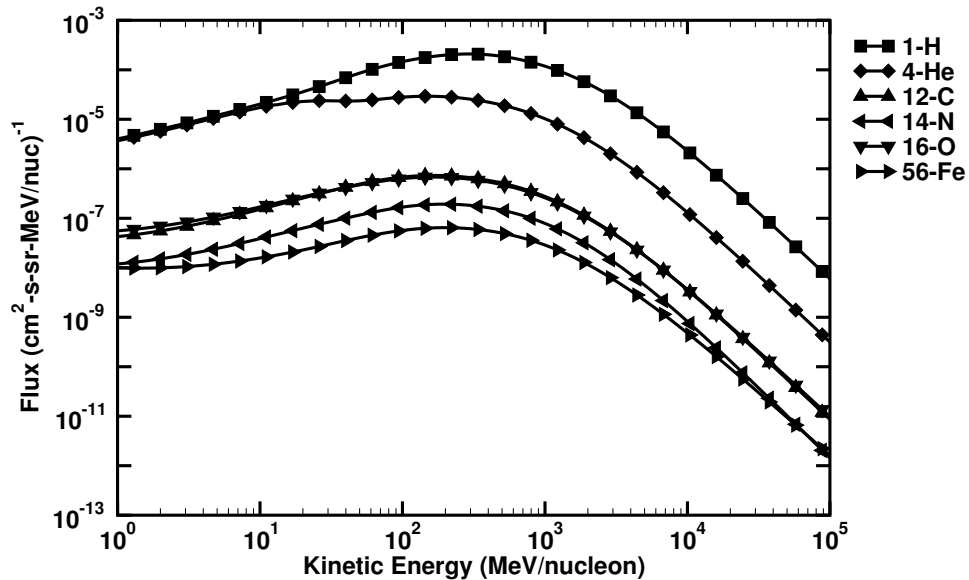


Figure 12: The particle flux spectra computed by CREME96 for a Near-Earth Interplanetary or Geosynchronous orbit during solar minimum with 100 mils of aluminum shielding. Common species shown, all others omitted.

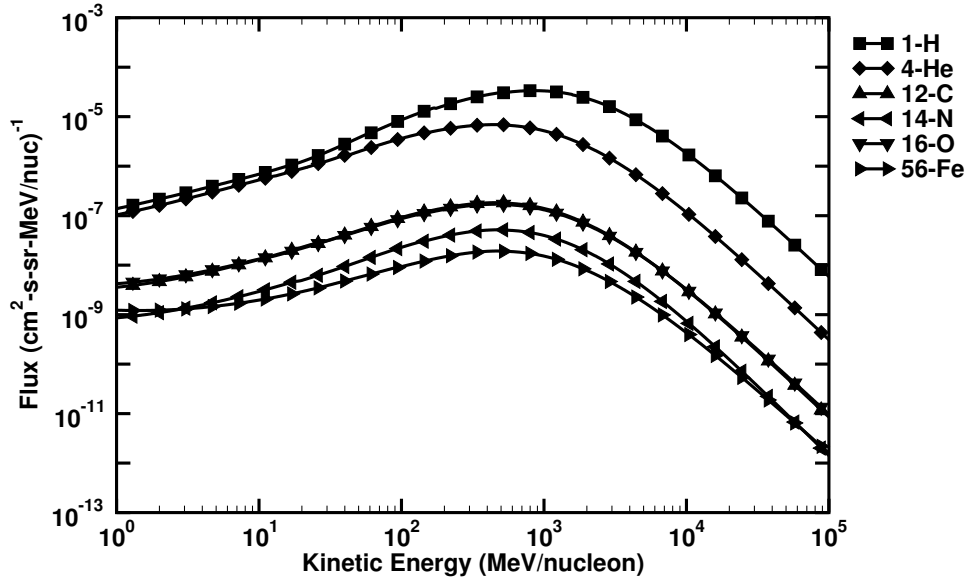


Figure 13: The particle flux spectra computed by CREME96 for a Near-Earth Interplanetary or Geosynchronous orbit during solar maximum with 100 mils of aluminum shielding. Common species shown, all others omitted.

### Near Earth

#### Solar Particle Events

Solar particle events are the result of coronal mass ejections from the sun's surface. In these events a large flux of (mostly low energy) particles are emitted into the interplanetary medium. They follow the magnetic field lines and depending on the position of the Earth, may arrive at the near-Earth environment. The events occur randomly in time and vary in severity.

Several models exist for these environments. The models in CREME96 are derived from data acquired during the October 1989 event. The enhanced flux in the “Worst day” model can be seen in Figure 14. While these events have an effect throughout the solar system, the models should only be considered for use in near Earth environments.

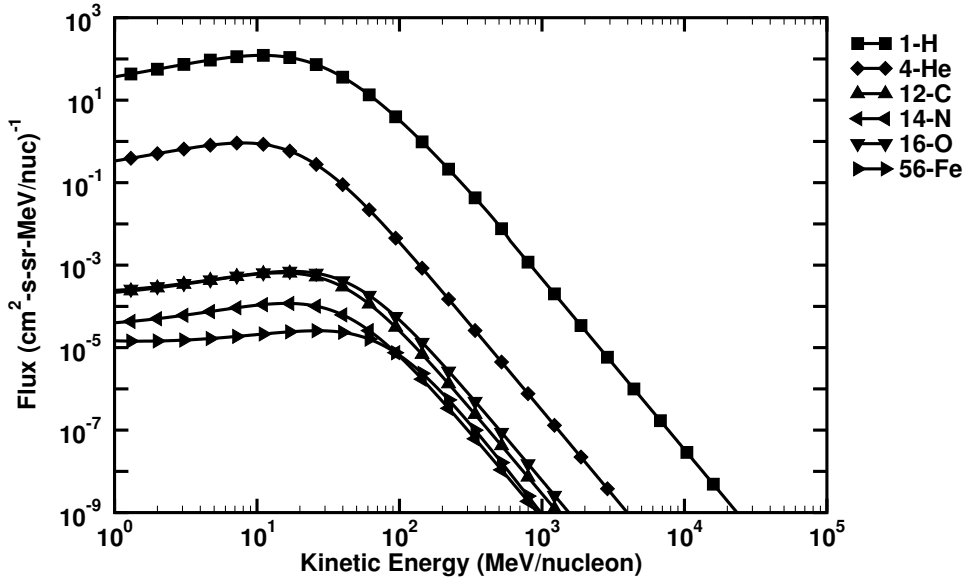


Figure 14: The particle flux spectra computed by CREME96 for a Near-Earth Interplanetary or Geosynchronous orbit during the worst day scenario with 100 mils of aluminum shielding. Common species shown, all others omitted.

### Magnetic Rigidity

The Earth's magnetosphere prevents low-energy charged particles from entering the atmosphere. For low-inclination, low-Earth orbits (LEO) this is an important consideration. At inclinations above  $45^\circ$ , such as polar orbits, the geomagnetic shielding is less effective.

### Trapped Proton and Electron Belts

The Earth's magnetic field not only prevents radiation from entering the atmosphere, but also traps (relatively) low-energy particles. Van Allen is credited with the discovery of the radiation belts. Although previously predicted, he first reported the results of an investigation into the trapped population of particle surrounding the Earth [50]. Using detectors on-board a satellite in 1958 with an inclination of 51 deg, 260 km perigee and 2200 km apogee, the experiment reported the counting rates as

a function of the satellite position. Additional investigations into the trapped populations have been carried out and have resulted in the development of environment models with versions AP-8 and AE-8 released in 1976 [51]. Development of AP-9 and AE-9 releases is underway to improve the accuracy of the models and address sources of uncertainty. An excellent source of the history is recounted in [52].

In fact, the belts consist of two zones with a slot region between. The inner zone consists of both protons and electrons and extends to approximately  $2R_E$  (Earth radii). Figure 15 shows one description of the flux of protons from the AP-8 model. The higher energy protons of 400 MeV or more are mostly confined in the inner zone below  $2R_E$  with the spectrum becoming softer at higher altitudes. This zone is more stable for protons greater than 25 MeV, however, atmospheric effects at altitudes below 1000 km [53] can cause variation in the flux. Additionally, at altitudes less than 600 km the atmosphere causes a rapid drop in the flux, providing a large source of uncertainty for models. Figure 16 provides the CREME96 particle flux spectra for the International Space Station orbit.

The discrepancy between the tilt and location of the geographic and magnetic poles produces a region known as the South Atlantic Anomaly. In this region, the inner zone is closest to the surface of the Earth. Low-Earth orbit satellites passing through this region will experience temporarily high levels of radiation. Some high-voltage instruments have to be powered off during this period of their orbit.

The outer zone is located beyond  $3R_E$  and contains mostly electrons. Compared to the inner zone, the outer zone is not as stable as it is affected by solar variations. The flux of particles in the region even exhibits a diurnal variation at a fixed altitude due to solar winds compressing the magnetic field on the sun-side of the Earth.

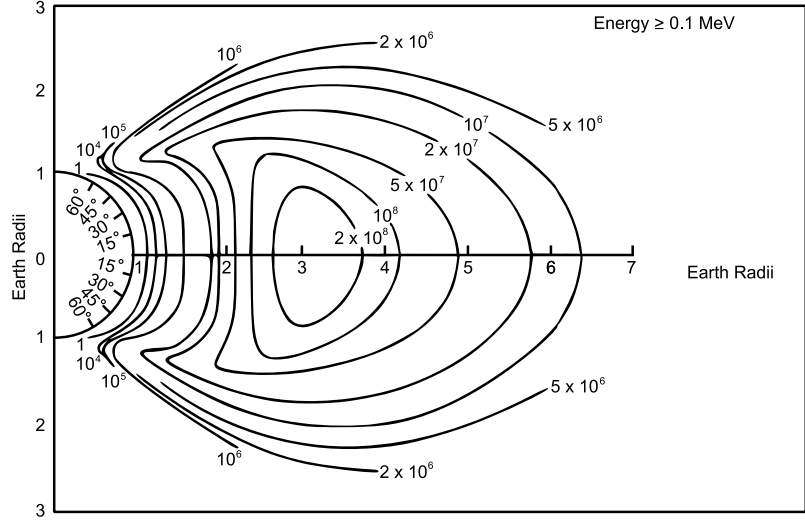


Figure 15: AP8MIN constant intensity omnidirectional flux (protons/cm<sup>2</sup>-s) with energy  $\geq 0.1$  MeV. Reproduced from [51].

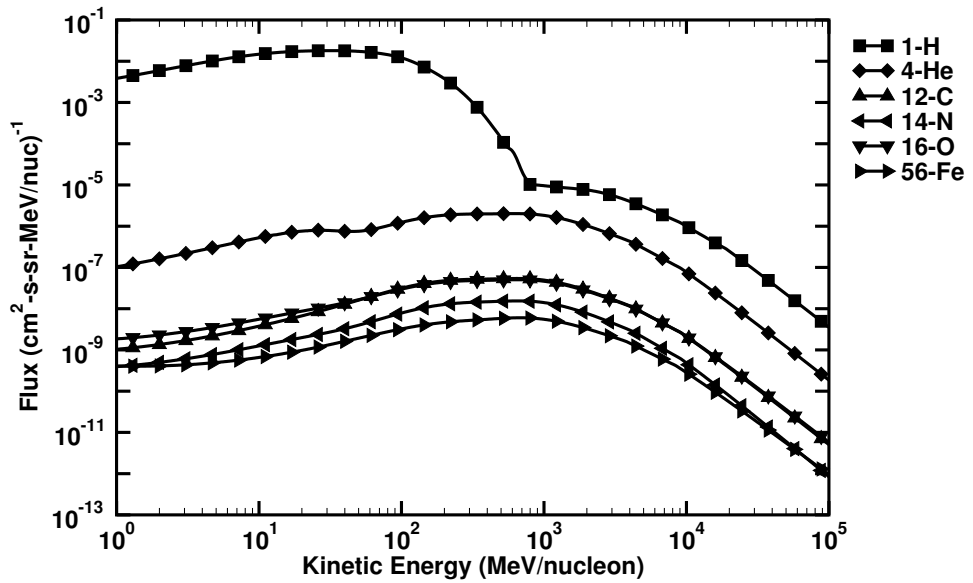


Figure 16: The particle flux spectra computed by CREME96 for the ISS orbit during solar minimum and quiet geomagnetic conditions transported through 100 mils of aluminum shielding. Common species shown, all others omitted.

The slot region between the inner and outer zones is highly dependent on the effects of solar activity on the magnetosphere, and can even become depleted. Data have also shown that another proton belt may form just outside of the inner belt during some solar storms and last for several months afterwards [54].

### Terrestrial Environments

As high-energy GCR particles reach the Earth, they strike the atmosphere resulting in nuclear reactions. At high altitudes the environment consists mainly of protons. Several measurements of the high altitude environment have been made [55, 56, 57, 58]. The nuclear reactions produce showers of particles in secondary and tertiary reactions as illustrated in Figure 17. These interactions generate the “soft” electronic, “hard” mesonic, and nucleonic components. Because of the generation of secondary particles and the variation in atmospheric density, the intensity of particles changes greatly with altitude. One notable region varying around 20 km in altitude is termed the Pfitzner point [59] at which the intensity reaches a maximum.

In addition to altitude, the intensities of the atmospheric particles have distributions over zenith angle  $\theta$ . It is widely accepted that this distribution can be modeled using the vertical intensity  $I_0$  and a fitting parameter  $n$  according to Equation 13.

$$I = I_0 \cos(\theta)^n \quad (13)$$

To complicate matters, the parameter  $n$  itself is a function of the particle energy. Other variations in intensity exist as a result of an east-west effect, geomagnetic rigidity, solar cycle, and diurnal variation.

To address the complications of the environments and the shortcomings of the

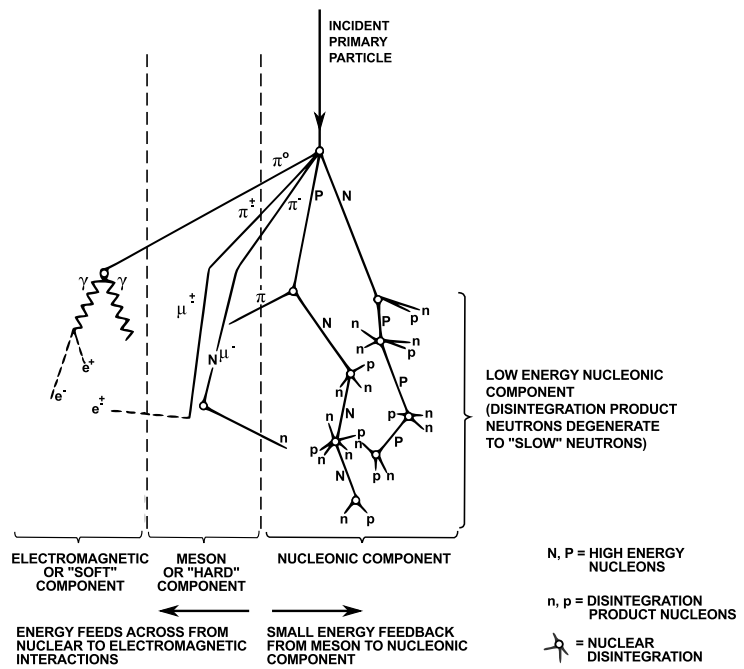


Figure 17: Illustration of cosmic ray interactions in the atmosphere generating showers of daughter particles

existing datasets, several terrestrial environment models have been proposed. Most of these are based on Monte Carlo simulations of the interactions of the primary proton galactic cosmic ray spectrum in the atmosphere. In [60], ground level spectra were generated with Geant4, MCNPX, and Fluka showing general agreement between the codes. ATMOCOSMICS is a Geant4 application that can compute the secondary particle spectra [61]. TIERRAS is an AIRES application that is tailored to supporting underground physics experiments [62]. MUPAGE is a HEMAS application that is tailored to evaluate muon events for neutrino detectors [63]. The Qinetic Atmospheric Response Model (QARM) precomputes a matrix allowing for the prediction of an environment in time and location [64, 65]. EXPACS is also a parameterized model [66] that uses the results of PARMA, a PHITS application [67]. In the following sections, the environment generated by EXPACS is examined as it will be used in the remaining Chapters to assess error rates. The energy spectra for a sea level New York City location are shown in 18 and provided in Appendix A.

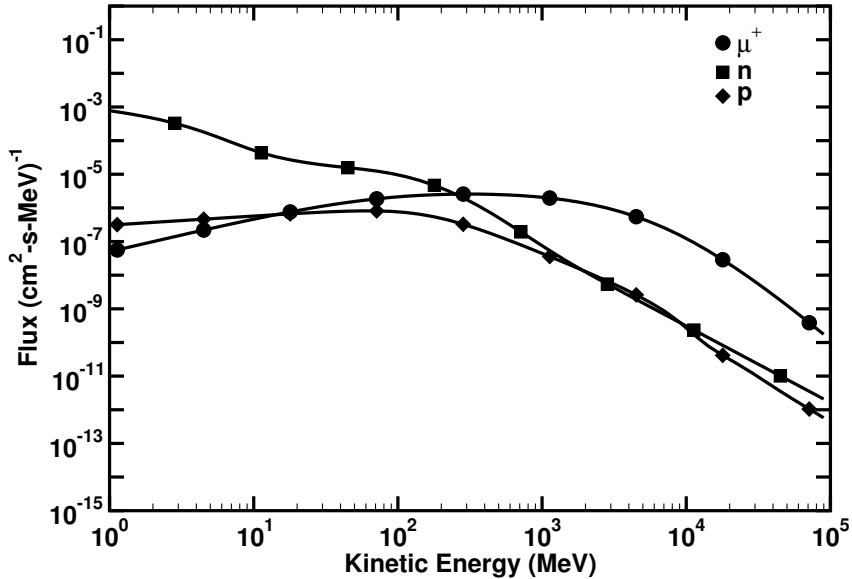


Figure 18: Sea level environment at  $40^\circ$  latitude,  $73^\circ$  longitude, and 0 ft. elevation generated by PARMA and extracted from EXPACS.

## Neutron Component

The terrestrial neutron spectrum spans an energy range from thermal to multiple GeV. For radiation effects in microelectronics, the spectrum above 1 MeV has been extensively studied and standards for assessing the environment agreed upon. The data set that forms the basis of the JEDEC 89A standard environment [5] was published in [68]. As the measurements were made with a Bonner sphere, the data reported represent an omnidirectional spectrum. In fact, the neutron flux is directed toward the ground, but for modeling purposes, the directionality is often ignored. Details of the environment are reported elsewhere.

The neutron flux has been shown to vary with the solar cycle. This is a result of the difference in the GCR flux that reaches the atmosphere during solar minimum and solar maximum periods. Figure 19 shows the monthly sunspot number, an indication of solar activity overlaid on data obtained from the Climax Neutron Monitor. The variation with solar cycle should be expected to hold true for other particle types as well.

## Proton Component

The proton component of the terrestrial environment has been measured by various investigators with momentum cloud chambers and magnetic spectrometers. Much of the data in literature report on high-momentum protons ( $> 100 \text{ MeV}/c$ ). It should also be noted that the majority of measurements are reported for the vertical proton intensity. Figure 20 shows the proton intensity as reported by [70, 71, 72]. When converted to vertical momentum intensities, the EXPACS proton flux spectrum shows good agreement to measurements over most of the momentum range. The conversion

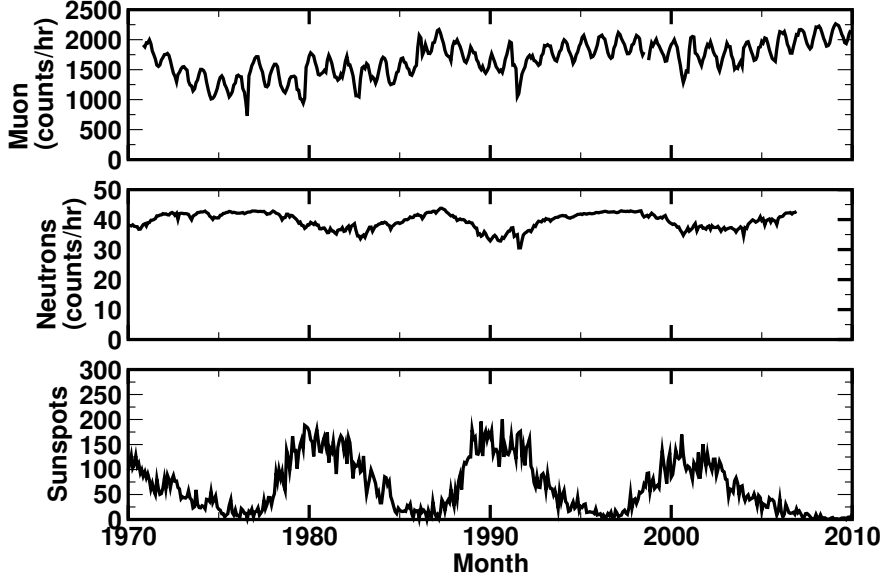


Figure 19: Correlation between the solar activity and counts reported by the Climax Neutron Monitor and Nagoya Muon Station [69].

utilizes Equation 13 with an  $n$  parameter of 3.2 according to [73].

#### Muon Component

Investigations into the muon component of the terrestrial environment have also been performed using muon telescopes and nuclear emulsions. The variation in the count rate can be seen in Figure 19. Data obtained from the Nagoya muon station [69] show a strong annual variation with peaks occurring during the winter months. However, because of the apparatus used, almost no data are available in open literature to estimate the muon flux at low momenta. Figure 21 shows muon momenta intensity measured at sea level. When converted to vertical momentum intensities, the EX-PACS muon flux spectrum shows good agreement over most of the momentum range. The conversion utilizes Equation 13 with an  $n$  parameter of 4.7 according to [74].

A number of studies performed between the 1950's and the 1970's measured the rate of stopping muons as a function of depth beneath the Earth. Generally, these

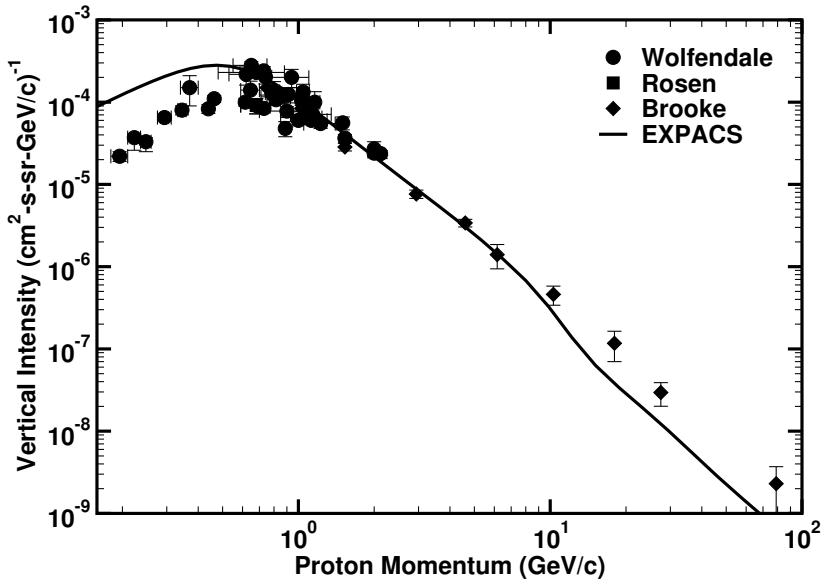


Figure 20: Differential proton momentum spectrum at sea level. Digitized from [70, 71, 72]. Comparison to EXPACS model also provided.

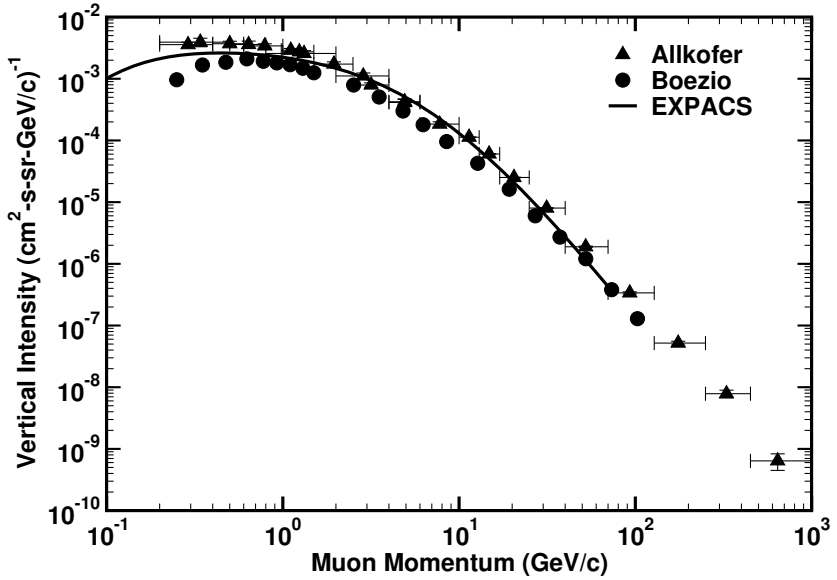


Figure 21: Differential muon momentum spectrum at sea level. Digitized from [75, 76]. Comparison to EXPACS model also provided.

studies involved the creation and placement of a nuclear emulsion at various subterranean locations. In many cases, these were Ilford G5 nuclear emulsions. After the emulsions had been exposed for a given period of time, they were scanned for signs of muon decays. The number of stopping muons was then used to estimate the rate of stopping muons at the depth, in units of meters water equivalent. A compilation of published data are presented in Figure 22.

Since no measured data on the low-energy muon energy spectra have been located in the literature, the muon stopping data sets are an important point of validation for any model. A comparison is drawn between the data and the energy spectra obtained from EXPACS. Using range tables for silicon, the differential flux with respect to energy ( $\text{cm}^2\text{-s-MeV}$ ) $^{-1}$  is converted to a differential flux with respect to range ( $\text{cm}^3\text{-s}$ ) $^{-1}$ . After a normalization of units, these values are overlayed on the stopping muon data in Figure 22. The immediate agreement is fair and expected to improve upon consideration of the axes. As the measured data represent stopping in a nuclear emulsion with a different atomic composition and greater density, it is expected that the silicon stopping rate should be less than that of an emulsion. In addition, the results are reported as depth in silicon instead of water and have the effect of stretching data towards greater depths. Under these considerations, the model spectrum appears quite reasonable.

### Conclusions

All environments present a threat to the reliable use of microelectronics due to ionizing radiation. It is therefore important that the components of the environment

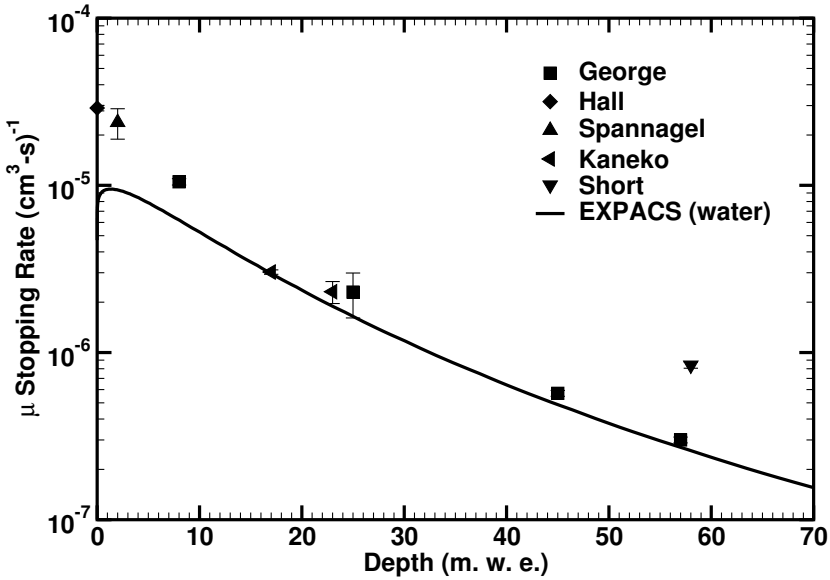


Figure 22: The rate of stopping muons measured at various depth underground [77, 78, 79, 80, 81]. Comparision to EXPACS model also provided.

are characterized. The reliability community has done this well for much of the terrestrial and space environments providing standards for the evaluation of the effects of altitude and latitude, as well as the natural variability. Unfortunately, the characterization has focused on the flux spectra of heavy ions and high-energy protons in space and neutrons on Earth. The historical absence of a need for the low-energy proton and muon environments has not motivated the characterization of these components of operating environments. For a comprehensive approach to radiation effects, a model of the full environment should be considered.

## CHAPTER IV

### ACCELERATED TESTING

The evaluation of a part's radiation response is often an undertaking that requires an accelerated test condition which can enhance the speed at which a failure mechanism presents itself. Under a controlled environment, the statistics of the experiment are greater than what can be estimated from on-orbit or in-field operation. Further, the inability to identify a part that is not suitable for the intended radiation environment will present extraneous costs to the mission or corporation, if not complete failure of the system.

Accelerated testing for single event effects involves measuring an event cross-section (i.e., the probability of event occurrence). A particle accelerator is used to produce an enhanced flux environment. Ideally, the beam is monochromatic, presenting the part with a particular species and a nearly single-valued kinetic energy, although specialized facilities are capable of reproducing the shape of the energy spectrum of natural environments.

In single event upset testing, the part, usually a memory, is placed in front of the beam and irradiated while retaining data. After the irradiation, the memory is checked for bit errors. If the device is sensitive to the incident radiation, the number of errors observed during the test,  $N$ , will directly depend on the beam fluence,  $\phi \text{ cm}^{-2}$ .

In some cases, the memory is a test array that is not production ready. The yield of these memories may be low or unstable bits in the array may be present. Even in the absence of radiation, after a write to the array, a read will uncover bits in error.

If the number of bad bits is comparable to the number of single event upsets during a test run, they will introduce a bias into the measured cross section.

This can provide a systematic background error that must be accounted for during the data analysis. If the number of bad bits can be measured and shown to be independent of the time between the read and write, their effect can be removed from the data. This implies that bad bits do not accumulate with time. Since the number of bad bits may fluctuate as bits randomly flip, measurements will have a probabilistic distribution. The mean value of the distribution will be referred to as  $\mu_B$  and the variance of the sample distribution as  $s_B^2$  to prevent confusion with the SEU cross section  $\sigma_{SEU}$ . In this case, the variance and cross section of the number of upsets can be calculated as:

$$s_{SEU}^2 = |N - \mu_B| + s_B^2 \quad (14)$$

$$\sigma_{SEU} = \frac{|N - \mu_B| \pm s_{SEU}}{\phi} \quad (15)$$

The SEU cross section is not only a result of the area presented by the target, but also captures the probability that the particle deposits sufficient energy to evoke an upset in the circuit. For unlikely particle interactions in the semiconductor material to induce an upset, the SEU cross section is much smaller than the physical features of the device. This is the case for neutron and high-energy proton-induced events. The measured cross section is most useful as a function of the particle kinetic energy, although for heavy ion irradiation, the particle LET is commonly used.

### Devices Under Test

SRAMs fabricated in different process technologies from various manufacturers were used to investigate the effects of singly-charged particles. Table 3 provides details of each part. The Texas Instruments 65 nm memory consists of three variations on a 6-transistor cell design. In most datasets, cross sections for all 8 Mbits are reported unless otherwise noted. The memory was bonded as a chip-on-board and has  $5 \mu\text{m}$  of material on top of the metal interconnects. Both of these characteristics allow for easier front-side testing. Similarly, the Texas Instruments 45 nm memory consisted of banks with variations on the distance to well contacts. The memory was bonded to a ZIF socket and has  $7.5 \mu\text{m}$  of material on top of the metal interconnects. Both parts from Texas Instruments were biased at their nominal supply voltage of 1.2 V. unless otherwise noted. Each of the daughtercards was operated by a Field Programmable Gate Array (FPGA) tester designed by NASA Goddard Space Flight Center.

The composition of the Marvell Semiconductor memories is not known, although the parts were “delidded” for testing. The 55 nm and 40 nm generation devices were 1 Mb and 5 Mb arrays, respectively, and the supply voltage for these devices was 1.0 V.

Table 3: Device Under Test

Manufacturer	Process	Size
Texas Instruments	65 nm bulk CMOS	8 Mbit
Texas Instruments	45 nm bulk CMOS	8 Mbit
Marvell Semiconductor	55 nm bulk CMOS	1 Mbit
Marvell Semiconductor	40 nm bulk CMOS	5 Mbit

The 65 nm SRAM was characterized versus supply voltage to establish a baseline for background errors. For each bias, the mean  $\mu_B$  and standard deviation  $s_B$  are

reported in Table 4. The other SRAMs did not experience background errors when operated at 1.0 V.

Table 4: Baseline error counts characterized versus bias for 65 nm SRAM

Bias (V)	Runs	$\mu_B$	$s_B$
0.8	3	125.000	44.952
0.9	10	37.100	13.641
1.0	17	19.353	4.934
1.1	16	8.375	2.260
1.2	10	5.100	2.022

### Heavy Ion Accelerated Tests

#### Accelerated Test Setup

Heavy ion SEU data were acquired for the Texas Instruments 65 and 45 nm SRAMs using the facilities at the Lawrence Berkeley National Laboratories (LBNL) and Texas A&M University (TAMU). Both facilities use a cyclotron to accelerate ions to the device under test. The LBNL cyclotron offers a cocktail of ions up to 30 MeV/nucleon, although experimental beams up to 32 MeV/nucleon are available and were used for this experiment. The TAMU cyclotron offers ions up to 40 MeV/nucleon which allows testing with ions with lower LET.

The choices of ion species and energy for the 65 and 45 nm memories are listed in Tables 5 and 6, respectively. The 45 nm memory was not available for the test opportunity at TAMU so we do not have data at  $\text{LET} < 1 \text{ MeV-cm}^2/\text{mg}$ . In many test campaigns, these data are not collected because of limited resources for testing at high-energy facilities. The data collected on the 45 nm memory is as complete as is often acquired. For arguments presented later, the low-LET cross sections have

considerable value to accurate rate predictions. The other parts did not participate in either test.

Table 5: Texas Instruments 65 nm Experimental Ion Species and Energies

Species	Energy MeV/u	Facility	LET MeV-cm <sup>2</sup> /mg	Range in Si μm
He	15	TAMU	0.1	1440
He	6.3	TAMU	0.2	317
N	40	TAMU	0.6	2350
N	32	TAMU	0.7	1580
B	10	LBNL	0.9	306
Ne	40	TAMU	1.2	1710
Ne	13.5	TAMU	2.8	259
Ne	10	LBNL	3.5	162
Ar	40	TAMU	3.9	1070
Ar	12.6	TAMU	8.6	179
Ar	10	LBNL	9.7	130
Cu	10	LBNL	21.2	103
Kr	11.3	TAMU	28.9	119
Kr	10	LBNL	30.9	104

Table 6: Texas Instruments 45 nm Experimental Ion Species and Energies

Species	Energy MeV/u	Facility	LET MeV-cm <sup>2</sup> /mg	Range in Si μm
B	10	LBNL	0.89	315
O	10	LBNL	2.19	195
Ne	10	LBNL	3.49	163
Ar	10	LBNL	9.74	130

### Accelerated Test Results

The data collected on the two memories are presented in Figure 23 and 24. Both curves demonstrate a similar shape over the range of LET values tested. Because the electronic stopping of a high-LET ion generates sufficient charge to upset the memory cells as it passes through the circuit transistors, the measured cross section is comparable to physical features such as reverse-biased drains. At even greater values

of LET, diffusion and multiple cell effects contribute to larger cross sections. At low-LET, a threshold for direct ionization upsets causes the measured cross sections to diminish until other effects like nuclear reactions from high-energy, low-LET ions, if they are significant, define the cross section.

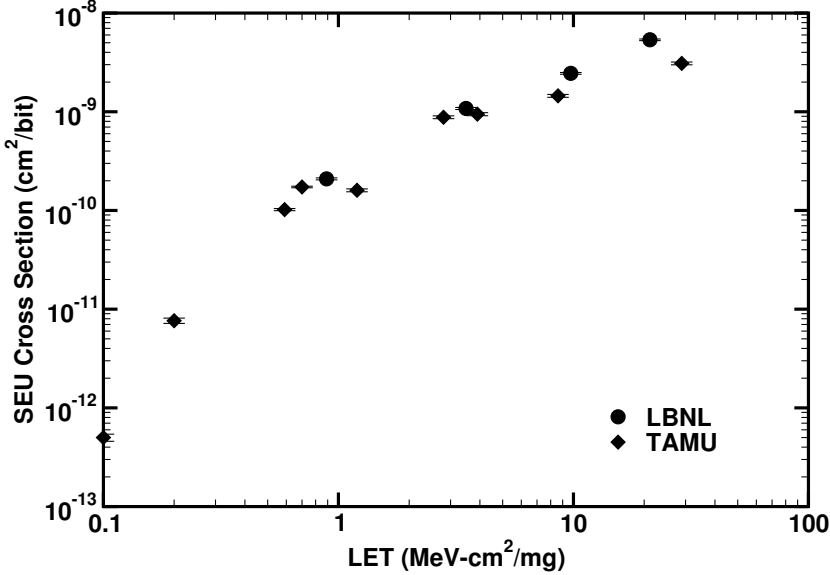


Figure 23: Heavy ion single event upset cross sections for the Texas Instruments 65 nm SRAM measured at LBNL and TAMU.

Figure 23 demonstrates that the 65 nm memory has an exceptionally low LET threshold compared to older technologies. In fact, this effect is not a weakness of this particular part, but has been reported in many other tests of similar technologies. Extrapolation of the data on the 45 nm memory also suggests an  $\text{LET}_{\text{th}} < 1 \text{ MeV-cm}^2/\text{mg}$ .

The dominant mechanism causing upsets with He at 0.1 and 0.2 MeV-cm<sup>2</sup>/mg is unclear. It may be the result of weak bits, LET variability, nuclear reactions, or some mix of causes. The data obtained with N at 0.6 and 0.7 MeV-cm<sup>2</sup>/mg are relatively large cross section values. Single bit upset cross sections greater than  $1 \times 10^{-10} \text{ cm}^2$  are likely the result of direct ionization on an area of the cell of 100 nm × 100 nm.

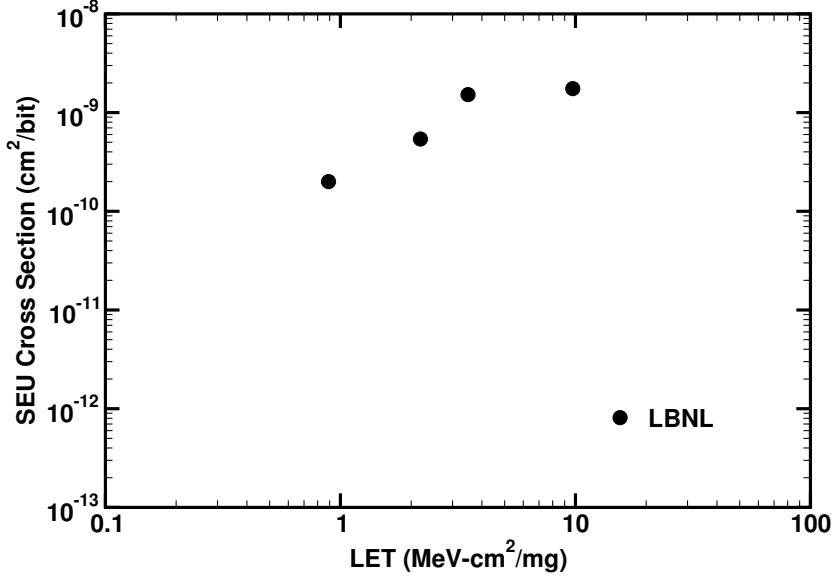


Figure 24: Heavy ion single event upset cross sections for the Texas Instruments 45 nm SRAM measured at LBNL.

Therefore direct ionization processes are probably only beginning to fall off in the 0.5 MeV-cm<sup>2</sup>/mg regime. As shown in Chapter II, protons, muons, and other singly-charged particles have a maximum LET of approximately 0.5 MeV-cm<sup>2</sup>/mg. Datasets such as this one demonstrate that a sensitivity to singly-charged particles may exist for the device under test and acquisition of other datasets is warranted.

In practice, heavy ion testing has found little use in the terrestrial community since the flux is nearly negligible at the ground level. Space-bound parts that have heavy ion data sets with an  $\text{LET}_{\text{th}} < 1 \text{ MeV-cm}^2/\text{mg}$  should additionally have low-energy proton tests performed for proton-rich orbits.

### Accelerated Test Setup

Proton single event upset data were collected for the Texas Instruments 65 and 45 nm memories over a wide energy range at four facilities. The cyclotron at Indiana University [82] was used to obtain cross sections at 198 and 98 MeV. A 63.3 MeV proton beam at UC Davis [83] was used (with degraders) to obtain data as low as 19.8 MeV and a 14.6 MeV primary beam was degraded to obtain data down to 2.6 MeV. The low-energy ( $< 2$  MeV) data were acquired at NASA GSFC's Van de Graaff facility. The LBNL cyclotron was used to confirm the measured proton cross section at 32.5 MeV. Additionally a 6 MeV H<sub>2</sub>+ beam was broken up and degraded through air to obtain a proton spectrum with a peak as low as 1.2 MeV.

Figure 25 shows the proton energy spectrum at LBNL measured with a surface barrier detector. The 1.2 MeV beam was used in the test on the 65 nm SRAM. The 1.7 and 1.4 MeV beams were measured with a different calorimetry setup at a later date and therefore appear less well-defined. These beams were used to test the 45 nm SRAM. The spectrum demonstrates that the dosimetry is one difficulty associated with low-energy proton testing. In order to measure the flux during a test, the counts on the SBD were used to calibrate the counts observed on the photo multiplier tubes upstream.

Similar difficulties arose with the tests performed at UC Davis. The primary beams used were 63.3 MeV and 14.6 MeV. Other energies were obtained through the use of degraders. The composition and thickness of the degraders were modeled and simulated in MRED to obtain the energy spectrum observed by the part. Figure 26

shows the result of the simulations.

A similar analysis was performed for the TRIUMF 65 MeV proton beam, although no test data were obtained with this beam line. The beam line at TRIUMF is another possible choice for moderate proton energies therefore an analysis has been included at the end of the chapter. Low energy tests could be developed to use this beam line.

Whether the tests were performed with the cyclotron at UC Davis or TRIUMF, a degraded beam has some undesirable characteristics. In the simulations of a 60+ MeV beam degraded to less than 20 MeV, the distribution of incident energies is very broad. Although no beam is truly monochromatic, the range of energies produced by this setup may cover a region of the device response that is rapidly changing with energy.

The setup for low-energy proton tests at LBNL required that the test be performed in air rather than in the vacuum chamber. Since protons at these energies have very limited range, the device was placed as close to the beam window as possible as shown in Figure 27. The effect of the air introduces straggling and systematic error in the cross section measurement.

## Accelerated Test Results

The experimental proton-induced SEU cross section curves for the 65 and 45 nm memories are shown in Figures 28 and 29, respectively. The cross section measurements at proton energies above 10 MeV look similar to almost any other part. The value is nearly constant up to the highest energies tested. This portion of the curve is dominated by particle-reaction-induced events since at these energies protons are well above the Coulomb barrier. A proton that strikes a nucleus near the active region of an SRAM cell causes secondary charged particles to ionize the material and generate

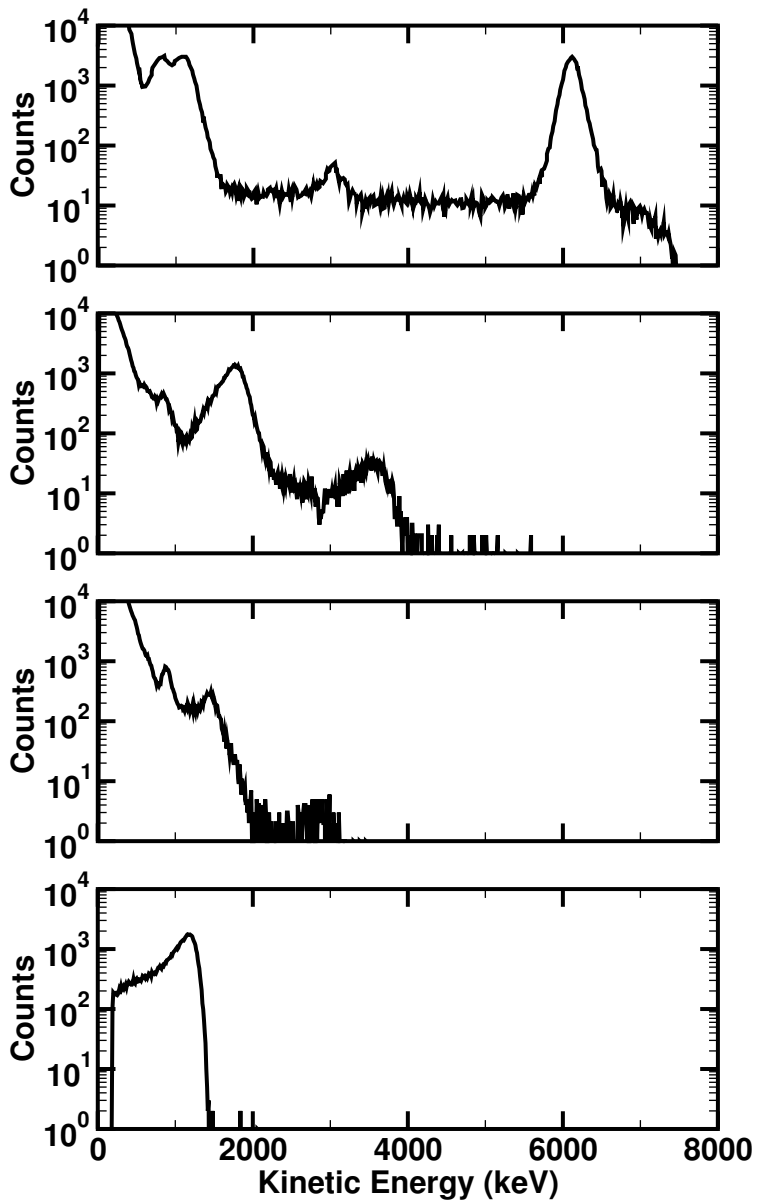


Figure 25: The low-energy proton spectrum at the Lawrence Berkeley National Laboratories measured by a surface barrier detector with a multi-channel analyzer. The top plot captures the energy distribution of the 6 MeV diatomic  $\text{H}_2^+$  beam as measured in September 2009. The plot second from the top shows the 1.7 MeV beam. The plot second from the bottom shows the 1.4 MeV beam. The bottom plot shows the 1.2 MeV beam measured in October 2008.

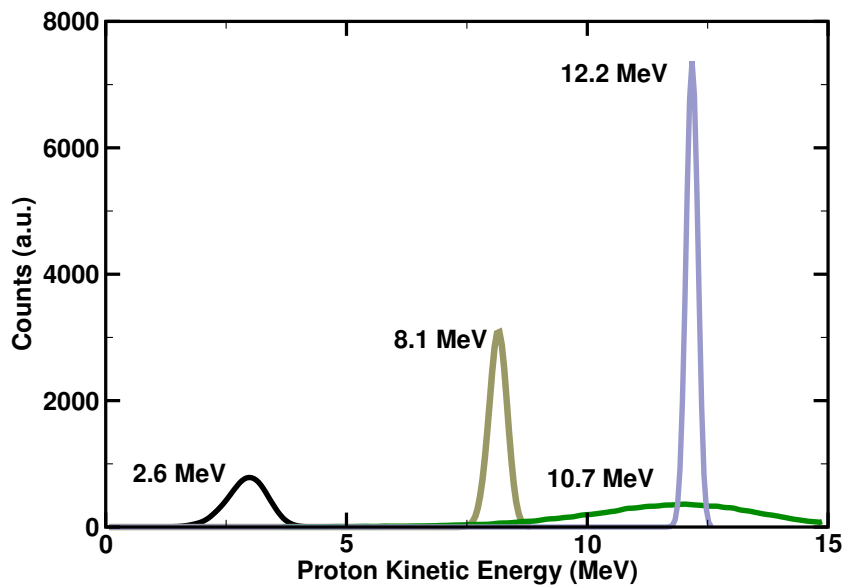


Figure 26: Simulated kinetic energy spectra of a 14.6 MeV tune degraded to achieve mean values of 2.6, 8.1, and 12.2 and a 63.3 MeV tune degraded to 10.7 MeV.

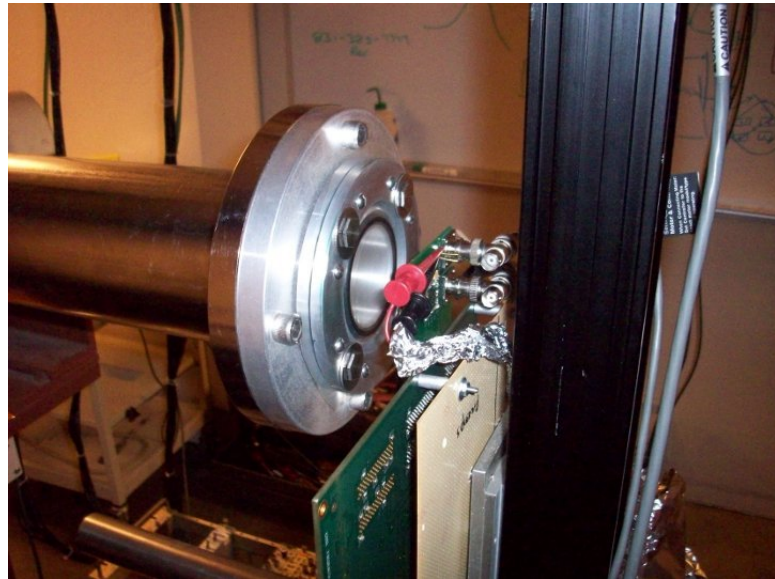


Figure 27: Texas Instruments 65 nm SRAM in the beam line at the Lawrence Berkeley National Laboratories. Distance between the device and beam window was minimized because of proton range and energy straggling in air.

enough charge to upset the circuit. The cross section is consistent with what one would expect from nuclear reaction events. Assuming a one micrometer collection depth, and a  $0.5 \times 10^{-8} \text{ cm}^2$  cell area, applying Equation 3 yields  $5 \times 10^{-14} \text{ cm}^2$ .

Classical proton and neutron cross sections roll off at energies of 10 MeV or higher. Neither of these datasets does. Between 2 and 10 MeV the cross sections appear slightly elevated from the values at higher energies. As discussed in Chapter II, protons at this energy are nearing the Coulomb barrier which prevents the particle from initiating a particle reaction. Instead the proton is likely displacing a silicon or oxygen nucleus from the crystal lattice through an elastic scattering event. It is also possible that some enhancement in the cross section was caused by the degrading of the beam.

At energies below 2 MeV the proton cross-section curves demonstrate the characteristics expected when direct ionization dominates the other upset mechanisms. The beam energy is below the Coulomb barrier for the common materials and the range of the recoil is increasingly limited. The three orders of magnitude increase in cross section going from high energy ( $> 10 \text{ MeV}$ ) to low energy ( $< 2 \text{ MeV}$ ) indicates a clear transition from upsets due to nuclear elastic and inelastic events to direct ionization. At these low energies, the proton cross section is on the order of the dimensions of the physical features of the cell, consistent with direct ionization.

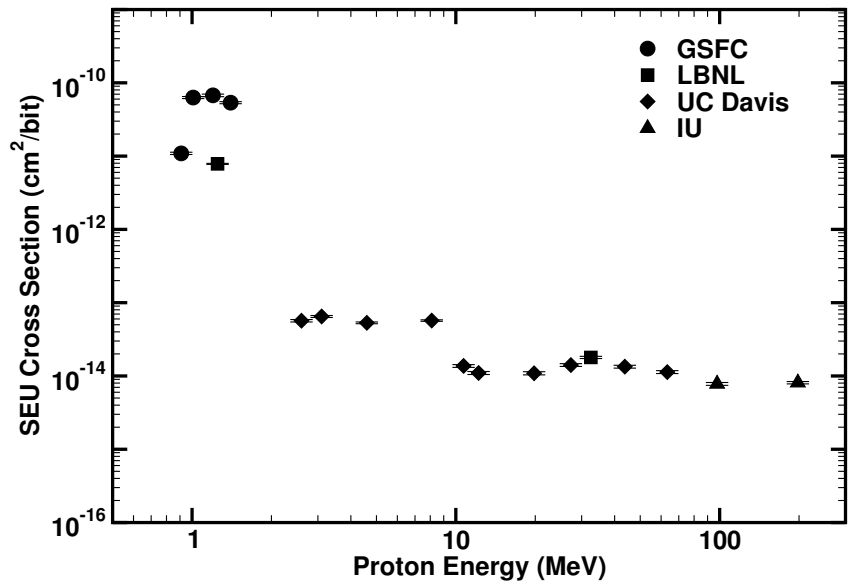


Figure 28: Proton single event upset cross-section curve for the Texas Instruments 65 nm SRAM. Proton datasets with dramatic increases in cross section are not amenable to traditional rate prediction models.

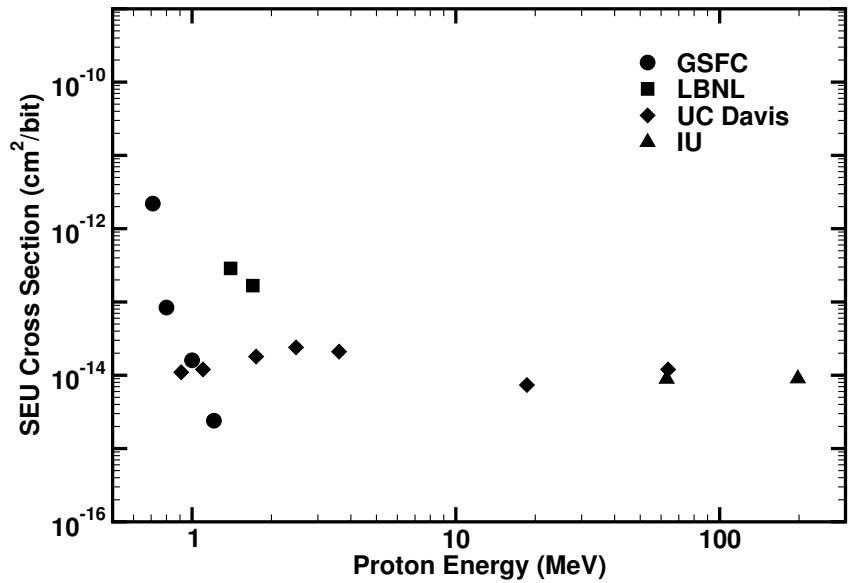


Figure 29: Proton single event upset cross-section curve for the Texas Instruments 45 nm SRAM. Proton datasets with dramatic increases in cross section are not amenable to traditional rate prediction models.

## Muon Accelerated Testing

### Accelerated Test Setup

To investigate the effects of low-energy muons on the reliability of microelectronics, we sought the use of a surface muon beam line. The list of candidates is very limited. The muon source requires the accompaniment of a high-energy proton beam. A search for possible facilities provided the candidates in Table 7.

Table 7: Facilities Offering Muon Sources

Facility	Location
TRIUMF	Vancouver, British Columbia
Paul Scherrer	Villigen, Switzerland
ISIS, Appleton Laboratory	Oxfordshire, United Kingdom
KEK	Japan
JINR	Dubna, Russia
RIKEN	Hirosawa, Japan

In this work, we performed accelerated tests with the M20B beam line at TRIUMF [84]. This facility produces surface muons (positive muons from the decay of stopped pions near the surface of the production target [85]) for scientific research. A diagram of the beam line is shown in Figure 31. The meson production begins with a 100  $\mu\text{A}$  500 MeV proton beam BL1A focused on the production target 1AT2 consisting of 10 cm of beryllium. Pions are produced within the target and decay with a lifetime of 26 ns into a muon and neutrino. Although both  $\pi^+$  and  $\pi^-$  are produced, the  $\pi^-$  are mostly captured within the target and do not decay into  $\mu^-$ . The remaining  $\mu^+$  surface muons have an initial kinetic energy of 4.1 MeV (30 MeV/c momentum) and are transported downstream to the beam line. The facility provides the user control

over a dipole magnet (M20B1) to select particle momentum, followed by variable-width slits (M20SL1) for refinement. Following a second bending magnet (M20B2), an electrostatic separator (M20BSEP) provides velocity selection. Finally, a second set of slits (M20BSL2) is used for collimation and the beam is brought to the final focus.

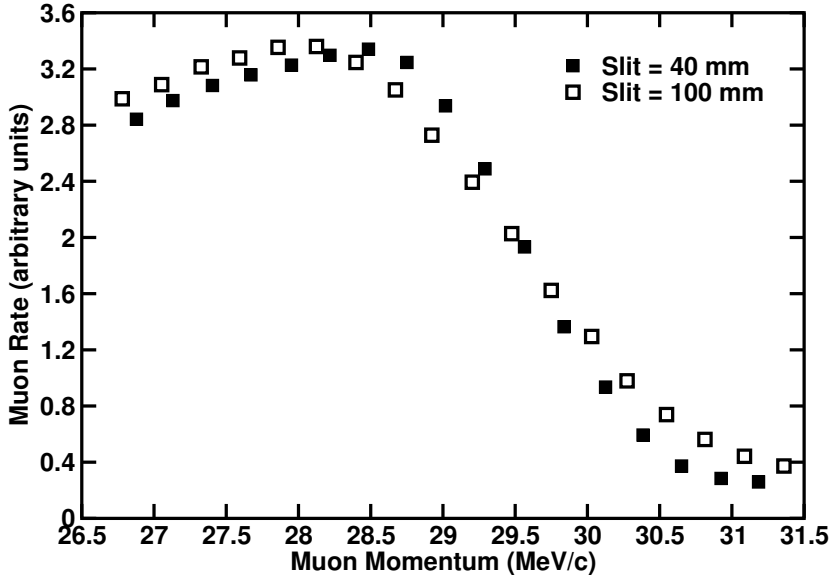


Figure 30: The surface muon momentum produced by the M20B beamline at TRI-UMF [86].

Given the momentum and velocity selections in the beam line and the energy deposition in a surface barrier detector (discussed in the following subsection) the mass of the accelerated particles is known to be  $106 \text{ MeV}/c^2$ . Positively-charged particles of different mass such as pions ( $140 \text{ MeV}/c^2$ ) and protons ( $938 \text{ MeV}/c^2$ ) are clearly eliminated. For instance, 420 keV protons match the  $28 \text{ MeV}/c$  channel momentum but are deflected away in the electrostatic separator. Similarly, pions are removed by the separator and further decay with a mean decay length of about 2 m. After traversing the 20 m channel length all pions are eliminated.

Positrons, while deflected by the magnets and separators upstream, are present

downstream in the beam from muon decay. These particles deposit very little energy through electronic stopping and rarely interact through annihilation. The fact that the final particles range out as expected and produce positrons when they decay shows that the beam indeed consists of  $\mu^+$ . Final confirmation of particle species is provided by many muon spin rotation experiments [85] that look at the depolarization pattern of muons using a spectrometer.

To provide dosimetry, a collimator with a 2.5 cm diameter aperture was placed at the beam line window and a scintillator positioned 1 cm from the window. At full momentum, a flux of  $2 \times 10^6 \mu^+ s^{-1}$  can be obtained in a 4 cm  $\times$  3 cm spot size; however, as the momentum selection is reduced, the flux is reduced. The presence of the scintillator further lowered the mean beam energy and broadened the energy distribution. The device under test was placed at normal incidence 3 cm behind the scintillator.

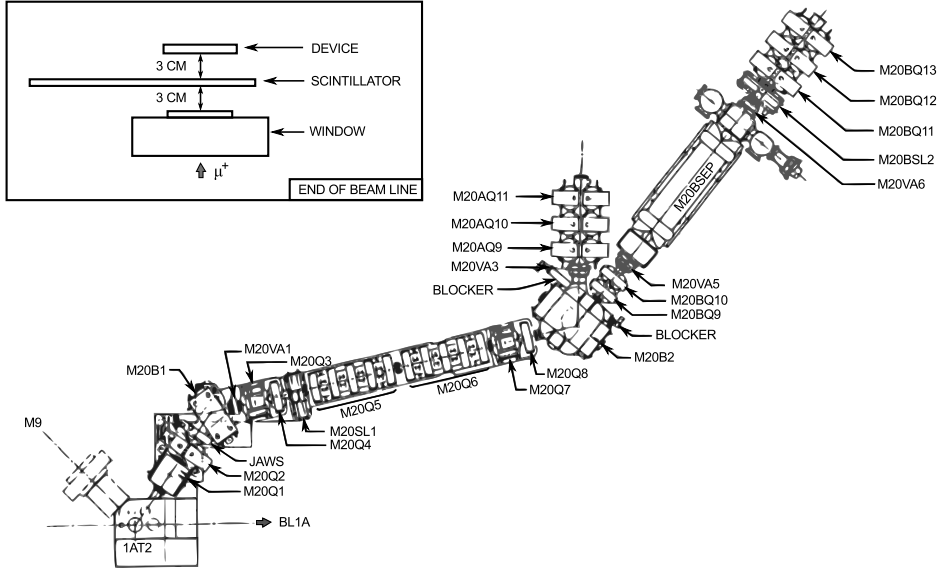


Figure 31: The M20 beam line at TRIUMF. Muon selection is performed through the use of bending magnets and an electrostatic separator. Reproduced from [84]. Inset illustrates the position of test setup at the end of the beam line.

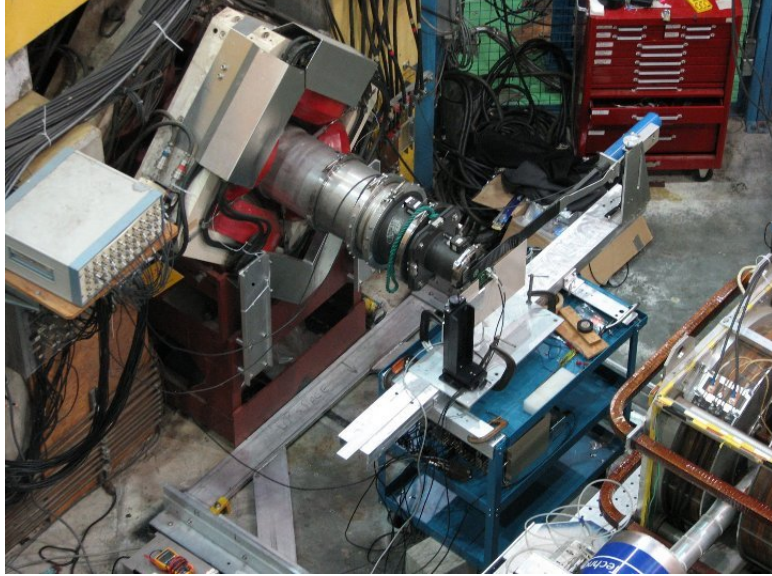


Figure 32: The Texas Instruments 65 nm SRAM in the M20B beamline at TRIUMF.

### Experimental Validation

To characterize the beam, a  $500 \mu\text{m}$  thick fully-depleted surface barrier detector (SBD) was used in a pulse height analysis to measure the energy of the particles. The detector was enclosed within an aluminum box 3 cm downstream of the scintillator with a  $4 \mu\text{m}$  aluminized mylar window in the beam line. The detector was thick enough to stop all of the muons after the scintillator, so the SBD was an effective tool in characterizing the muon kinetic energy spectra. The dipole magnet M20B1 was adjusted to select muons with momentum lower than 28 MeV/c and the M20SL1 slits were opened to 20 mm. The M20BSL2 slits were not used during the test. The resulting energy deposition provides an adequate characterization of the kinetic energy as well as energy loss and straggling of the beam in the scintillator and other materials.

The top plot in Figure 34 shows the deposited energy spectra as measured with the SBD at various momentum selections. At full momentum, the mean energy

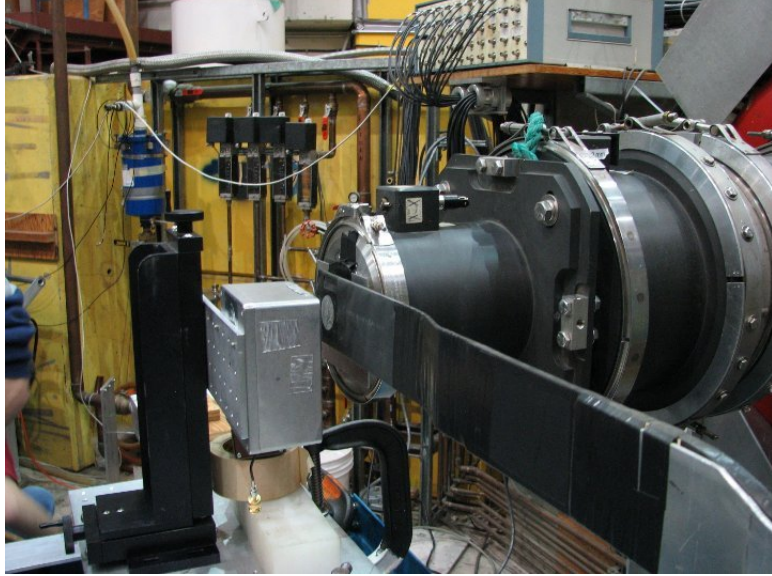


Figure 33: The surface barrier detector in the M20B beamline at TRIUMF. Distance between the device and beam window was minimized because of muon range and energy straggling.

deposition in the SBD is slightly greater than 3 MeV whereas the initial kinetic energy is 3.6 MeV for a 28 MeV/c muon. This indicates that some energy has been lost in the passage through the materials between the final velocity selection and the device. As the momentum is decreased, the corresponding peak energy deposited by the stopping particles decreases. The low-energy contribution below 500 keV, which is seen in each spectrum, is most likely produced by positrons from  $\mu^+$  decay. With the magnet settings set to 21.6 MeV/c, the muon peak is barely distinguishable from the positron peak, and by 20 MeV/c the muon peak was completely indistinguishable. It is important to note that even though there are positrons in the beam, positrons cause significantly less energy deposition per unit path length than muons.

A Geant4 application was used to investigate the energy deposition of muons in the detector. A muon beam with a 4% standard deviation in momentum was transported through a scintillator layer of CH<sub>2</sub> with an assumed thickness of 250  $\mu\text{m}$ . Air gaps,

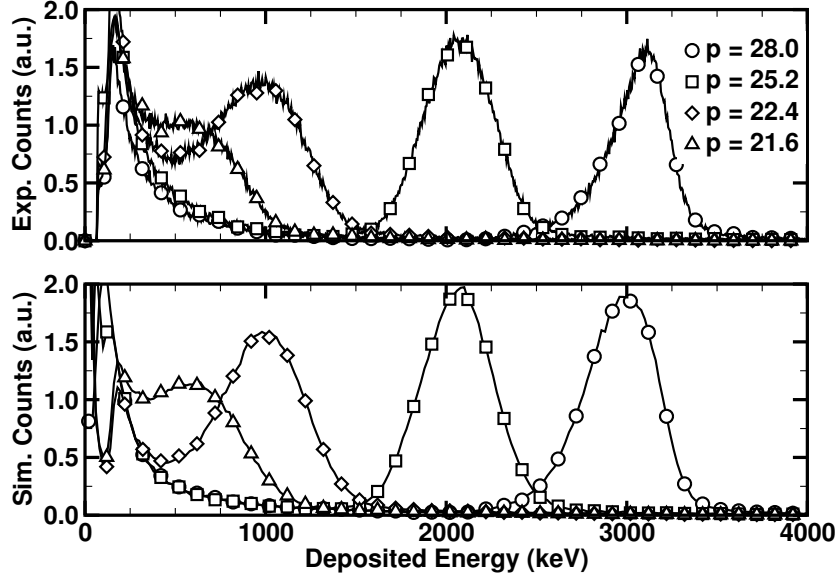


Figure 34: Experimental (top) and simulated (bottom) energy deposition counts in 500  $\mu\text{m}$  surface barrier detector.

the mylar window, and the SBD were included. Figure 34 shows the results of the simulation compared with experimental data. Reducing the initial kinetic energy to the respective experimental condition and simulating the energy deposition in the SBD yields good agreement with measurements. The centroids shift appropriately and the positron contribution can be seen in the low energy bins. The agreement of simulation results provides final confirmation that energy deposition at final beam focus is caused by the stopping of muons. This virtual beam line will be used to interpret the SRAM results.

### Accelerated Test Results

A second set of Geant4 simulations was performed to characterize the muon kinetic energy spectra for the experimental momentum selections. In these simulations muons were transported through the scintillator and positrons were destroyed upon creation. The kinetic energy spectra at the surface of the SRAMs are shown in the bottom plot

in Figure 35. Given the prior agreement with the data acquired with the SBD, the simulation results provide a reasonable estimate of the incident beam.

The upset probability versus momentum measurements are presented in the top plot of Figure 35. The abscissa is related to the kinetic energy by associating the upsets at the mode value of the simulated energy distribution. An approximate event cross section is indicated based on an estimate of the beam fluence. All SRAMs were operated at a supply voltage of 1.0 V. This bias was chosen because it produced a statistically significant error count.

At the highest energy, 3 MeV, the upset count was indistinguishable from the baseline for the 65 nm device. This was because muons pass through the device without generating sufficient charge to result in an SEU. Additionally, this measurement confirms that reported upsets cannot be attributed to noise sources while the beam is in operation. Near 700 keV the range of the beam through the metallization is such that a large portion of the muons traversing the active silicon are close to the Bragg peak and the collected charge is sufficient to exceed the critical charge. As the mean energy is further decreased, the beam begins to range out and the error counts return to the baseline. The 45 nm and 40 nm devices were spot checked and also exhibited muon sensitivities.

Figure 36 shows the 65 nm device SEU response versus supply voltage for a distribution centered around 400 keV. At the nominal operating voltage of 1.2 V, few errors are attributed to muon upsets. However, as the voltage is reduced, the number of muon-induced upsets increases. The reduction in voltage corresponds to a reduction in critical charge. Therefore we expect that a greater range of muon energies are capable of inducing SEU at reduced bias.

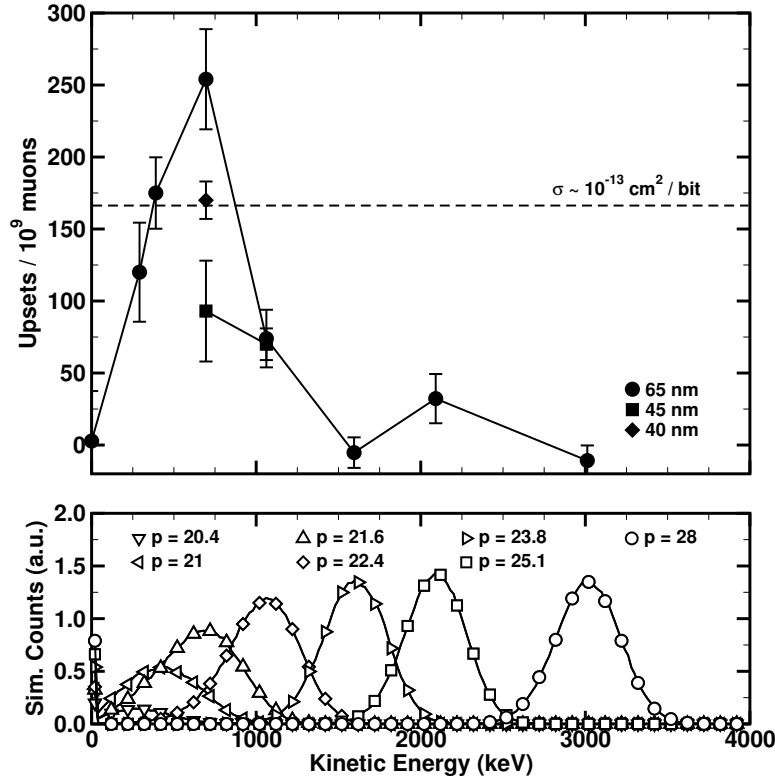


Figure 35: Simulated muon kinetic energy distributions, as seen at the front of the part, corresponding to experimental momenta including upstream energy losses and straggling (bottom). Error counts for 65 nm, 45 nm, and 40 nm SRAMs versus estimated muon kinetic energy at 1.0 V bias (top). Dashed horizontal line represents an approximate muon-induced SEU cross section for reference.

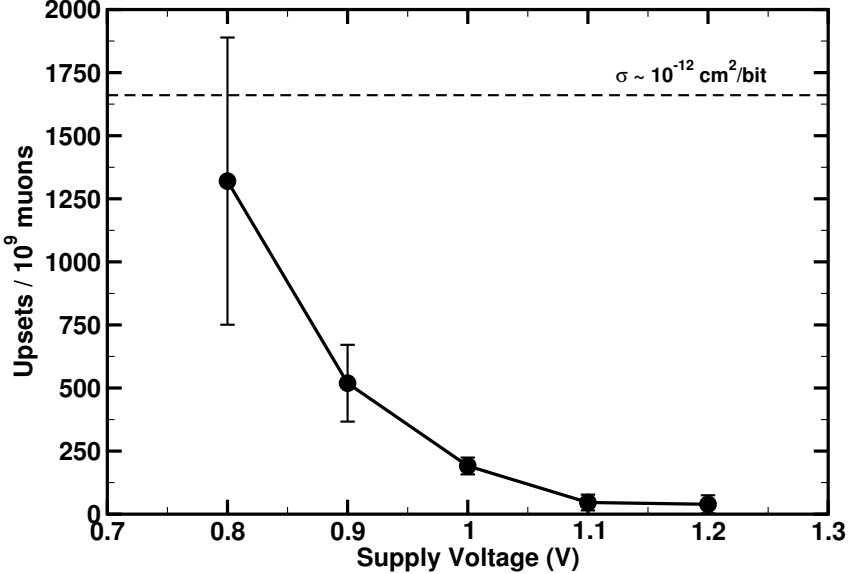


Figure 36: Error counts for 65 nm SRAM versus supply voltage for approximately 400 keV muons produced by 21 MeV/c momennum selection. Dashed horizontal line represents an approximate muon-induced SEU cross section for reference.

Data were collected over interspersed reads with the beam on and off to monitor any drift in the background errors. This baseline error count was verified to be independent of exposure time and is thought to be the result of unstable bits being operated below the recommended bias. Error counts in Table 8 are presented as the number of incorrect bits read exceeding the baseline errors. Error bars in Figures 35 and 36 represent the standard deviation of the upset count after removing the measured distribution of baseline errors according to Equation 14.

#### Effect of technology

The data presented in Figure 37 show the probability of upset at nominal bias. All four SRAMs were irradiated using the 21.6 MeV/c  $\mu^+$  beam. The probabilities are presented as the number of upsets per  $10^9$  muons counted by the scintillator and scaled by the memory capacity. We have refrained from presenting the data as SEU

Table 8: Single event upset counts for 65 nm SRAM

Bias (V)	P (MeV/c)	Runs	N	Muons ( $\times 10^6$ )	SEU (per $10^9 \mu$ )	$s_{\text{SEU}}$
0.8	21.0	1	232	81.0	1321	569
0.8	22.4	1	179	113	478	403
0.9	21.0	1	89	100	519	154
0.9	21.6	1	70	56.0	588	264
1.0	19.6	3	62	144	27.3	60.8
1.0	20.4	3	86	204	137	49.3
1.0	21.0	6	204	461	191	33.2
1.0	21.6	4	175	382	255	36.5
1.0	22.4	3	88	357	83.9	28.4
1.0	23.8	3	59	493	1.91	17.4
1.0	25.2	1	28	232	37.3	24.8
1.0	28.0	1	17	326	-7.22	15.9
1.1	20.2	1	9	100	6.25	23.9
1.1	20.4	1	16	100	76.2	35.7
1.1	20.7	1	14	100	56.2	32.8
1.1	21.0	1	13	100	46.2	31.2
1.1	21.3	1	18	101	95.3	38.0
1.1	21.6	2	37	203	99.8	27.2
1.1	21.8	1	23	100	146	44.4
1.1	22.1	1	8	100	-3.75	23.4
1.1	22.4	1	13	101	45.8	30.9
1.2	19.6	1	7	53.0	35.8	46.2
1.2	21.0	1	8	74.0	39.2	35.7
1.2	21.6	2	19	427	20.6	9.7
1.2	22.4	2	11	211	3.79	14.2
1.2	23.8	1	7	165	11.5	14.8
1.2	25.2	1	2	224	-13.8	12.0
1.2	28.0	1	5	300	-0.33	6.8

cross sections to emphasize that the beam was not monoenergetic.

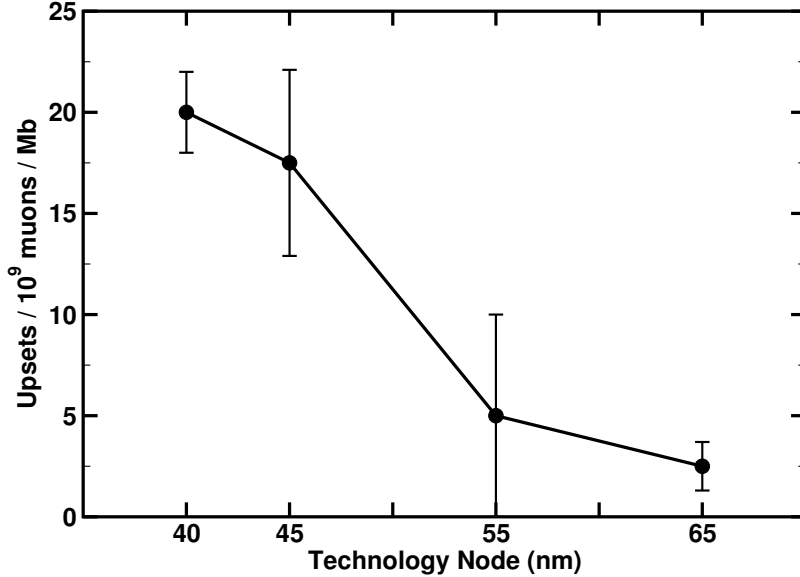


Figure 37: Experimental muon-induced single event upset probability for each device under test operated at nominal supply voltage. Momentum selection was 21.6 MeV/c.

These data show a clear increase in the SEU susceptibility and significance of energy deposition by muons for scaled technologies. To first order, the reduction of the device area results in a decrease in the number of particles passing through the cell and capable of producing an upset. This scaling would reduce the probability of a bit being in error in the beam. The increase in upset probability is therefore due to differences in the geometry of the charge collection, an increase in the fluence of energy deposition events exceeding the critical charge, or both.

Further, in these experiments, the incident muons have a distribution of kinetic energies and therefore a distribution of stopping powers. As the technology node decreases, the charge required to upset a single memory cell decreases. The effect of this trend is an increase in the fraction of the distribution that is able to induce an upset. For the 40 nm SRAM, a larger portion of the 21.6 MeV/c beam exceeds the stopping power threshold as compared with the 65 nm SRAM. While the probability

of upset is increasing for future devices, it cannot be ascertained from these data whether the trend is linearly or super-linearly increasing.

### Hardness Assurance Methods

#### Recommendations

Our results show, for some environments, that direct ionization from low-energy protons will be a significant factor affecting the overall error rate. If it is believed that a component is susceptible to upset from the direct ionization of a proton, characterizing the low-energy proton SEU cross section will be imperative. Therefore the implications for hardness assurance are considered and the following sequence of steps to qualify the component for space applications have been developed with the advisement of investigators at NASA Goddard.

**Step 1: Measure the upset cross section with long range, low-LET light ions.** In general, soft error rate prediction techniques derived from accelerated testing require that the stopping power of the incident particle is known as it traverses through the device. Low-energy proton testing is conducted using proton beams with energies at or below 2 MeV, such that the particles are at or near end-of-range. This is done to achieve mass stopping powers – LETs – large enough to cause single-event upset through direct ionization from the primary beam.

The SRIM-calculated mass stopping power of protons incident on silicon is compared to data from Helmut Paul's database [87] in Figure 38. It agrees well with the majority of data presented, though the large spread in experimental mass stopping powers below 1 MeV is apparent. It is generally true that experimental errors in

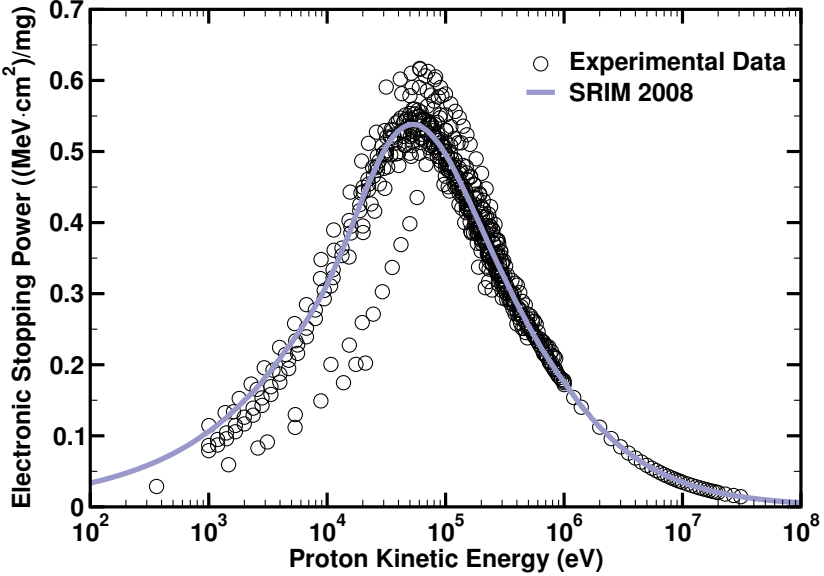


Figure 38: A comparison of experimental and calculated mass stopping power for hydrogen on silicon. The experimental data are taken from H. Paul’s database [87] and the calculated values are from SRIM-2008.04 [89]. Note that as proton energy decreases, the uncertainty in the experimental mass stopping power increases.

measuring stopping powers increases with decreasing energy [88]. For transmission measurements at low energy, thin foils are needed. This makes the presence of pin holes, surface impurities, and thickness variations detrimental to the measurement. Furthermore, the critical angle for channeling increases at low energy along with the importance of multiple scattering. These facts translate to uncertainty in stopping power formulations that rely on these data, which includes SRIM and codes based on ICRU Report 49 [36], such as Geant4.

Alternatively, ions having greater mass, must be accelerated to higher energy to achieve a similar stopping power. Thus they have increased range and reduced straggling, both issues that plague low-energy proton testing. The energy loss of higher-energy ions will be less sensitive to variations in materials as they are transported through the back-end-of-line or a flip-chip substrate.

## Step 2: Create an event model using low-LET data and technology

**information.** An event model, for Monte Carlo application or otherwise, should be derived from well-controlled and well-characterized radiation sources to be a valid predictor of failure rates in other environments. The predictable transport and energy loss of low-LET heavy ions, and even high-energy proton data should be used to build and calibrate the model. By applying a physics-based code to the model, one can predict stochastic processes. It is easier to construct the convolution of circuit response with the variable interaction of stopping rather than deconstruct data.

The model should be constructed with technology information to reproduce the various material layers and thicknesses that will affect low energy particles.

**Step 3: Validate the model by comparing it with measured low-energy proton response.** Most proton and heavy ion radiation test facilities use cyclotron accelerators. Cyclotrons can achieve high particle energies, but have minimum energy requirements below which resonant beams do not exist. Van de Graaff accelerators can produce low-energy beams with much tighter energy resolution than cyclotrons – a few keV wide versus several hundred keV wide – however, the upper energy limits of Van de Graaff accelerators make them less useful for many accelerated SEE testing applications.

Since cyclotrons are often used to accelerate protons and there is a lower limit to the energies they can produce, the proton beams must be degraded to achieve energies below approximately 7 MeV for in-air testing. Aluminum and Mylar are common degrader materials for protons, though higher- $Z$  materials like tantalum are also employed. Additional materials in the beam line, including the device-under-test, will also degrade the energy of the beam. However, degraded beam energy comes at the cost of increased energy-loss straggling. A charged particle passing through matter

loses most of its energy through random Coulomb collisions along the length of the track [36]. The total energy lost per particle along its track length is a stochastic quantity, so some particles will lose more energy and stop sooner than others, which is the basic concept behind energy-loss straggling. Degrading a beam removes its quasi-monoenergetic characteristic and thereby makes it difficult to tie proton energy to a specific single-event upset cross section since the cross section was produced by a spectrum of proton energies, as shown in Figure 26. It is more advantageous to tune the beam to the lowest possible energy before degrading in order to minimize straggle.

Based on low-energy proton testing experience gained so far, the following suggestions should be considered:

1. Measure and record materials in the beam line upstream from the device-under-test. Higher density and atomic number increase the importance of these materials for subsequent transport calculations.
2. Experimentally determine the mean beam energy and beam energy-width at the device-under-test location. This should be carried out for the primary, undegraded beam as well as for all degraded beams. Accurate and precise knowledge of the beam energy is critical for subsequent transport calculations since differences in beam energy on the order of 100 keV can result in single-event upset cross sections different by more than an order of magnitude.
3. In reference to item 1), it is important to complete transport calculations using accurate and properly ordered material stacks. It is inadvisable to collapse identical materials appearing in different upstream locations. As a proton

slows down, its stopping power increases non-linearly, so transporting a proton through an aluminum-air-aluminum stack is not the same as an aluminum-air stack with equivalent thicknesses.

4. Different levels of systematic error in the form of energy-loss straggling can be introduced depending on the type of device-under-test package. Topside wire bond schemes are preferable since the semiconductor back-end-of-line process is thin. Controlled collapse chip connection (C4), or flip-chip, packages are more common for commercial, highly-integrated parts. Flip-chip parts require irradiation through the backside of the die – *i.e.*, substrate – and should be uniformly thinned if possible to reduce straggling and lower the energy of possible beam tunes. Thicknesses less than 100  $\mu\text{m}$  are preferable, but are fraught with their own set of challenges. All parts must be delidded.
5. In reference to item 4), if the die is thinned, variations in proton stopping power can occur in different regions of the device if the die thickness is not uniform. The single-event upset cross section can be altered by variations of less than 10  $\mu\text{m}$  of material. Mitigating this problem requires two things: knowledge of die thickness and a way to monitor the physical location of single-event upsets. Die thickness can be determined non-destructively via x-ray cross sections or Rutherford backscattering spectrometry or, alternately, through destructive physical analysis following the experiment. Knowledge of physical upset location is achieved more easily for SRAM arrays, but can be quite challenging for more complex devices such as SDRAMs and FPGAs. This topic should be incorporated into the test design.

**Step 4: Use the calibrated model to predict the on-orbit error rate.**

The final step to determine the part's suitability in a space environment is to use the model to predict a soft error rate. A rate prediction that is derived from tests with unavoidable errors will inherit those errors. We advocate that the event model be derived from well-characterized radiation sources and only validated with more stochastic tests. This process of steps will add assurance to the determined reliability.

#### Low-Energy Proton Testing with a Cyclotron

As mentioned previously, testing for a low-energy proton sensitivity with a cyclotron can present difficulties interpreting the resulting data. However, since space-bound parts require a trip to a high-energy proton test facility, the chance to perform a screening test at low-energy is desirable. As the primary beam energy is too high to induce direct ionization upsets, thick degraders are used to slow the beam. Although low energies can be obtained, this practice introduces straggling and widens the incident energy distribution.

To investigate the viability of this approach and the shape of the energy distribution, radiation transport simulations of a 65 MeV proton beam were performed with MRED. In each simulation protons passed through an aluminum slab of variable thickness and the energy of each particle was recorded as it exited the slab. The histograms were smoothed and normalized to the particle fluence in Figure 39. The curves represent a probability density function of incident kinetic energies for the degrader selection.

The simulations demonstrate that degrader thicknesses of 5, 10, and 15 mm still produce reasonably shaped energy spectra for single event upset testing with peak

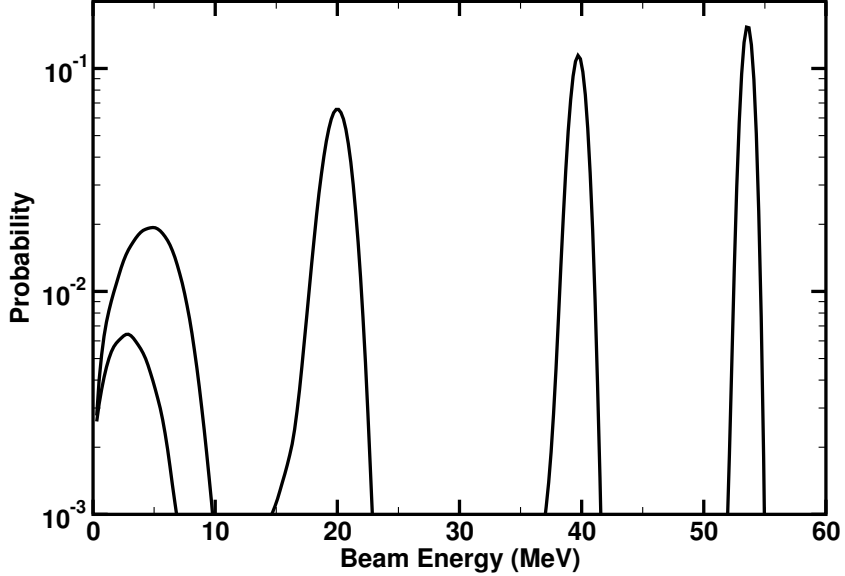


Figure 39: Simulated kinetic energy spectra of a 65 MeV proton beam after degraded by 5, 10, 15, 17, 17.25 mm aluminum slabs. According to PSTAR, the 65 MeV beam CSDA range is 17.3 mm.

energies at 53, 40, and 20 MeV. For thicker degraders producing lower-energies, the beam is spread wide relative to the changes in the SEU cross section measured in Figure 28. Since the SEU cross section increases by over three orders of magnitude, these beams would be a poor selection for quantitative measurements of the SEU cross section.

The simulated energy distributions were used to predict the observed SEU cross section as measured at a cyclotron facility with such a degrader setup. Cross section data were assumed for the illustration and are consistent with the values in Figure 28. A calculation of a measured cross section was then performed by multiplying the probability density function of the beam energy with the assumed upset cross section. The measured values in Figure 40 show that this test has merit. Naturally, the measurement will provide a good estimate at energies greater than 20 MeV where straggling is minimal and the actual cross section is unchanging. In the low-energy

region, although the measured cross section does not match the actual cross section, it indicates a proton direct ionization sensitivity. Even though the distribution of particle energies is wide in this region, the large increase in the actual monochromatic cross section makes the sensitivity evident at low energies.

Another approach is to use a modulator wheel to evaluate the direct ionization cross section for a range of incident energies. Carefully designed approaches similar to those described in [90, 91] can be used at cyclotron facilities taking advantage of a highly-degraded beam. The drawback of the use of a modulator wheel is that it restricts the test to an evaluation of the device response in a specific space environment. A rate prediction for low Earth or a solar flare environment can be directly measured from the test results, but because the cross section as a function of energy is not obtained, rate predictions for arbitrary environments are not possible.

If the part is shown to have the sensitivity, a monochromatic low-energy proton beam is recommended. This type of test requires a Van de Graaff or Pelletron machine capable of producing a suitable beam.

### Conclusions

Devices that exhibit a low-LET threshold are possibly sensitive to the direct ionization from singly-charged particles. Because of the abundance of these particles in both the space and terrestrial environments, additional tests to characterize a part's SEU cross section are justified. Through this work, we report on measurements of proton and muon-induced single event upsets characterized over incident energy. Accelerated test results show an SEU error count that varies over beam energy in a manner that is consistent with the energy loss curve.

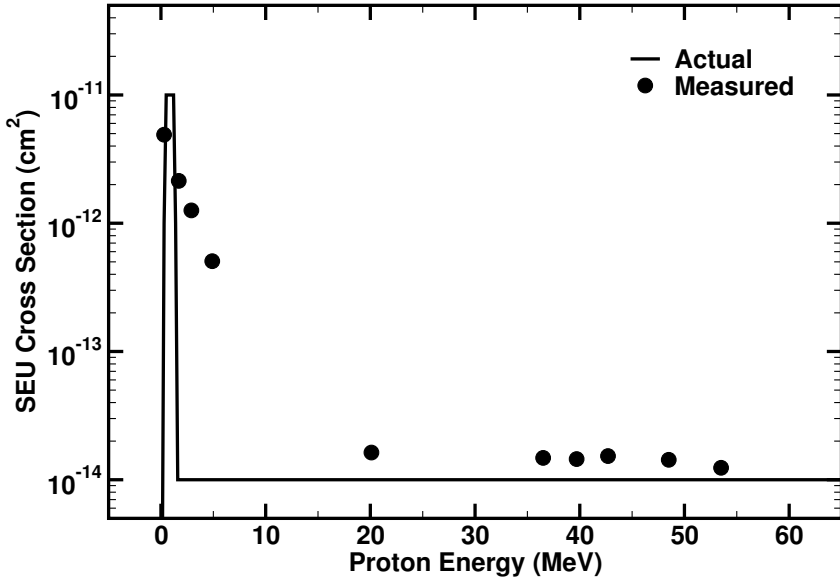


Figure 40: Prediction of measured proton SEU cross sections using various degraders in a 65 MeV beam.

Accelerated tests with muons present unique experimental challenges. First there are few high-energy facilities in the world that produce muon beams. Among these facilities, those that produce a surface muon beam are preferable to a cloud muon beam for observing a muon ionization effect. Surface muons are lower in energy since the pion decays within a production target and the construction of the following beam line reduces the possibility of contaminants reaching the device. Cloud and decay muons are produced by the decay of pions as they are transported down the beam line and can be either positive or negative polarity, but are typically higher energy. The range of the surface muon beam is limited because of the initial kinetic energy. Therefore, the amount of material encountered by the muons must be reduced. This may require that a device be de-lidded and de-passivated for test. In addition to any kinetic energy spread, straggling causes a distribution of kinetic energies to reach the active device area.

Fortunately, if the part is immune to proton direct ionization, there is high confidence that it is also immune to muon direct ionization. Proton testing, unlike that for muons, is easier and accelerators are more readily available. If the device is sensitive to proton direct ionization, though, it is possibly also susceptible to muon ionization.

The critical charge of present technologies is less than the muon ionization threshold. It is important to determine when (and if) muons will contribute a significant portion of the overall error rate. Testing a technology at reduced bias is a leading indicator for a sensitivity in scaled technologies.

Accelerated tests and soft error rate predictions are standard practices for microelectronics applications with high reliability requirements. The data presented here, however, suggest that the SER of future technologies also may be affected by protons and muons. Whereas neutrons only rarely interact with nuclei to produce ionizing particles, both protons and muons are able to generate charge through the electromagnetic force. Therefore, the low-energy muon and protons fluxes have the potential to be a significant component of the SER for sensitive devices.

Our results suggest muon-induced upsets do not affect the soft error rate for 65 nm and 45 nm SRAMs operated at nominal supply voltage, but they are likely to have a greater impact for circuits fabricated in smaller process technologies with lower critical charge values. Ultimately, SRAMs, flip-flops, and combinational logic may become sensitive to the low-energy muon spectrum. Future error rate predictions will require characterization of the device LET threshold, consideration of the full environment, and advanced radiation transport computations.

## CHAPTER V

### RATE PREDICTION ANALYSES

In this Chapter the implications of low-energy proton sensitivity are examined for various space environments. Although SEU cross sections at proton beam energies less than 1 MeV have been shown to be more than three orders of magnitude greater than at higher energies, the operating environment dictates whether this will be a reliability issue for the part or not. The raw space environments both near or far from Earth consist heavily of protons. Models to assess the relative importance of this upset mechanism versus the traditionally dominant particle interactions are applied to the measured SEU response.

Rate predictions for terrestrial muons are not presented here as the same model does not indicate significant error rates from muons for this technology generation. Instead, muon-induced error rates are examined in the following Chapter in a discussion of the implications for future devices.

#### Traditional Approaches

In the approach provided by Bendel [1], a one parameter fit to the proton upset cross sections over kinetic energy is derived. The method was intended to capture elastic recoil events at medium energies near the device upset threshold and inelastic particle reactions at high energies. Upon the assumption that the probability of an upset is independent of the proton incident energy for high-energy particle reactions, the cross section curve should follow  $\exp(-E/200 \text{ MeV})$  according to [92]. Bendel

also assumed that elastic scatters define the threshold region and the critical energy of a silicon recoil to cause an upset is 2.5 MeV (111 fC). This reaction requires an incident proton energy of 18.5 MeV by Equation 4. Applying arguments to justify the form of the function to fit experimental upset cross section, Bendel introduced a one-parameter model only requiring an apparent threshold  $A$ . Stapor later suggested a two-parameter function to fit both the energy threshold and the saturated cross section in [93]. The modified form of the original function, now known as the two-parameter Bendel equation is given by:

$$\sigma = \left(\frac{B}{A}\right)^{14} \left(1 - e^{(-0.18Y^{\frac{1}{2}})}\right)^4 \quad (16)$$

$$Y = \left(\frac{18}{A}\right)^{\frac{1}{2}} (E - A) \quad (17)$$

The simplicity of the approach has driven the data points sought in proton SEU testing. Acquisition of a few carefully selected proton energies and then folding the fit to the proton environment has enabled error rate predictions in proton environments. The fits have been used quite successfully for nearly thirty years. However, some device cross-section curves including those in the previous section are not well-described by this fit. In these cases, physical modeling is necessary.

### TCAD and SPICE Analysis

A three-dimensional Technology Computer Aided Design (TCAD) model of the 65 nm SRAM cell was used to investigate the SEU mechanisms from an incident charged particle. The dimensions and device parameters were approximated with values representative of the technology node. Ion tracks with stopping powers as low

as  $0.3 \text{ MeV}\cdot\text{cm}^2/\text{mg}$  were introduced into the device and simulated in the Synopsys Sentaurus Device TCAD solver. Figure 41 illustrates the TCAD structure with all materials other than silicon omitted and an ion strike to one of the NMOS transistors. The results of the transient simulations confirmed the inherent sensitivity of scaled technology nodes. This investigation of the physical processes of charge collection establishes that the electronic stopping of protons and muons, which have a peak LET near  $0.5 \text{ MeV}\cdot\text{cm}^2/\text{mg}$ , may induce upsets if the peak occurs near the sensitive device regions.

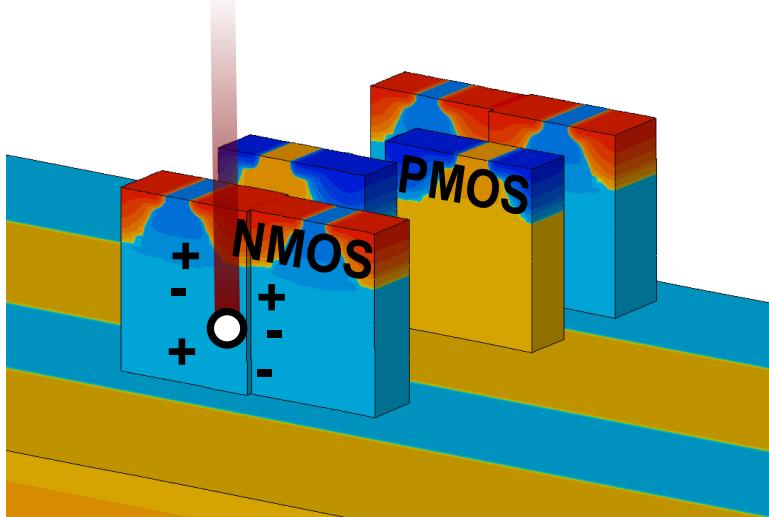


Figure 41: TCAD model of a 65 nm bulk CMOS SRAM. Oxides have been omitted for illustration. Sensitive drain areas are on the order of  $1 \times 10^{-10} \text{ cm}^2$ . Ionization core from ion strike to reverse-biased drain diffusion indicated.

For devices where detailed process information is unavailable the evaluation of a cell's sensitivity to ionizing radiation begins with an estimate of the circuit critical charge ( $Q_{\text{crit}}$ ) value. Few publications provide critical charge estimations for future or even recent deep-submicron technologies. For existing technologies, this value can be inferred from tests, device simulations, or circuit simulations. Device simulation can

be used to provide an estimate of  $Q_{\text{crit}}$ , but requires at the least basic knowledge of the process. If a chip has been fabricated, accelerated testing can be useful to determine the LET threshold, but the estimation of  $Q_{\text{crit}}$  still requires the assumption of a charge collection depth and may require at-angle testing and physical modeling to validate. Other works have attempted to provide models for pulse shaping for circuit simulations and critical charge analysis, but often lack any comparison to other forms of determination.

In our first evaluation of critical charge values, circuit simulations were performed. Predictive models [94, 95] for various nodes were downloaded from the Predictive Technology Model website [96]. A standard 6T SRAM cell based on the existing 65 nm design was constructed to establish transistor width to length ratios. For each smaller technology node, the appropriate MOSFET models were included in the netlist and the transistor dimensions were scaled by the square root of two. The voltage supply was also reduced using projections in the ITRS Roadmap [97]. A current source based on [98] was added to the netlist to perform transient charge injection. The parameters of the source were varied and the current integrated to obtain the injected charge. The largest quantity of charge that did not upset the circuit was recorded as the critical charge. These values are provided in Table 9.

The problems associated with a critical charge estimation from SPICE are the omission of parasitic capacitances in a predictive circuit netlist and the need for a current source with accurate pulse shaping. Several works have shown that this method may provide overestimates simply due to the current pulse shape [99, 100]. Therefore the SPICE values will be taken as an upper bound of the critical charge.

One could also base estimates of  $Q_{\text{crit}}$  on rough calculations of the gate capacitances as described in Chapter I Section . The calculations performed here are based on the trend in values projected by the ITRS Roadmap. The values are independent of the particular process and can be used to generalize the industry as a whole. In the roadmap, the total gate capacitance for a minimum length device is expected to remain relatively constant at  $1 \text{ fF}/\mu\text{m}$  over the next several generations. From the voltage and capacitance on an NMOS and PMOS pair, we derive an estimate of the  $Q_{\text{crit}}$  values for 65 through 16 nm technologies. These values are used as a lower bound for  $Q_{\text{crit}}$  in our subsequent analysis.

When comparing with the data in Figure 7 the predictions have good agreement to the extrapolated fit. In fact, Rodbell [32] quotes a critical charge for 65 nm SOI parts between 0.21 and 0.27 fC and an evaluation of the extrapolated fit yields 0.25 fC. It should be noted that further extrapolation under-predicts values provided in the table.

Table 9: Critical Charge Estimates

Technology (nm)	65	45	32	22	16
Vdd (V)	1.2	1.1	0.97	0.90	0.84
$Q_{\text{crit}}$ lower (fC)	0.32	0.21	0.13	0.088	0.056
$Q_{\text{crit}}$ upper (fC)	1.3	0.71	0.44	0.36	0.19

### Radiation Transport Modeling

MRED [101] (Monte Carlo Radiative Energy Deposition version 920) was used to investigate the energy deposition by ions and protons. MRED is based on Geant4 [102] (currently release 9.4.p01), which comprises reliable and well-calibrated computational physics models for the transport of radiation through matter. Geant4 is a

library of C++ routines assembled by an international collaboration for describing radiation interaction with matter. MRED includes a model for screened Coulomb scattering of ions [103], tetrahedral geometric objects [104], a cross-section biasing and track weighting technique for variance reduction, and a number of additional features relevant to semiconductor device applications. MRED is structured so that all physics relevant for radiation effects applications are available and selectable at run time.

The modeling methodology begins with the calibration of a weighted sensitive volume model for Monte Carlo simulation using a subset of the heavy ion data described in Table 5. The calibration is based on the device response to low-LET heavy ions and high-energy protons; the same calibrated model is used to predict the upset mechanisms and cross sections for protons at low energies where experimental data are difficult to obtain.

Figure 42 shows the measured single event upset cross sections for the ions used at TAMU and LBNL. Each ion has sufficient energy and range to deposit a known quantity of charge within the device region. We make the assumption that the single bit upset cross section corresponds to a physical device area that is sensitive to energy deposition events. Therefore only ions with stopping power between 0.6 and 2.8 MeV-cm<sup>2</sup>/mg were used for calibration, as the cross section must be physically justifiable and we avoid using data where multiple bit upsets are significant.

Sensitive volumes represent regions of sensitivity within the semiconductor materials. A weighted sensitive volume model [105] can be used to describe intracell variation in charge collection. The following equation relates energy deposited in the

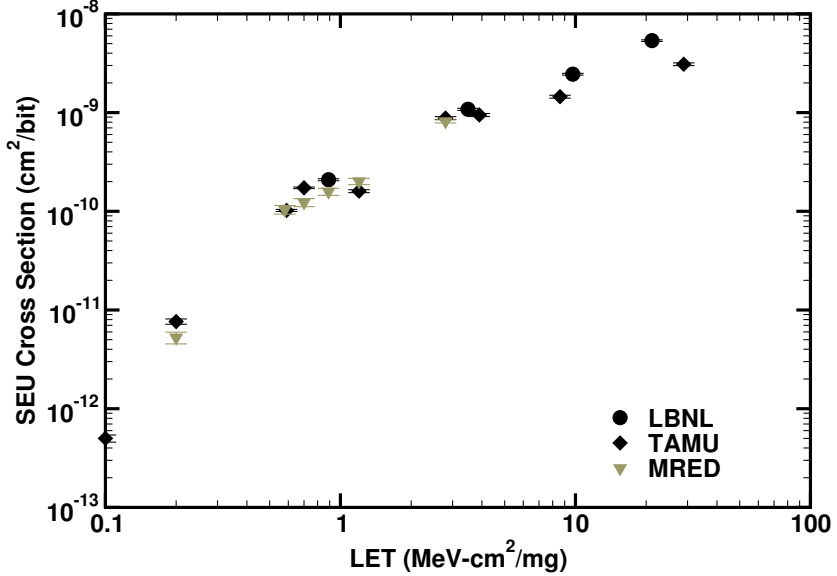


Figure 42: Heavy ion single event upset cross sections measured at LBNL and TAMU. Protons, for comparison, have a maximum LET of approximately 0.5 MeV-cm<sup>2</sup>/mg.

$N$  volumes used to describe a single device to the charge collected on the corresponding circuit node.

$$Q_{\text{coll}} = \frac{1 \text{ pC}}{22.5 \text{ MeV}} \times \sum_{i=1}^N (\alpha_i \times E_{\text{dep}_i}) \quad (18)$$

The model quantifies the charge collection at a node by an individual particle event as a linear combination of the energy deposited in each volume,  $E_{\text{dep}_i}$ , scaled by the respective coefficient  $\alpha_i$ , which is related to the collection efficiency. When the model contains nested volumes — that is, one or more volumes encapsulated within another — we make the distinction between the coefficient of an individual volume’s energy deposition  $\alpha_i$  and the collection efficiency of the region  $\hat{\alpha}_i$ . Our method for calibration to  $N$  normally-incident heavy ion cross sections proceeds as follows:

1. Choose the dimensions of a sensitive volume  $V_1$  placed in the active region and consistent with  $\sigma_1$ , device features, and isolation of the region. Assign  $\alpha_1 = 1$

to indicate 100% charge collection in this volume.

2. For each heavy ion cross section calibration value  $\sigma_i$ , where  $1 < i \leq N$  and  $\sigma_i > \sigma_{i-1}$ , ( or selected points along a Weibull curve ), create a sensitive volume  $V_i$  in the substrate with a surface area equal to  $\sigma_i$ . Assume the depth,  $d_i$ , of  $V_i$  is the same as the lateral dimension,  $\sqrt{\sigma_i}$ .
3. Assign each sensitive volume  $V_i$ , where  $i > 1$ , a charge collection efficiency  $\hat{\alpha}_i = \frac{Q_{\text{crit}}(\text{pC})}{LET_i \times d_i}$  where  $LET_i$  is in units of pC/ $\mu\text{m}$  and  $d_i$  in  $\mu\text{m}$ . This relationship essentially uses  $\hat{\alpha}_i$  to modify the quantity of charge generated in  $V_i$  required to exceed the circuit  $Q_{\text{crit}}$  (i.e., a strike further from the device requires a particle with a larger  $LET$  to upset the cell than a strike near the device).
4. Create a larger outer volume, with low efficiency, for high-energy proton secondary particles.
5. Assign  $\alpha_i = \hat{\alpha}_i - \sum_{j=i+1}^N \alpha_j$ , where  $i > 1$ , to obtain the coefficients necessary for Equation 18.
6. Simulate the experimental conditions and adjust parameters until good agreement is achieved with both heavy ion and high-energy proton datasets.

Following this method, we created the model illustrated in Figure 43. Volume  $V_1$  was assumed to encompass a transistor bounded in width and depth by shallow trench isolation and assigned  $\alpha_1 = 1$ . Volumes  $V_2$  and  $V_3$  were assigned individual coefficients 0.52 and 0.25 respectively. The outer volume was calibrated to  $\alpha_4 = 0.05$  with upset cross sections from protons with energy greater than 32.5 MeV, corresponding to nuclear reaction-driven upsets.

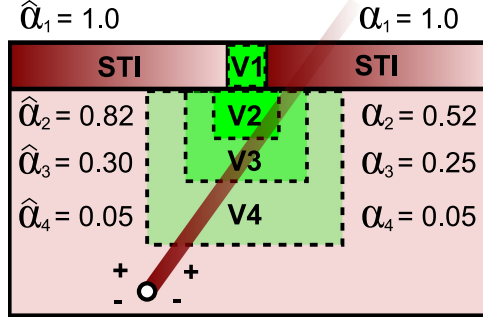


Figure 43: The weighted sensitive volume model used to model the response of a 65 nm CMOS SRAM cell. The surface area of each volume is correlated with normally-incident heavy ion cross sections.

Within the simulator, we create an array of device models in a silicon block with representative overlayer materials, and irradiate the target with normally incident particles. The underlying Geant4 code models the energy deposition in a device produced by direct ionization, recoils, and nuclear reactions. Each event is tallied in a charge collection histogram for the particular ion and energy simulated. The single event upset cross section versus collected charge is obtained by dividing the reverse integral of the histogram (i.e., the definite integral from  $Q_{\max}$  to  $Q$ ) by the fluence in the simulation. Using the experimental SEU cross sections for heavy ions and high-energy protons, we use a least squares fit to validate the assumed  $Q_{\text{crit}}$ . This is illustrated for a subset of the data in Figure 44. As we scan across critical charge values, we can extract the simulated SEU cross section for each of the species. As the critical charge, or vertical line, decreases, note that the simulated SEU cross section increases. As  $Q_{\text{crit}}$  increases, the SEU cross section decreases. This method of fitting estimates  $Q_{\text{crit}}$  to be 1.3 fC which is in good agreement with the SPICE analysis. The sensitive volume model and associated critical charge are used through the remainder of this chapter.

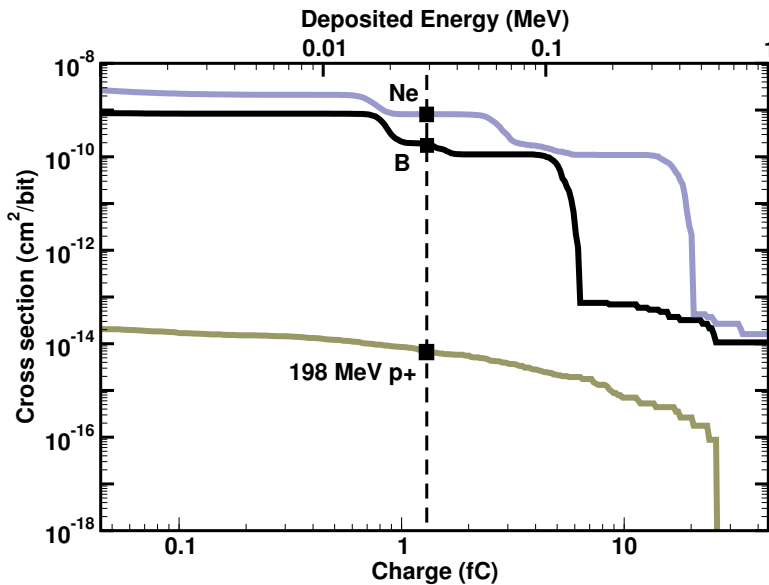


Figure 44: Simulated single event upset cross sections of a 65 nm SRAM cell as a function of collected charge. Vertical dashed line indicates a critical charge value providing the least error to experimental cross sections.

#### Single Event Upset Predictions

The strength of first-principles Monte Carlo simulation is that the calibrated device model can be used to study mechanisms and predict the device response in other radiation environments. The model may be used to predict the device response where experimental measurements may have systematic errors or cannot be made.

#### Proton Response

The low-energy proton response was computed using MRED with the calibrated model by extending the simulation of primary energies below 32.5 MeV. With only a few key calibration points to establish the charge collection volumes and critical charge we are able to capture the variety of mechanisms that result in the SEU cross sections in Figure 45. The high-energy proton cross sections show good agreement with the measured data and the simulation predicts the steep increase in cross section

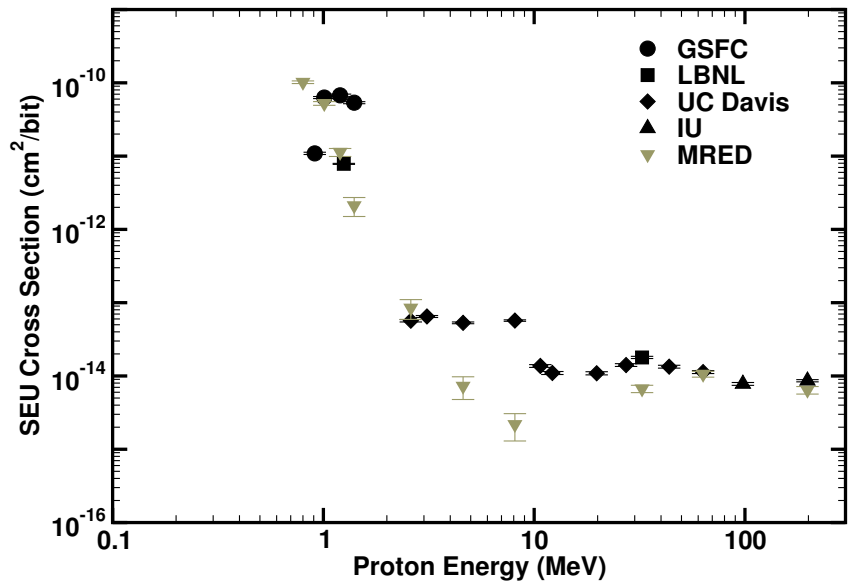


Figure 45: Simulated and experimental proton cross sections of a 65 nm SRAM cell. Model provides good agreement at high energy and captures the steep increase in cross section at low energy.

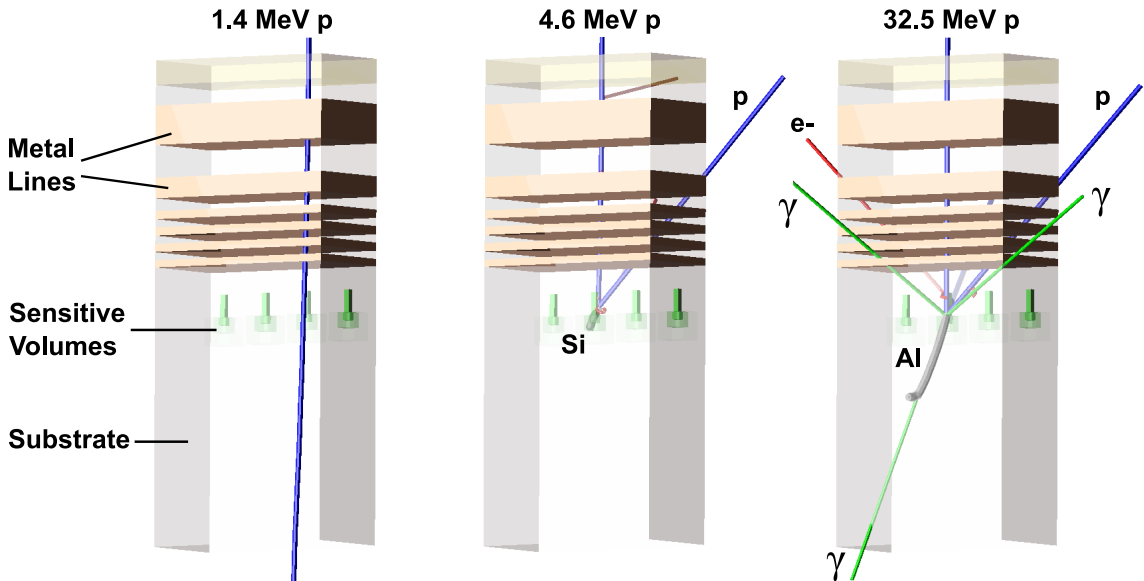


Figure 46: Events causing single event upsets in a 65 nm SRAM cell for 1.4, 4.6, and 32.5 MeV incident protons. The material dimensions have been reduced for illustration purposes.

below 2 MeV. While we can estimate the 1.4 MeV protons will be slowed and pass through the active silicon with a most probable energy of 430 keV, systematic errors in the energy of the proton as it passes through the device are not easily quantifiable. These errors were discussed in Chapter IV.

The nature of a physics-based simulation allows one to capture events resulting in an upset. Figure 46 illustrates examples of the different physical mechanisms leading to upset as predicted by MRED. The 1.4 MeV proton on the left passes through a representative back-end-of-line and exceeds the critical charge solely by electronic stopping. The event in the middle illustrates a short range silicon recoil that has been displaced by a 4.6 MeV proton and traverses the device. At higher energies, such as 32.5 MeV, spallation reactions produce secondary fragments that easily upset the device as they pass through.

### Rate Predictions

The model was used to predict the single event error rate in isotropic space environments. CREME96 flux versus energy spectra from Chapter III were transported through 100 mils of aluminum shielding. All species from Z=1 to 92 were simulated. The Monte Carlo computation included both electronic and nuclear energy loss and the contribution of each particle species was recorded. Energy filters required a minimum of 10 keV deposited for an event to register as valid in a device. The on-orbit error rate is predicted as the total errors from all species.

## International Space Station Orbit

Figure 47 shows the predicted error rate in the ISS orbit with 100 mils of aluminum shielding. Similar to the cross sections, we plot the error rate as a function of charge. This allows us to see the sensitivity to the critical charge parameter. In this proton-rich environment, we focus on the proton contribution. Two curves are shown for the protons. The curve labeled ‘H ( $dE/dx$ )’ represents the contribution from proton direct ionization only, and the second labeled ‘H (all processes)’ includes recoils and nuclear inelastic events. The vertical dashed line once again marks the critical charge. The model predicts that direct ionization from protons is a large contributor to the total error rate, which follows the ‘all processes’ curve. The predicted error rate for this environment is  $4.1 \times 10^{-8}$  upsets per bit per day.

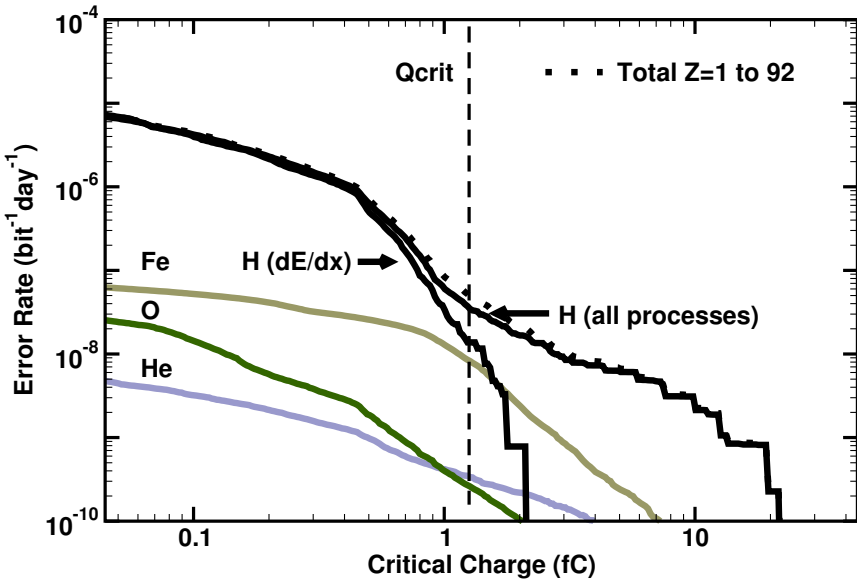


Figure 47: Simulated 65 nm SRAM error rate as a function of critical charge for CREME96 International Space Station orbit, AP8MIN, magnetic quiet, solar minimum, with 100 mils of aluminum shielding. Direct ionization from protons contribute heavily to the error rate.

### Geosynchronous Orbit (Worst day)

In a geosynchronous orbit with the worst day environment and 100 mils of aluminum shielding, we obtain the proton contribution shown in Figure 48. This environment is both proton and alpha particle rich and these particles dominate the error rate. The critical charge is at the point where proton direct ionization is significant and may continue to increase in the future. Certainly, the large flux of protons requires that we assess the impact of increasing event rates on higher levels of error mitigation. The predicted total error rate in this environment is  $3.0 \times 10^{-4}$  upsets per bit per day.

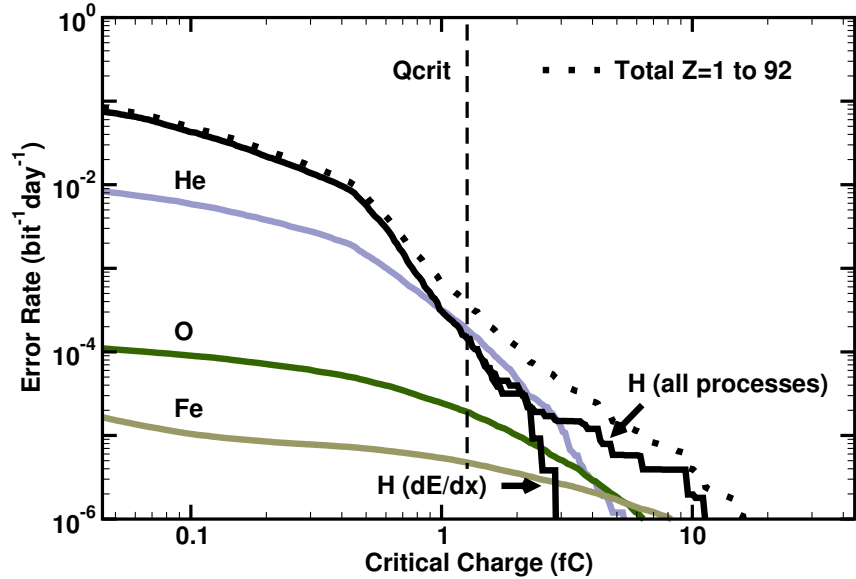


Figure 48: Simulated 65 nm SRAM error rate as a function of critical charge for CREME96 geosynchronous orbit, worst day, with 100 mils of aluminum shielding. Total Z=1 to 92 environment and major contributors to the error rate shown only. Direct ionization from protons and alphas dominate error rate.

### Geosynchronous Orbit (Solar min)

In a geosynchronous orbit, during solar minimum, we find that the proton flux is too low to be an issue in the total error rate and the contribution in Figure 49

is negligible. Instead, we can examine the contributions of ion species and see that the contributions of iron and oxygen continue to dominate the error rate. It is also possible that while the protons are not significant, the error rate will continue to climb for decreasing critical charge values. The GCR spectra contain large numbers of low-LET, light ions, one of which is oxygen. The predicted total error rate in this environment is  $1.2 \times 10^{-7}$  upsets per bit per day.

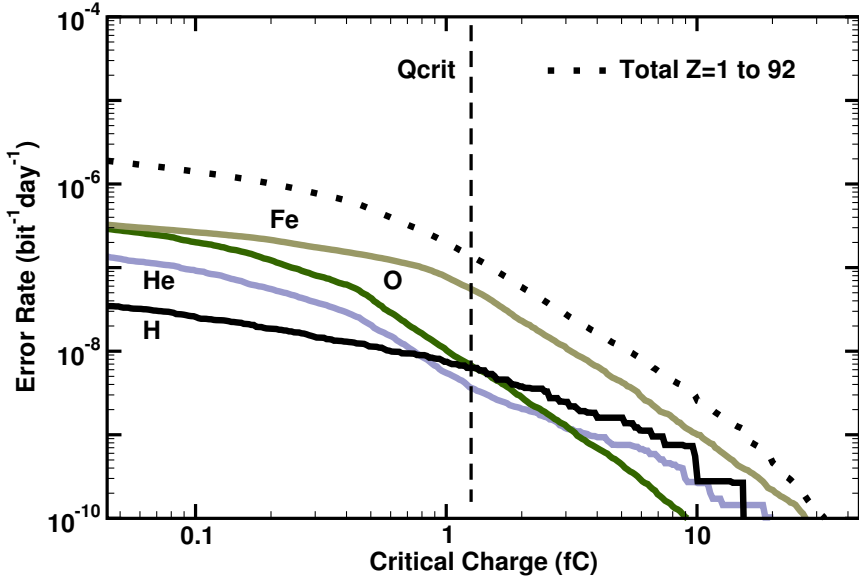


Figure 49: Simulated 65 nm SRAM error rate as a function of critical charge for CREME96 geosynchronous orbit, solar minimum, with 100 mils of aluminum shielding. Total  $Z=1$  to 92 environment and major contributors to the error rate shown only. Abundant low-LET ions dominate error rate.

### Effect of Shielding

Spacecraft shielding is an effective way to prevent particles from reaching internal components, but while the lowest energy particles are stopped, the shielding simultaneously slows higher energy particles. Figure 50 presents the effect of increased shielding on the error rate due to direct ionization from protons in the ISS orbit. The predictions show that the increase in equivalent aluminum shielding from 100 to 1000

mils reduces the rate by 5X, but does not eliminate upsets from low-energy protons. For other external environments, the level of mitigation gained with shielding will be dependent on the proton energy spectrum. Therefore, this upset mechanism may still have a significant contribution to the total error rate in a proton-rich environment, even behind heavy shielding.

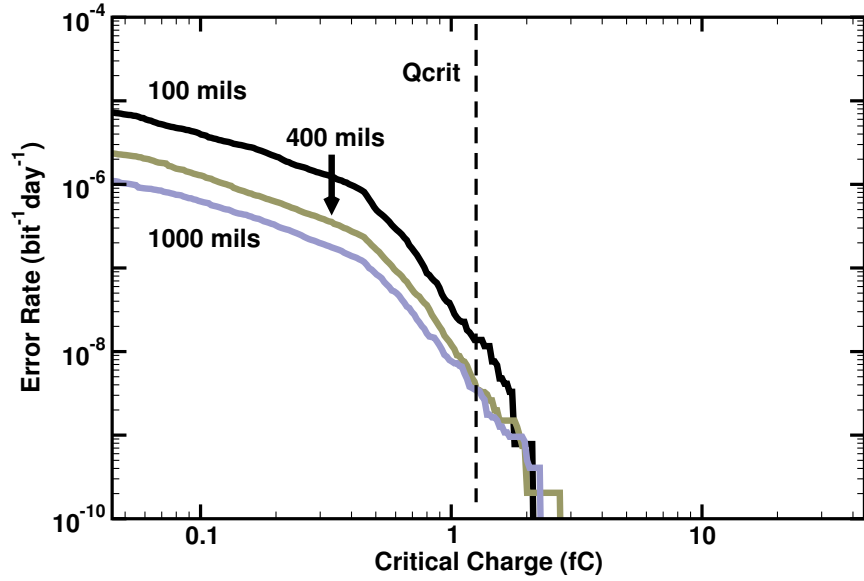


Figure 50: Simulated 65 nm SRAM error rate due to direct ionization from protons as a function of critical charge for CREME96 International Space Station orbit, AP8MIN, magnetic quiet, solar minimum, with 100, 400, and 1000 mils of aluminum shielding.

### Conclusions

Traditional models for evaluating the effects of protons on devices considered for space applications have only considered the nuclear interactions caused by this substantial portion of the environment. The distinction between direct ionization and nuclear-reaction induced effects has led to the development and application of different tools to evaluate each independently as if the environment could be separated into

these two constituents. With the onset of proton direct ionization upsets, physics-based Monte Carlo models work quite well to evaluate single events.

We have found that it is possible to describe the charge collection of a memory cell under heavy ion and proton irradiation by a weighted sensitive volume model. The specific model described for a 65 nm bulk CMOS process reproduced the SEU cross section over LET and also matched the proton cross sections over beam energy. When the model was evaluated under the proton-rich space environments, the error rates due to proton direct ionization alone were comparable to the nuclear-reaction component. Similar simulations for this technology in the terrestrial environment showed negligible effects from protons and muons compared to typical neutron-induced error rates.

## CHAPTER VI

### IMPLICATIONS FOR FUTURE DEVICES

According to the ITRS roadmap, conventional bulk planar CMOS will have difficulty continuing to meet the needs of the industry beyond gate lengths of 16 nm. It has been proposed that ultrathin body silicon-on-insulator or multiple gate technologies will be required to fill the need. The semiconductor industry is in the process of transitioning some applications to these new technologies. Even in light of the introduction of the new processes, conventional bulk planar CMOS may see several more generations of use.

Predictions for soft error rates at scaled technologies nodes beyond one generation out have no shortage of challenges. Even in bulk planar technologies, the initial spatial distributions of energy deposition, charge collection by contacts with nanometer dimensions, charge diffusion, and lack of calibration data make the application of a predictive model suspect. Further, the uncertainty in the industry's roadmap for technologies clouds our ability to look into the future.

In this section, the implications of various processes on the proton and muon error rates are examined. The differences in these analyses concern the charge collection due to geometrical changes. Other factors related to the specific technology are not considered and remain as future work when these technologies become available.

At deep-submicron technology nodes, it is likely that the sensitive volume for charge collection does not scale proportionally with the technology feature size. In the original works that developed the concept of a sensitive volume, the dominant

mechanism for charge collection was drift in the depletion region around the junction. For large devices, circa 1990, this volume may have scaled well with the junction size. However, diffusion of charge to devices with nanometer dimensions is an important consideration. Thus diffusion transport may establish the dimensions of the sensitive volume. It is probably the case that more complicated sensitive volume models would provide a better description of the amount of charge seen at the circuit node. However, in the absence of SEU cross section data and the complications of capturing multiple node charge collection and multiple cell upsets across technology nodes, we will forgo this model. Instead, the choice of a single sensitive volume will be used as an indicator for the trend in the soft error rates.

Larger diffusion areas would cause the generated charge curves to translate to high error rates. An increase in the sensitive volume depth will also increase charge collection for any given particle's linear energy transfer through an increase in path-length. In this case the energy deposition curves would translate to the right causing the soft error rates for an assumed  $Q_{\text{crit}}$  to increase.

The analysis is performed with MRED similarly to our previously presented model and simulations. However, in this work we have chosen to use a single sensitive volume model for each SRAM cell. The sensitive volume simply reports the amount of energy deposited within its boundaries for each particle event. The simple approximation of the model is that a cell upset occurs if the deposited charge is greater than or equal to the critical charge. In Section V we have discussed use of multiple weighted sensitive volume models.

Despite these pitfalls, for each technology node investigated, an array of volumes was constructed to represent a small group of SRAM cells. An individual sensitive

volume was sized according to the projected NMOS gate and drain geometry. As mentioned, the correlation of the volume lateral dimensions with the gate length is one possible, but not necessarily the correct, approximation of the effects of technology scaling on charge collection. For the simplicity of analysis, we will make the previous assumption for all technologies. To translate the model between technology nodes, the lateral dimensions of the model were scaled by  $\lambda = \sqrt{2}$ , as well as the spacing between volumes.

A multilayer planar stack structure was used to model the substrate and back-end-of-line materials for radiation transport. The layers were constructed of several layers of common microelectronics materials such as silicon,  $\text{SiO}_2$ , and copper. On top of the overlayers,  $200 \mu\text{m}$  of silicon was added to slow the lowest energy particles in the environment model to stopping. The exact details of the composition have very little effect on the results as the primary energy loss mechanism involved is electronic stopping. The material structure was reused for all technologies and did not change with scaling. The sensitive volume models were placed within the substrate layer.

The simulations produce histograms of energy deposition events weighted appropriately by the input flux spectrum. The simulation data are integrated and scaled to present plots of soft error rate versus the charge generated in the cell. The thick curves represent the range of  $Q_{\text{crit}}$  values that fall between our established upper and lower bounds for the technology node.

## Charge Collection Models

Additionally, Monte Carlo physics-based radiation transport simulations of the terrestrial muon spectrum were performed. The sensitive volumes were scaled laterally according to the representative technologies and the energy deposited by each particle was recorded.

In bulk planar CMOS, we note that there is little motivation for decreasing the well depth in the same way that scaling drives packing density. Therefore we assume a constant collection depth of  $0.5 \mu\text{m}$ . We will discuss the implications of our assumptions later.

FinFETs have been proposed as process technology to replace conventional bulk planar CMOS. The introduction of the fin structure allows for better control of the transistor channel but could also change the nature of the charge collection from a single event.

To establish a reasonable charge collection depth for bulk FinFETS, we have performed 3D drift-diffusion simulations with the Synopsys Sentaurus device simulator following a single event strike to a reverse-biased n+ junction in a silicon fin representative of a 22 nm device (Figure 51). The fin height (FH) was assumed to be 170 nm and the fin width (FW) 25 nm. The fin was placed on top of a  $2 \times 2 \times 2 \mu\text{m}$  substrate volume and a potential of 1 V was applied to the n+ diffusion and Nwells. The particle struck the fin at normal incidence with an LET of  $0.5 \text{ MeV}\cdot\text{cm}^2/\text{mg}$ . The track extended  $1.5 \mu\text{m}$  into the substrate from the top of the fin and had a characteristic radius of 2 nm.

The transient simulations solve for the current through the drain contact as shown in Figure 52. The integrated current is also plotted as an indication of the charge

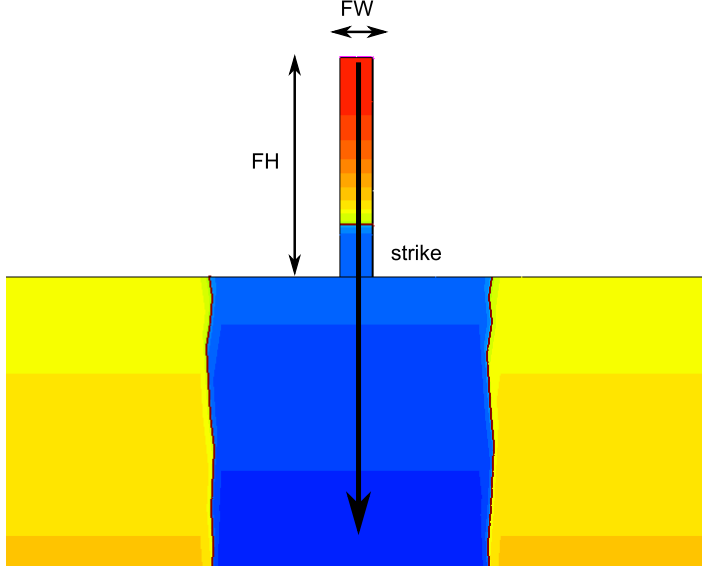


Figure 51: Three dimensional device model used to investigate the charge collection depth for a bulk FinFET drain. The fin width (FW) and fin height (FH) are characteristic of a 22 nm process. Red and yellow indicate the n-type regions including the drain and n-well. Blue regions indicate p-type doping.

collected at the contact. For this device, the charge arriving at the contact is approximately 1.3 fC. The collected charge and LET values indicate that the fin has a sensitive volume depth of 240 nm.

Ultrathin body silicon-on-insulator (UTSOI) is intended to improve the leakage current in fully-depleted technologies by reducing the thickness of the body to less than 10 nm. Devices with even thinner bodies have been proposed [106]. One challenge associated with making an operational device is reducing the lateral source-drain resistance with such a thin layer of silicon on top of a buried oxide layer and still providing enough material for silicidation. It has also been reported that the critical charge of an SOI SRAM decreases with decreased body thickness [107].

The sensitive volume thickness was assumed to be 10 nm, however raised source/drains in these technologies may even be as thick as 50 nm [108]. Under the LET pathlength assumptions, it is possible to deposit 0.05 fC with a particle of 0.5 MeV-cm<sup>2</sup>/mg.

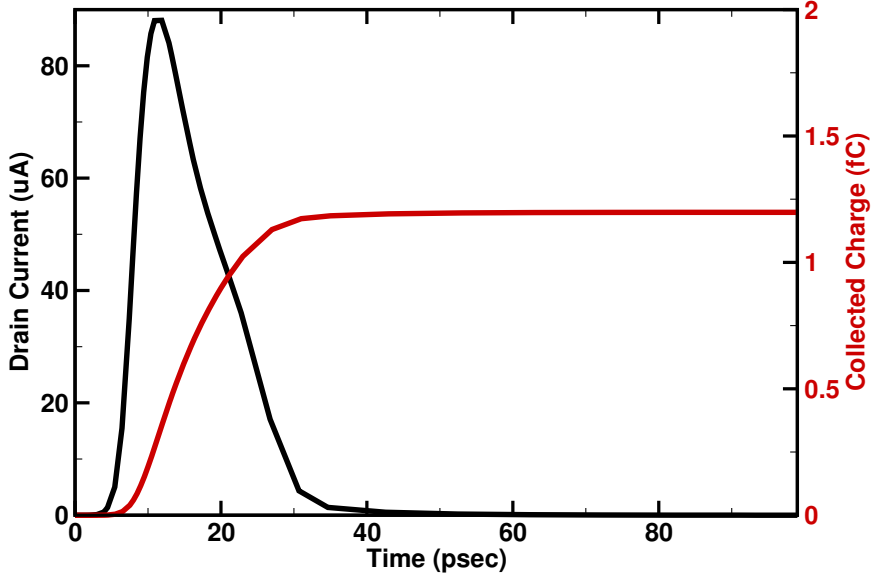


Figure 52: Device simulation results for single event strike into fin indicating drain current and collected charge.

The contacting scheme, which has been ignored here will also affect the sensitive volume. As discussed in [109], individual contacts to source/drain regions in multi-fin devices are unlikely. Additionally, bar contacts across the fins add parasitic capacitance. Instead methods of selective epitaxial growth are preferred. Unless these regions are completely consumed by silicidation, they could also contribute to the charge collected following a single event strike.

#### On-Orbit Single Event Upsets

The particle gun for the proton analysis used the Worst Day flux transported through 100 mils. This environment was chosen based on the response seen in Section V. To isolate the effect of direct ionization only, the nuclear models and recoils were turned off.

The curves in Figures 53, 54, and 55 show the results of the simulations representing the cells in the 32, 22, and 16 nm nodes. In each figure, error rates are presented

as a function of the critical charge. In the region of possible critical charge values indicated in Table 9, each curve is thicker.

The error rates predicted for the bulk devices are the highest due to the larger charge collection volumes. The bulk FinFET models show a reduced error rate which can be attributed to the smaller drain volume associated with the fins. The SOI device models, with the smallest volume for charge collection, show very low error rates, assuming that the critical charge values are similar to bulk devices.

For a given value of charge, the error rate curve for a smaller node shifts toward lower rates compared to a larger node. This is intuitive as the sensitive area presented by the cell decreases accordingly. In addition to the reduction in area, however, the critical charge will decrease. Given the two trends, the errors appear to maintain a fairly steady, but significant rate.

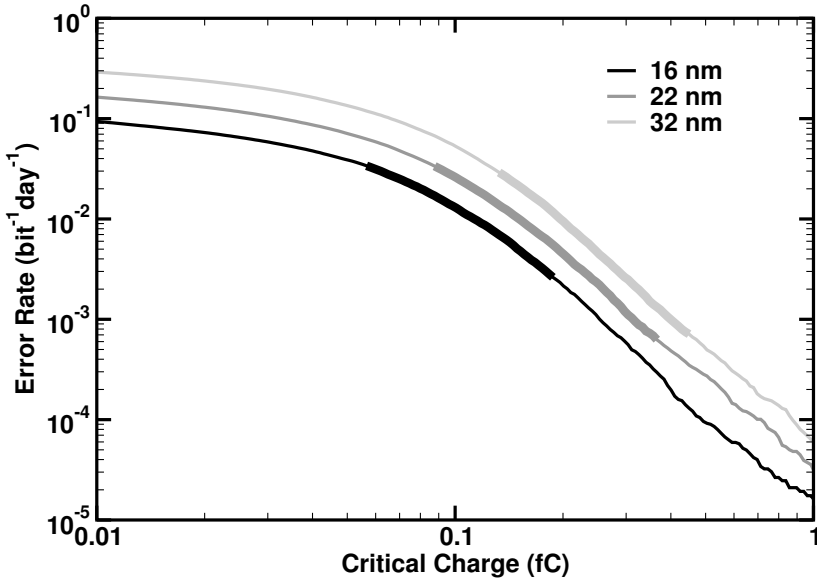


Figure 53: Estimated worst day proton  $dE/dx$  error rate versus critical charge curves for 32, 22, and 16 nm bulk CMOS representative sensitive volumes. Thick lines indicate the error rate for a technology node based on the range of critical charge values.

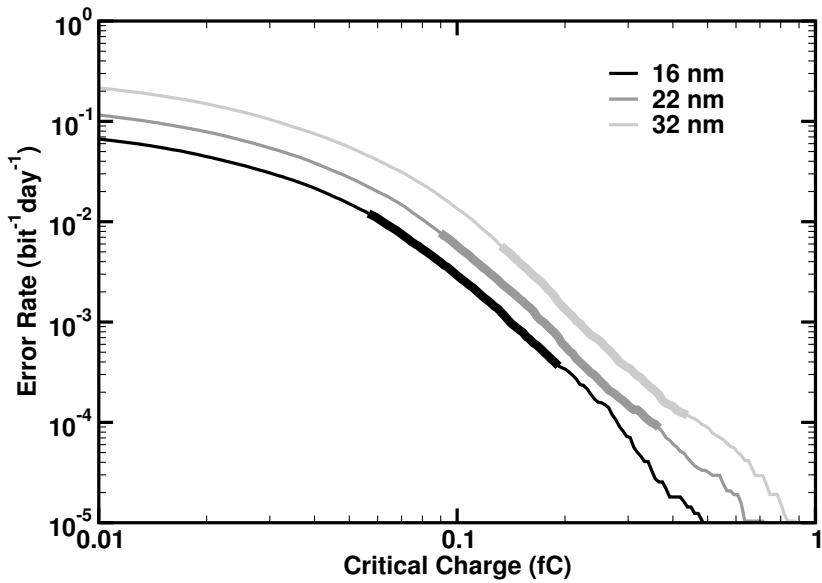


Figure 54: Estimated worst day proton dE/dx error rate versus critical charge curves for 32, 22, and 16 nm bulk FinFET representative sensitive volumes. Thick lines indicate the error rate for a technology node based on the range of critical charge values.

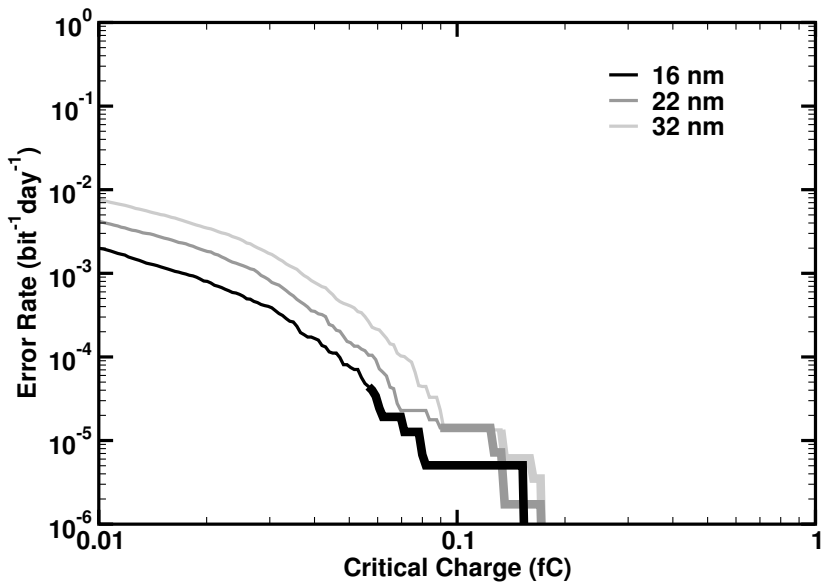


Figure 55: Estimated worst day proton dE/dx error rate versus critical charge curves for 32, 22, and 16 nm SOI representative sensitive volumes. Thick lines indicate the error rate for a technology node based on the range of critical charge values.

## Terrestrial Single Event Upsets

Our preliminary estimates indicate that the muon-induced error rates for the 65, 55, 45, and 40 nm technology nodes are insignificant. In all cases, the muon-induced FIT rate is much lower than those commonly quoted from neutron events which are typically a few hundred FIT/Mbit. Although it has been shown experimentally that these nodes are sensitive to direct ionization from muons, the flux of muons with sufficient stopping power to upset a cell is quite low.

We build on the assumptions laid out for the scaling of sensitive volumes with technology nodes to examine if and when such a muon susceptibility would become a reliability issue. For smaller and more sensitive technologies, the flux of muons that are capable of exceeding a cell's critical charge value is larger. Consequently, the muon-induced soft error rate will increase.

The particle gun used the proton,  $\mu^+$ , and  $\mu^-$  spectra obtained from EXPACS as described in Chapter III. The spectra include the flux of particles greater than 1 MeV.

The estimated muon sea level error rates are shown in Figures 56, 60, and 58 for 32, 22, and 16 nm representative sensitive volumes. Estimated proton error rates are shown in Figures 57, 59, and 61. Both sets of plots demonstrate similar characteristics. Each curve increases for lower values of critical charge in accordance with the expectation that a more sensitive device will have a higher error rate. Below the 32 nm technology node, the critical charge has decreased enough that this threshold now permits a significant rate of errors to occur. For a given process technology it is also apparent that the surface area of the volume is equally important as the upset threshold in determining the error rate.

The predicted error rates for muons and protons are significant as, for modern bulk CMOS memories, neutron-induced bit errors tend to be on the order of 100's of FIT/Mbit. According to Figure 56 the muon error rate may be as large as several thousand FIT/Mbit. In the bulk models the muon error rates tend to be higher than those predicted from sea level protons. The onset of proton-induced upsets is more gradual though and may exceed the muon upsets at higher critical charge values. In the bulk FinFET models, the contributions from protons and muons are similar in frequency possibly because of the reduced sensitive volume depth. The SOI models certainly had the lowest predicted values as the threshold for upset was below the estimated critical charge values. This is based on the assumption that these devices exhibit no bipolar amplification that could make them more susceptible than bulk processes.

Although the proton error rates are considerable, it should be noted that the simulations assume the device is exposed to the raw NYC cosmic ray environment. Protons, unlike muons, are easily mitigated by shielding by building materials below a few hundred MeV. In fact the range protons at the peak flux in Figure 18 prohibits most of the spectrum from reaching commerical applications. Based on these results, error rates due to ionization from other singly-charge particles such as antiprotons, kaons, and pions are expected to be neglible as well as the flux is lower. The results may still be of relevance for avionics applications where parts are less protected from the environment.

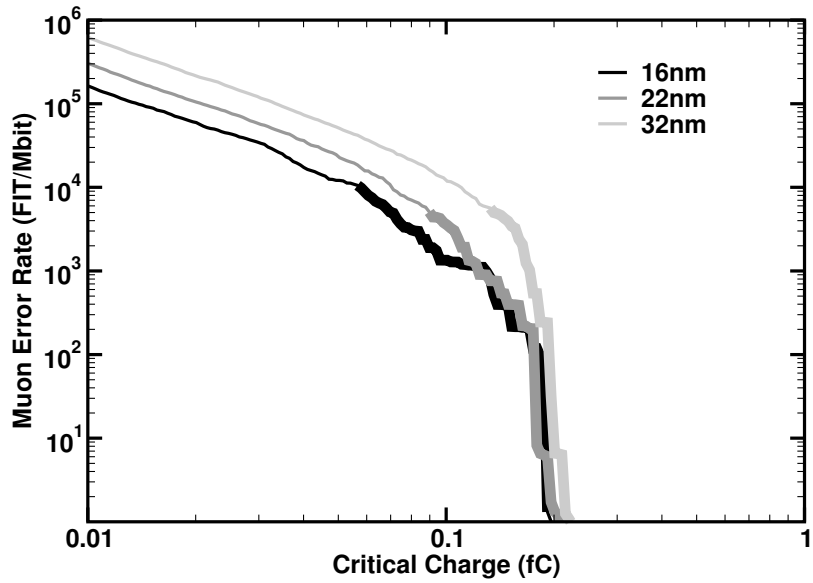


Figure 56: Estimated NYC muon-induced error rate versus critical charge curves for 32, 22, and 16 nm bulk CMOS representative sensitive volumes. Thick lines indicate the error rate for a technology node based on the range of critical charge values.

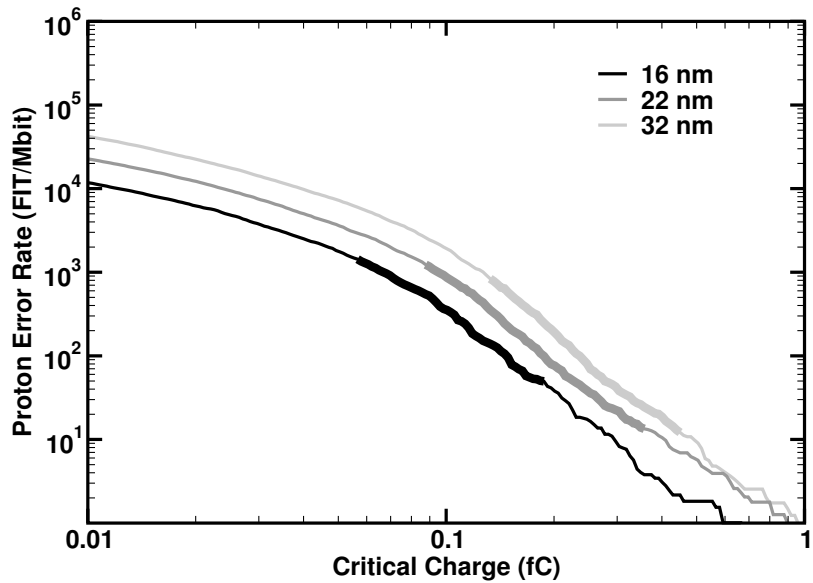


Figure 57: Estimated NYC proton-induced error rate versus critical charge curves for 32, 22, and 16 nm bulk CMOS representative sensitive volumes. Thick lines indicate the error rate for a technology node based on the range of critical charge values.

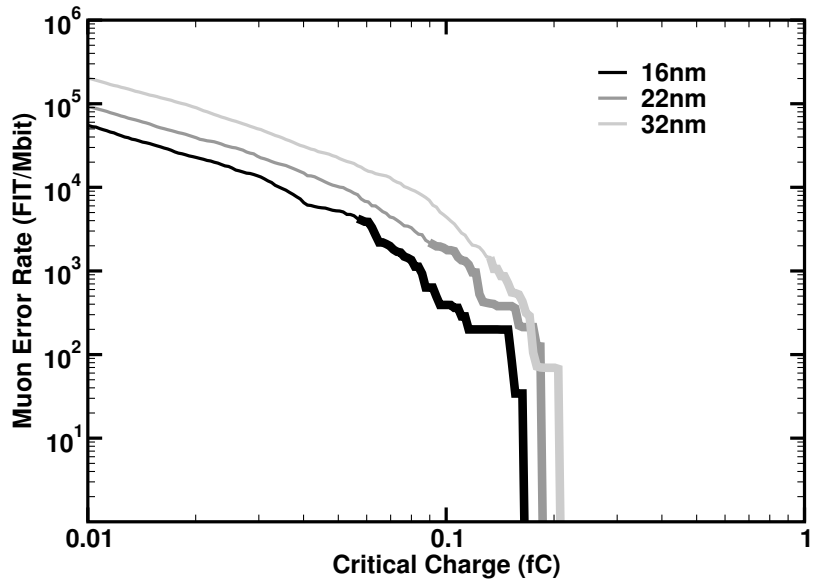


Figure 58: Estimated NYC muon-induced error rate versus critical charge curves for 32, 22, and 16 nm bulk FinFET representative sensitive volumes. Thick lines indicate the error rate for a technology node based on the range of critical charge values.

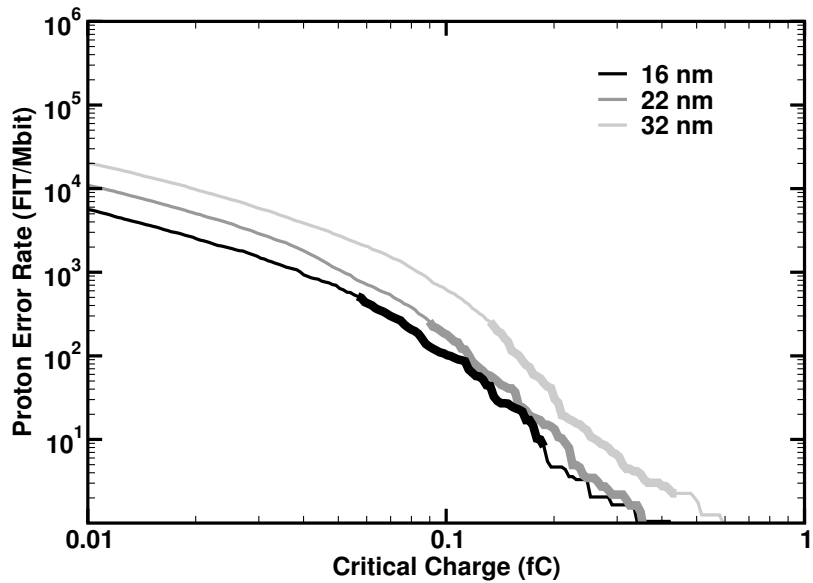


Figure 59: Estimated NYC proton-induced error rate versus critical charge curves for 32, 22, and 16 nm bulk FinFET representative sensitive volumes. Thick lines indicate the error rate for a technology node based on the range of critical charge values.

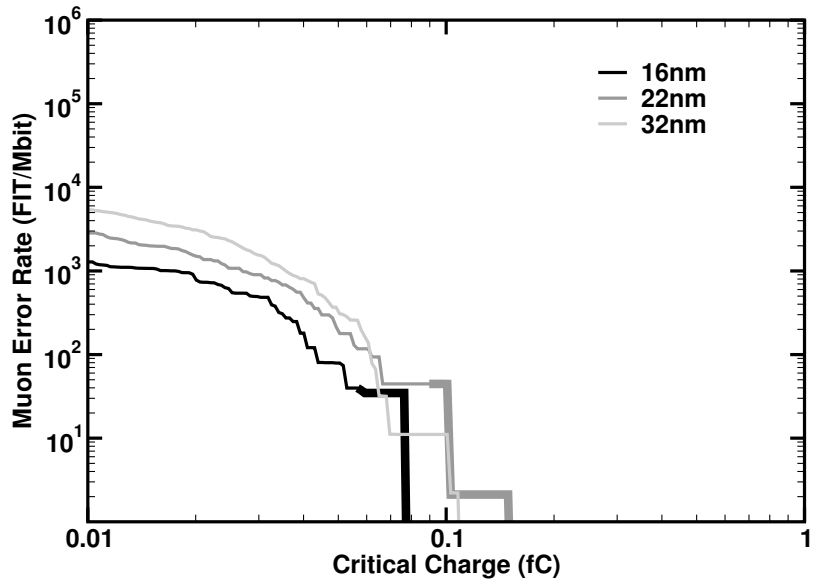


Figure 60: Estimated NYC muon-induced error rate versus critical charge curves for 32, 22, and 16 nm SOI representative sensitive volumes. Thick lines indicate the error rate for a technology node based on the range of critical charge values.

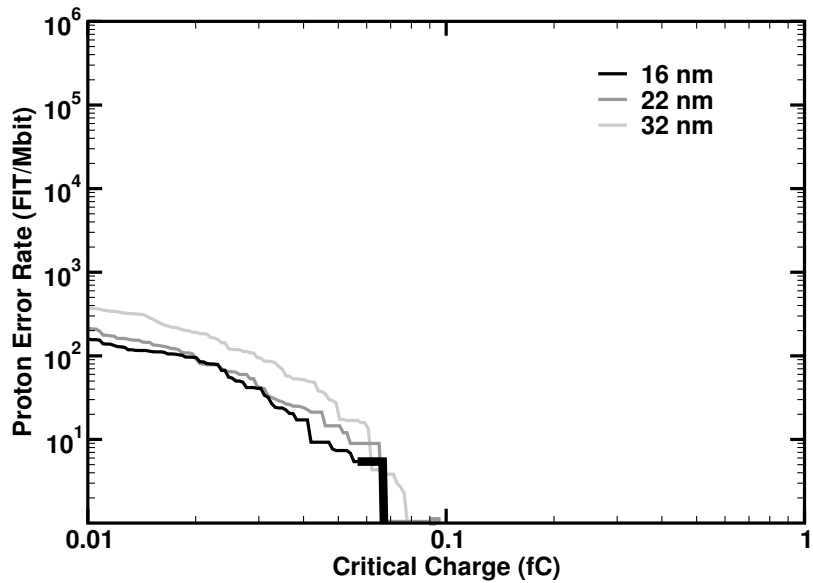


Figure 61: Estimated NYC proton-induced error rate versus critical charge curves for 32, 22, and 16 nm SOI representative sensitive volumes. Thick lines indicate the error rate for a technology node based on the range of critical charge values.

## Conclusions

In all cases, the error rates predicted by simulation in this chapter are not definitive, but depend on the previously stated assumptions. However, based on the assumptions regarding the space and terrestrial environments, the sensitive volume geometries, and the critical charge values established in the preceding sections, the upset rates in COTS microelectronic memories will experience a large portion of errors to the direct ionization from protons and muons. The simple charge collection models used in this analysis suggest that these errors will be present in sub-32 nm technologies and their contribution will be important even as geometries shrink.

The results indicate the potential for large variations in the error rate for 16 nm devices. The dramatic increase in the error rate for devices with a threshold below 0.2 fC suggest that even minor design differences may have a large impact on the reliability of the memory. Small changes in charge collection depth, cell area, and even critical charge variability may produce large changes in the error rate. Low-power memories may be especially susceptible to the effects of reduced critical charge.

These simulations only present the potential for direct ionization upsets from protons and muons. The models employed in the analyses are not rigorous. Factors affecting the charge collection in these nanometer volumes need to be investigated. Further, the details of charge transport through drift and diffusion as well as non-silicon materials and circuit response will shape the models for these technologies in ways not anticipated or captured here. As the technologies become available, the predictions made herein should be verified through accelerated testing with low-LET ions and low-energy protons.

## CHAPTER VII

### CONCLUSIONS

The expectation that microelectronics will operate reliably requires the anticipation and mitigation of radiation effects. It was proposed in this body of research that single event upsets in deep-submicron memories will be caused by direct ionization from singly-charged particles. It has been speculated since the industry was still in its infancy that these particles would exhibit an effect in sufficiently sensitive devices. However, devices which have been manufactured until the present time have not seen these effects.

In this work we have shown experimentally that the single event upset cross section for low-energy protons in 65 nm and smaller bulk CMOS technologies are sufficiently large to make ionization a substantial upset mechanism in a proton-rich space environment. Additionally, these technologies have been experimentally shown to upset due to muon ionization. The method and facilities used to collect the data not only show that a proton sensitivity exists in the technologies tested but also provide single event cross sections that can be used in modeling and rate prediction techniques. Experimental techniques need to be further developed to obtain similar datasets for muons.

The continued development of test methods in this area is necessary to confidently measure and predict the true effects. A number of uncertainties are introduced with these types of tests ranging from material effects to beam characteristics. Further, the low-energy environment is not completely characterized and highly-variable. A better

understanding of the environment and its extremes will help with reliable predictions.

Through a physics-based modeling approach that utilizes Monte Carlo methods, the single event effects were shown to have relevance to error rates in proton-rich space environments and in the terrestrial environment although at smaller technologies. Continued decreases in critical charges coupled with larger contributions from singly-charged particles in all natural environments will drive higher error rates in future technologies. This driver is only offset by accompanying changes in the charge collection volume, particularly the depth.

A general recommendation can be made based on the outcome of this work. Typically, in the course of qualifying a part for space or simply quantifying its error rate in a terrestrial environment, the part will be taken to a proton facility for testing with energies from tens to hundreds of MeV. This is necessary according to good practice for space and can also be used as a substitute for monochromatic neutrons for commercial applications. The data and simulations in this work support the recommendation that the cyclotron beam additionally be degraded and used for low-energy proton testing. While not providing usable cross sections, this experiment can be a gating condition for further tests. Datasets which demonstrate a clear roll off in the proton SEU cross section at energies well above a few MeV strongly suggest the part is immune to proton direct ionization. If no roll off in the SEU cross section exists and even increases near stopping or if the result of the degraded beam test is inconclusive as to demonstrate direct ionization, further testing with an electrostatic accelerator is recommended.

Low-energy tests with an electrostatic accelerator are much better controlled and provide data which may be used to calibrate an SEU model for rate predictions. In

the case of terrestrial applications, a demonstration of a low-energy proton sensitivity is a necessary, but not sufficient indication of a low-energy muon sensitivity. In this case, characterization of the part at a surface muon facility may be pursued.

## APPENDIX A: EXPACS GENERATED FLUX SPECTRA

Table 10: Positive Muon Flux at Sea Level in NYC

Energy (MeV)	Flux ( $\mu^+/\text{cm}^2\text{-s-MeV}$ )
1.1295	5.63403E-08
1.4219	7.09374E-08
1.7901	8.92315E-08
2.2536	1.121E-07
2.8371	1.40606E-07
3.5717	1.76017E-07
4.4965	2.19808E-07
5.6607	2.73664E-07
7.1264	3.39454E-07
8.9716	4.19147E-07
11.295	5.14712E-07
14.219	6.27821E-07
17.901	7.59761E-07
22.536	9.10846E-07
28.371	1.08018E-06
35.717	1.26524E-06
44.965	1.46164E-06
56.607	1.66317E-06
71.264	1.86219E-06
89.716	2.05026E-06
112.95	2.21909E-06
142.19	2.36131E-06
179.01	2.47127E-06
225.36	2.54501E-06
283.71	2.58021E-06
357.17	2.5757E-06
449.65	2.53103E-06
566.07	2.44624E-06
712.64	2.32193E-06
897.16	2.1597E-06
1129.5	1.96276E-06
1421.9	1.73689E-06

Energy (MeV)	Flux ( $\mu^+/\text{cm}^2\text{-s-MeV}$ )
1790.1	1.49055E-06
2253.6	1.2352E-06
2837.1	9.84129E-07
3571.7	7.50784E-07
4496.5	5.46536E-07
5660.7	3.78675E-07
7126.4	2.49382E-07
8971.6	1.56109E-07
11295	9.3006E-08
14219	5.2888E-08
17901	2.87983E-08
22536	1.50818E-08
28371	7.63068E-09
35717	3.74687E-09
44965	1.79342E-09
56607	8.40168E-10
71264	3.86601E-10
89716	1.7529E-10

Table 11: Negative Muon Flux at Sea Level in NYC

Energy (MeV)	Flux ( $\mu^-/\text{cm}^2\text{-s-MeV}$ )
1.1295	7.36689E-08
1.4219	9.03373E-08
1.7901	1.10687E-07
2.2536	1.35469E-07
2.8371	1.65572E-07
3.5717	2.02019E-07
4.4965	2.45963E-07
5.6607	2.98672E-07
7.1264	3.61495E-07
8.9716	4.35783E-07
11.295	5.22798E-07
14.219	6.23472E-07
17.901	7.38364E-07
22.536	8.67212E-07
28.371	1.0088E-06
35.717	1.16073E-06
44.965	1.31924E-06
56.607	1.47939E-06
71.264	1.63531E-06
89.716	1.78074E-06
112.95	1.90966E-06
142.19	2.01677E-06
179.01	2.09806E-06
225.36	2.15068E-06
283.71	2.17288E-06
357.17	2.16366E-06
449.65	2.12247E-06
566.07	2.0491E-06
712.64	1.94375E-06
897.16	1.80748E-06
1129.5	1.64275E-06
1421.9	1.45415E-06
1790.1	1.24854E-06
2253.6	1.03537E-06
2837.1	8.25624E-07

Energy (MeV)	Flux ( $\mu^-/\text{cm}^2\text{-s-MeV}$ )
3571.7	6.30485E-07
4496.5	4.59466E-07
5660.7	3.18719E-07
7126.4	2.1015E-07
8971.6	1.31709E-07
11295	7.85605E-08
14219	4.47228E-08
17901	2.4377E-08
22536	1.2778E-08
28371	6.47028E-09
35717	3.1793E-09
44965	1.52266E-09
56607	7.13681E-10
71264	3.28536E-10
89716	1.49013E-10

Table 12: Proton Flux at Sea Level in NYC

Energy (MeV)	Flux (p/cm <sup>2</sup> -s-MeV)
1.1295	3.17659E-07
1.4219	3.38165E-07
1.7901	3.59994E-07
2.2536	3.8322E-07
2.8371	4.07927E-07
3.5717	4.34198E-07
4.4965	4.62112E-07
5.6607	4.91738E-07
7.1264	5.23124E-07
8.9716	5.56279E-07
11.295	5.91145E-07
14.219	6.27514E-07
17.901	6.65009E-07
22.536	7.02866E-07
28.371	7.39776E-07
35.717	7.73567E-07
44.965	8.00838E-07
56.607	8.16655E-07
71.264	8.14643E-07
89.716	7.88023E-07
112.95	7.32098E-07
142.19	6.47683E-07
179.01	5.42914E-07
225.36	4.31394E-07
283.71	3.26757E-07
357.17	2.38009E-07
449.65	1.68301E-07
566.07	1.16497E-07
712.64	7.94394E-08
897.16	5.36014E-08
1129.5	3.58829E-08
1421.9	2.38679E-08
1790.1	1.57693E-08
2253.6	1.03326E-08
2837.1	6.68703E-09
3571.7	4.24076E-09

Energy (MeV)	Flux (p/cm <sup>2</sup> -s-MeV)
4496.5	2.60062E-09
5660.7	1.52013E-09
7126.4	8.37467E-10
8971.6	4.0304E-10
11295	1.70388E-10
14219	7.80528E-11
17901	4.15067E-11
22536	2.32366E-11
28371	1.2736E-11
35717	6.73056E-12
44965	3.53701E-12
56607	1.90924E-12
71264	1.04889E-12
89716	5.76922E-13

Table 13: Neutron Flux at Sea Level in NYC

Energy (MeV)	Flux (n/cm <sup>2</sup> -s-MeV)
1.1295E-08	20938.62298
1.4219E-08	23445.19265
1.7901E-08	25480.44436
2.2536E-08	26671.2223
2.8371E-08	26630.28457
3.5717E-08	25060.14341
4.4965E-08	21898.00723
5.6607E-08	17448.83997
7.1264E-08	12410.42972
8.9716E-08	7701.074385
1.1295E-07	4099.814784
1.4219E-07	1903.955814
1.7901E-07	866.1702727
2.2536E-07	485.891103
2.8371E-07	357.4277736
3.5717E-07	293.2748751
4.4965E-07	243.4056802
5.6607E-07	200.6531615
7.1264E-07	164.3170188
8.9716E-07	133.882014
1.1295E-06	108.6661063
1.4219E-06	87.9537619
1.7901E-06	71.0321301
2.2536E-06	57.27335212
2.8371E-06	46.12192279
3.5717E-06	37.10540487
4.4965E-06	29.828713
5.6607E-06	23.96451464
7.1264E-06	19.24333198
8.9716E-06	15.44580784
0.000011295	12.39285033
0.000014219	9.941030905
0.000017901	7.971716716
0.000022536	6.391150975
0.000028371	5.122927611
0.000035717	4.105590867

Energy (MeV)	Flux (n/cm <sup>2</sup> -s-MeV)
0.000044965	3.289760153
0.000056607	2.635703671
0.000071264	2.111416476
0.000089716	1.691261509
0.00011295	1.354569705
0.00014219	1.084939623
0.00017901	0.868919224
0.00022536	0.695937385
0.00028371	0.557426325
0.00035717	0.446525106
0.00044965	0.357741966
0.00056607	0.286673378
0.00071264	0.229783294
0.00089716	0.184247101
0.0011295	0.147793643
0.0014219	0.118624832
0.0017901	0.095269688
0.0022536	0.076574542
0.0028371	0.061606373
0.0035717	0.049619494
0.0044965	0.040018137
0.0056607	0.032325441
0.0071264	0.026159126
0.0089716	0.021214311
0.011295	0.017246212
0.014219	0.014061326
0.017901	0.011501503
0.022536	0.009442885
0.028371	0.007785379
0.035717	0.006449043
0.044965	0.005370032
0.056607	0.004497237
0.071264	0.003789645
0.089716	0.003214489
0.11295	0.002745356
0.14219	0.002361268
0.17901	0.00204488
0.22536	0.001782446
0.28371	0.00156262

Energy (MeV)	Flux (n/cm <sup>2</sup> -s-MeV)
0.35717	0.001376103
0.44965	0.001215234
0.56607	0.001073682
0.71264	0.000946255
0.89716	0.000828853
1.1295	0.000718432
1.4219	0.000613168
1.7901	0.000512349
2.2536	0.000416616
2.8371	0.000327695
3.5717	0.000248085
4.4965	0.000180413
5.6607	0.000126586
7.1264	8.70099E-05
8.9716	6.02577E-05
11.295	4.34389E-05
14.219	3.32154E-05
17.901	2.68234E-05
22.536	2.25668E-05
28.371	1.95918E-05
35.717	1.74327E-05
44.965	1.57239E-05
56.607	1.41428E-05
71.264	1.24575E-05
89.716	1.05756E-05
112.95	8.54824E-06
142.19	6.52615E-06
179.01	4.68323E-06
225.36	3.15366E-06
283.71	1.99459E-06
357.17	1.18923E-06
449.65	6.73124E-07
566.07	3.65665E-07
712.64	1.9353E-07
897.16	1.01627E-07
1129.5	5.39115E-08
1421.9	2.92835E-08
1790.1	1.63568E-08
2253.6	9.36637E-09

Energy (MeV)	Flux (n/cm <sup>2</sup> -s-MeV)
2837.1	5.45818E-09
3571.7	3.21329E-09
4496.5	1.90104E-09
5660.7	1.12679E-09
7126.4	6.68096E-10
8971.6	3.96031E-10
11295	2.34643E-10
14219	1.38993E-10
17901	8.22962E-11
22536	4.8716E-11
28371	2.88322E-11
35717	1.70611E-11
44965	1.00943E-11
56607	5.97189E-12
71264	3.53262E-12
89716	2.08953E-12

## REFERENCES

- [1] W. L. Bendel and E. L. Petersen, "Proton upsets in orbit," *IEEE Trans. Nucl. Sci.*, vol. 30, no. 6, pp. 4481–4485, Dec. 1983.
- [2] K. A. LaBel, M. M. Gates, A. K. Moran, P. W. Marshall, J. Barth, E. G. Stassinopoulos, C. M. Seidleck, and C. J. Dale, "Commercial microelectronics technologies for applications in the satellite radiation environment," in *Proc. IEEE Aerospace Applications Conf.*, vol. 1, Feb. 1996, pp. 375–390.
- [3] K. A. LaBel, R. L. Ladbury, L. M. Cohn, and T. R. Oldham, "Radiation test challenges for scaled commercial memories," *IEEE Trans. Nucl. Sci.*, vol. 55, no. 4, pp. 2174–2180, Aug. 2008.
- [4] EIA/JEDEC, *JESD57: Test Procedures for the Measurement of Single-Event Effects in Semiconductor Devices from Heavy Ion Irradiation*. 2500 Wilson Blvd., Arlington, VA 22201: Electronic Industries Association, 1996.
- [5] JEDEC, *JESD89A: Measurement and Reporting of Alpha Particle and Terrestrial Cosmic Ray-Induced Soft Errors in Semiconductor Devices*. 2500 Wilson Blvd., Arlington, VA 22201: JEDEC Solid State Technology Association, 2006.
- [6] Semiconductor Industry Association (SIA), "International roadmap for semiconductors 2009 edition," 2009. [Online]. Available: <http://www.itrs.net>
- [7] J. T. Wallmark and S. M. Marcus, "Minimum size and maximum packing density of nonredundant semiconductor devices," in *Proc. of the IRE*, Mar. 1962, pp. 286–298.
- [8] C. Svensson, "Forty years of feature-size predictions (1962-2002)," in *Dig. IEEE Int. Solid-State Circuits Conf.*, 2003, pp. 35–36.
- [9] D. Binder, E. C. Smith, and A. B. Holman, "Satellite anomalies from galactic cosmic rays," *IEEE Trans. Nucl. Sci.*, vol. 22, no. 6, pp. 2675–2680, Dec. 1975.
- [10] T. C. May and M. H. Woods, "Alpha-particle-induced soft errors in dynamic memories," *IEEE Trans. Electron Devices*, vol. 26, no. 1, pp. 2–9, 1979.
- [11] J. F. Ziegler and W. A. Lanford, "Effect of cosmic rays on computer memories," *Sci.*, vol. 206, no. 4420, pp. 776–788, 1979.
- [12] J. F. Ziegler, "The effect of concrete shielding on cosmic ray induced soft fails in electronic systems," *IEEE Trans. Electron Devices*, vol. 28, no. 5, pp. 560–565, May 1981.
- [13] R. Silberberg, C. H. Tsao, and J. R. Letaw, "Neutron generated single-event upsets in the atmosphere," *IEEE Trans. Nucl. Sci.*, vol. 31, pp. 1183–1185, Dec. 1984.

- [14] J. F. Dicello, C. W. McCabe, J. D. Doss, and M. Paciotti, "The relative efficiency of soft-error induction in 4K static RAMs by muons and pions," *IEEE Trans. Nucl. Sci.*, vol. 30, no. 6, pp. 4613–4615, Dec. 1983.
- [15] J. F. Dicello, M. E. Schillaci, C. W. McCabe, J. D. Doss, M. Paciotti, and P. Berardo, "Meson interactions in NMOS and CMOS static RAMs," *IEEE Trans. Nucl. Sci.*, vol. 32, no. 6, pp. 4201–4205, Dec. 1985.
- [16] J. F. Dicello, "Microelectronics and microdosimetry," *Nucl. Instrum. Methods Physics Res. B*, vol. 24-25, no. Part 2, pp. 1044–1049, 1987.
- [17] J. F. Dicello, M. Paciotti, and M. E. Schillaci, "An estimate of error rates in integrated circuits at aircraft altitudes and at sea level," *Nucl. Instrum. Methods Physics Res. B*, vol. 40, pp. 1295–1299, Apr. 1989.
- [18] G. R. Srinivasan, H. H. K. Tang, and P. C. Murley, "Parameter-free, predictive modeling of single event upsets due to protons, neutrons, and pions in terrestrial cosmic rays," *IEEE Trans. Nucl. Sci.*, vol. 41, no. 6, pp. 2063–2070, Dec. 1994.
- [19] C. J. Gelderloos, R. J. Peterson, M. E. Nelson, and J. F. Ziegler, "Pion-induced soft upsets in 16 Mbit DRAM chips," *IEEE Trans. Nucl. Sci.*, vol. 44, no. 6, pp. 2237–2242, Dec. 1997.
- [20] R. J. Peterson, "Radiation-induced errors in memory chips," *Brazilian J. Physics*, vol. 33, no. 2, pp. 246–249, Jun. 2003.
- [21] S. Duzellier, D. Falguere, M. Tverskoy, E. Ivanov, R. Dufayel, and M.-C. Calvet, "SEU induced by pions in memories from different generations," *IEEE Trans. Nucl. Sci.*, vol. 48, no. 6, pp. 1960–1965, Dec. 2001.
- [22] H. H. K. Tang, "Nuclear physics of cosmic ray interaction with semiconductor materials: Particle-induced soft errors from a physicist's perspective," *IBM J. Res. and Development*, vol. 40, no. 1, pp. 91–108, Jan. 1996.
- [23] E. Normand, "Single event upset at ground level," *IEEE Trans. Nucl. Sci.*, vol. 43, no. 6, pp. 2742–2750, Dec. 1996.
- [24] J. F. Ziegler and H. Puchner, *SER-History, Trends, and Challenges: A Guide for Designing with Memory ICs*. Cypress Semiconductor Corporation, 2004.
- [25] S. Duzellier, R. Ecoffet, D. Falguere, T. Nuns, L. Guibert, W. Hajdas, and M. C. Calvert, "Low energy proton induced SEE in memories," *IEEE Trans. Nucl. Sci.*, vol. 44, no. 6, pp. 2306–2310, Dec. 1997.
- [26] E. L. Petersen, P. Shapiro, J. H. Adams Jr., and E. A. Burke, "Calculation of cosmic-ray induced soft upsets and scaling in VLSI devices," *IEEE Trans. Nucl. Sci.*, vol. 29, no. 6, pp. 2055–2063, Dec. 1982.

- [27] E. Petersen, “Single event analysis and prediction,” in *Proc. IEEE NSREC Short Course*, 1997.
- [28] R. H. Dennard, F. H. Gaenslen, H.-N. Yu, V. L. Rideout, E. Bassous, and A. R. LeBlanc, “Design of ion-implanted MOSFET’s with very small physical dimensions,” *IEEE J. Solid-State Circuits*, vol. SC-9, no. 5, pp. 256–268, Oct. 1974.
- [29] R. Baumann, “The impact of technology scaling on soft error rate performance and limits to the efficacy of error correction,” in *Dig. IEEE Int. Electron Devices Meeting*, 2002, pp. 329–332.
- [30] S. Gerardin, M. Bagatin, P. Rech, A. Cester, and A. Paccagnella, “Exploiting a low-energy accelerator to test commercial electronics with low-LET proton beams,” in *presented at the Radiation Effects Components and Systems Workshop*, Athens, Greece, 2006.
- [31] D. F. Heidel, K. P. Rodbell, P. Oldiges, M. S. Gordon, H. H. K. Tang, E. H. Cannon, and C. Plettner, “Single-event-upset critical charge measurements and modeling of 65 nm silicon-on-insulator latches and memory cells,” *IEEE Trans. Nucl. Sci.*, vol. 53, no. 6, pp. 3512–3517, Dec. 2006.
- [32] K. P. Rodbell, D. F. Heidel, H. H. K. Tang, M. S. Gordon, P. Oldiges, and C. E. Murray, “Low-energy proton-induced single-event-upsets in 65 nm node, silicon-on-insulator, latches and memory cells,” *IEEE Trans. Nucl. Sci.*, vol. 54, no. 6, pp. 2474–2479, Dec. 2007.
- [33] D. F. Heidel, P. W. Marshall, K. A. LaBel, J. R. Schwank, K. P. Rodbell, M. C. Hakey, M. D. Berg, P. E. Dodd, M. R. Friendlich, A. D. Phan, C. M. Seidleck, M. R. Shaneyfelt, and M. A. Xapsos, “Low energy proton single-event-upset test results on 65 nm SOI SRAM,” *IEEE Trans. Nucl. Sci.*, vol. 55, no. 6, pp. 3394–3400, Dec. 2008.
- [34] H. Kobayashi, N. Kawamoto, J. Kase, and K. Shiraishi, “Alpha particle and neutron-induced soft error rates and scaling trends in SRAM,” in *Proc. IEEE Int. Physics Rel. Symp.*, Apr. 2009, pp. 206–211.
- [35] H. Bichsel, D. E. Groom, and S. R. Klein, “Passage of particles through matter,” *Physics Lett. B*, vol. 667, no. 1-5, pp. 267–280, 2008.
- [36] *Stopping Powers and Ranges for Protons and Alpha Particles*. Bethesda, MD: International Commission on Radiation Units and Measurements, 1993, vol. ICRU report 49.
- [37] J. F. Ziegler, “Stopping of energetic light ions in elemental matter,” *J. Applied Physics*, vol. 85, no. 3, pp. 1249–1272, 1999.

- [38] P. Wojciechowski, P. Baumann, H. Daniel, F. J. Hartmann, C. Herrmann, M. Mhlbauer, W. Schott, A. Fuchs, P. Hauser, K. Lou, C. Petitjean, D. Taqqu, and F. Kottmann, “Measurement of the stopping power for  $\mu-$  and  $\mu+$  at energies between 3 keV and 100 keV,” *Hyperfine Interactions*, vol. 82, no. 1, pp. 127–131, 1993.
- [39] F. J. Hartmann, H. Daniel, C. Maierl, M. Mhlbauer, W. Schott, P. Wojciechowski, P. Hauser, C. Petitjean, D. Taqqu, F. Kottmann, and V. E. Markushin, “Experiments with low-energy muons,” *Hyperfine Interactions*, vol. 101-102, no. 1, pp. 623–632, 1996.
- [40] D. E. Groom, N. V. Mokhov, and S. I. Striganov, “Muon stopping power and range tables 10 MeV-100 TeV,” *Atomic Data and Nucl. Data Tables*, vol. 78, pp. 183–356, Jul. 2001.
- [41] F. Wrobel, “Use of nuclear codes for neutron-induced nuclear reactions in microelectronics,” in *IEEE Int. On-Line Testing Symp.*, Jul. 2005, pp. 82–86.
- [42] R. A. Reed, R. A. Weller, R. D. Schrimpf, M. H. Mendenhall, K. M. Warren, and L. W. Massengill, “Implications of nuclear reactions for single event effects test methods and analysis,” *IEEE Trans. Nucl. Sci.*, vol. 53, no. 6, pp. 3356–3362, Dec. 2006.
- [43] A. Wyttenbach, P. Baertschi, S. Bajo, J. Hadermann, K. Junker, S. Katcoff, E. A. Hermes, and H. S. Pruys, “Probabilities of muon induced nuclear reactions involving charged particle emission,” *J. Nucl. Physics A*, vol. 294, pp. 278–292, Jan. 1978.
- [44] B. Rossi, “Interpretation of cosmic-ray phenomena,” *Reviews Modern Physics*, vol. 20, no. 3, pp. 537–583, Jul. 1948.
- [45] P. K. Grieder, *Cosmic Rays at Earth*. Amsterdam: Elsevier, 2001.
- [46] ISO, *ISO 15390:2004: Space Environment (Natural and Artificial) - Galactic cosmic Ray Model*. Geneva, Switzerland: International Organization for Standardization, 2004.
- [47] G. D. Badhwar and P. M. O’Neill, “Galactic cosmic radiation model and its applications,” *Advances in Space Research*, vol. 17, no. 2, pp. 7–17, 1996.
- [48] A. J. Tylka, J. H. Adams Jr., P. R. Boberg, B. Brownstein, W. F. Dietrich, E. O. Flueckiger, E. L. Petersen, M. A. Shea, D. F. Smart, and E. C. Smith, “CREME96: A revision of the cosmic ray effects on micro-electronics code,” *IEEE Trans. Nucl. Sci.*, vol. 44, no. 6, pp. 2150–2160, Dec. 1997.
- [49] R. A. Nyymik, M. I. Panasyuk, T. I. Pervaja, and A. A. Suslov, “A model of galactic cosmic ray fluxes,” *Int. J. Radiation Applications and Instrumentation. Part D. Nucl. Tracks and Radiation Measurements*, vol. 20, no. 3, pp. 427–429, 1992.

- [50] J. A. V. Allen, C. E. McIlwain, and G. H. Ludwig, “Radiation observations with satellite 1958  $\epsilon$ ,” *J. Geophysical Res.*, vol. 64, no. 3, pp. 271–286, 1959.
- [51] D. M. Sawyer and J. I. Vette, “AP-8 trapped proton environment for solar maximum and solar minimum,” NASA National Space Science Data Center, Tech. Rep., Dec. 1976.
- [52] J. L. Barth, C. S. Dyer, and E. G. Stassinopoulos, “Space, atmospheric, and terrestrial radiation environments,” *IEEE Trans. Nucl. Sci.*, vol. 50, no. 3, pp. 466–482, Jun. 2003.
- [53] E. G. Stassinopoulos and J. P. Raymond, “The space radiation environment for electronics,” *Proc. of the IEEE*, vol. 76, no. 11, pp. 1423–1442, Nov. 1988.
- [54] E. G. Mullen, M. S. Gussenoven, K. Ray, and M. Violet, “A double-peaked inner radiation belt: cause and effect as seen on CRRES,” *IEEE Trans. Nucl. Sci.*, vol. 38, no. 6, pp. 1713–1718, Dec. 1991.
- [55] D. P. Bhattacharyya, M. Mukherjee, and D. Basu, “The spectra of cosmic pions and nucleons at low and high geomagnetic latitudes at the top of the atmosphere,” *Annalen der Physik*, vol. 487, no. 3, pp. 161–165, 1975.
- [56] P. Papini, C. Grimani, and S. A. Stephens, “An estimate of the secondary-proton spectrum at small atmospheric depths,” *Nuovo Cimento C Geophysics Space Physics C*, vol. 19, pp. 367–387, Jun. 1996.
- [57] T. Sanuki, “BESS data on primary cosmic rays and muons,” *Nucl. Physics B - Proceedings Supplements*, vol. 100, no. 1-3, pp. 121–123, 2001.
- [58] M. Boezio, V. Bonvicini, P. Schiavon, A. Vacchi, N. Zampa, D. Bergström, P. Carlson, T. Francke, P. Hansen, E. Mocchiutti, M. Suffert, M. Hof, J. Kremer, W. Menn, M. Simon, M. Ambriola, R. Bellotti, F. Cafagna, F. Ciacio, M. Circella, C. N. D. Marzo, N. Finetti, P. Papini, S. Piccardi, P. Spillantini, E. Vannuccini, S. Bartalucci, M. Ricci, M. Casolino, M. P. D. Pascale, A. Morselli, P. Picozza, R. Sparvoli, J. W. Mitchell, J. F. Ormes, S. A. Stephens, R. E. Streitmatter, U. Bravar, and S. J. Stochaj, “The cosmic-ray proton and helium spectra measured with the caprice98 balloon experiment,” *Astroparticle Physics*, vol. 19, no. 5, pp. 583–604, 2003.
- [59] K. O’Brien, W. Friedberg, H. H. Sauer, and D. F. Smart, “Atmospheric cosmic rays and solar energetic particles at aircraft altitudes,” *Environment Int.*, vol. 22, no. Supplement 1, pp. 9–44, 1996, the Natural Radiation Environment VI.
- [60] C. Hagmann, D. Lange, and D. Wright, “Monte Carlo simulation of proton-induced cosmic-ray cascades in the atmosphere,” Lawrence Livermore National Laboratory, Livermore, CA, Tech. Rep. UCRL-TM-229452, Feb. 2007.

- [61] L. Desorgher, E. O. Flückiger, M. Gurtner, M. R. Moser, and R. Bütkofer, “Atmocosmics: A Geant4 code for computing the interaction of cosmic rays with the earth’s atmosphere,” *Int. J. Modern Physics*, vol. 20, pp. 6802–6804, 2005.
- [62] M. Tueros and S. Sciutto, “TIERRAS: A package to simulate high energy cosmic ray showers underground, underwater and under-ice,” *Computer Physics Communications*, vol. 181, no. 2, pp. 380–392, 2010.
- [63] G. Carminati, M. Bazzotti, A. Margiotta, and M. Spurio, “Atmospheric muons from parametric formulas: a fast generator for neutrino telescopes (MUPAGE),” *Computer Physics Communications*, vol. 179, no. 12, pp. 915–923, 2008.
- [64] F. Lei, S. Clucas, C. Dyer, and P. Truscott, “An atmospheric radiation model based on response matrices generated by detailed Monte Carlo simulations of cosmic ray interactions,” *IEEE Trans. Nucl. Sci.*, vol. 51, no. 6, pp. 3442–3451, Dec. 2004.
- [65] F. Lei, A. Hands, S. Clucas, C. Dyer, and P. Truscott, “Improvements to and validations of the QinetiQ atmospheric radiation model (QARM),” in *Proc. IEEE Radiation Effects Components and Systems*, Sep. 2005, pp. D3–1–D3–8.
- [66] “EXPACS homepage.” [Online]. Available: <http://phits.jaea.go.jp/expacs/>
- [67] T. Sato, H. Yasuda, K. Niita, A. Endo, and L. Sihver, “Development of PARMA: PHITS-based analytical radiation model in the atmosphere,” *Radiation Res.*, vol. 170, no. 2, pp. 244–259, 2008.
- [68] M. S. Gordon, P. Goldhagen, K. P. R. T. H. Zabel, H. H. K. Tang, J. M. Clem, and P. Bailey, “Measurement of the flux and energy spectrum of cosmic-ray induced neutrons on the ground,” *IEEE Trans. Nucl. Sci.*, vol. 51, no. 6, pp. 3427–3434, Dec. 2004.
- [69] C.-R. R. Section, “Nagoya multi-directional muon telescope,” Solar-Terrestrial Environment Laboratory, Tech. Rep., 2002.
- [70] G. Brooke and A. W. Wolfendale, “The momentum spectrum of cosmic ray protons near sea level in the momentum range 0.6-150 gev/c,” *Proc. Physical Soc.*, vol. 83, 1964.
- [71] A. Z. Rosen, “Proton intensities at sea level and 9000 feet,” *Physical Review*, vol. 93, no. 1, pp. 211–214, Jan. 1954.
- [72] A. W. Wolfendale and G. D. Rochester, *Cosmic rays at ground level. Edited by A. W. Wolfendale.* Institute of Physics London, 1973.
- [73] C. E. Miller, J. E. Henderson, D. S. Potter, J. Todd, W. M. Sandstrom, G. R. Garrison, W. R. Davis, and F. M. Charbonnier, “The zenith angle dependence of cosmic-ray protons,” *Physical Review*, vol. 93, no. 3, pp. 590–595, Feb 1954.

- [74] G. N. Roesler Jr., “The zenith-angle distribution of stopping muons at sea level, and the response of a stopping-muon cosmic-ray detector,” Naval Academy, Annapolis, MD, Tech. Rep., May 1975.
- [75] O. C. Allkofer, K. Carstensen, and W. D. Dau, “The absolute cosmic ray muon spectrum at sea level,” *Physics Lett. B*, vol. 36, no. 4, pp. 425–427, 1971.
- [76] M. Boezio, V. Bonvicini, P. Schiavon, A. Vacchi, N. Zampa, D. Bergström, P. Carlson, T. Francke, P. Hansen, E. Mocchiutti, M. Suffert, M. Hof, J. Kremer, W. Menn, M. Simon, M. Ambriola, R. Bellotti, F. Cafagna, F. Ciacio, M. Circella, C. N. De Marzo, P. Papini, S. Piccardi, P. Spillantini, E. Vannuccini, S. Bartalucci, and M. Ricci, “Energy spectra of atmospheric muons measured with the CAPRICE98 balloon experiment,” *Physical Review D*, vol. 67, no. 7, p. 072003, Apr. 2003.
- [77] E. P. George and J. Evans, “Further observations of cosmic-ray events in nuclear emulsions exposed below ground,” *Proc. Physical Soc. A*, vol. 68, no. 9, p. 829, 1955.
- [78] H. E. Hall, Jr. and M. E. Richmond, “Stopping rate and energy loss of cosmic ray muons in sand,” *J. Geophysical Res.*, vol. 79, pp. 5503–5506, Dec. 1974.
- [79] G. Spannagel and E. L. Fireman, “Stopping rate of negative cosmic-ray muons near sea level,” *J. Geophysical Res.*, vol. 77, no. 28, pp. 5351–5359, 1972.
- [80] S.-I. Kaneko, T. Kubozoe, M. Okazaki, and M. Takahata, “Observations of slow particles and stars in nuclear emulsions exposed at 17 m.w.e. underground,” *J. Physical Soc. Japan*, vol. 10, pp. 600–+, Aug. 1955.
- [81] A. M. Short, “Mesons stopped underground,” *Proc. Physical Soc.*, vol. 81, no. 5, p. 841, 1963.
- [82] C. C. Foster, S. L. Casey, A. L. Johnson, P. Miesle, N. Sifri, A. H. Skees, and K. M. Murray, “Radiation effects test facility at the Indiana University Cyclotron Facility,” in *Int. Conf. Application Accelerators in Res. and Industry*, J. Duggan and I. L. Morgan, Eds., vol. 392, no. 1. AIP, 1997, pp. 1131–1134.
- [83] C. M. Castaneda, “Crocker Nuclear Laboratory (CNL) radiation effects measurement and test facility,” in *IEEE Radiation Effects Data Workshop*, 2001, pp. 77–81.
- [84] G. M. Marshall, “Muon beams and facilities at TRIUMF,” *Zeitschrift fur Physik C Particles and Fields*, vol. 56, pp. 226–+, Mar. 1992.
- [85] J. H. Brewer, “ $\mu$ +sr with surface muon beams,” *Hyperfine Interactions*, vol. 8, no. 4, pp. 831–834, Jan. 1981.
- [86] J. Doornbos, private communication, 1983.

- [87] H. Paul, “Stopping power for light ions.” [Online]. Available: <http://www.exphys.uni-linz.ac.at/Stopping/>
- [88] H. Paul and A. Schinner, “An empirical approach to the stopping power of solids and gases for ions from  ${}^3\text{Li}$  to  ${}^{18}\text{Ar}$  – part II,” *Nucl. Instrum. Methods Physics Res. B*, vol. 195, pp. 166–174, 2002.
- [89] J. F. Zeigler, M. D. Zeigler, and J. P. Biersack, “Stopping and range of ions in matter SRIM.” [Online]. Available: <http://www.srim.org/>
- [90] J. J. Suter, J. M. C. J. R. Norton, D. Y. Kusnierkiewicz, and A. M. Koehler, “Simulation of low-earth-orbit radiation environments with a 5 to 120 MeV proton cyclotron beam using a proton beam modulator,” *IEEE Trans. Nucl. Sci.*, vol. 34, no. 4, pp. 1070–1075, Aug. 1987.
- [91] E. W. Cascio and S. Sarkar, “A solar flare simulation wheel for the radiation test beamline at the Francis H. Burr Proton Therapy Center,” *IEEE Trans. Nucl. Sci.*, vol. 55, no. 6, pp. 3428–3434, Dec. 2008.
- [92] J. R. Letaw, R. Silberberg, and C. H. Tsao, “Proton-nucleus total inelastic cross sections - an empirical formula for E greater than 10 MeV,” *Astrophysical J. Supplement Series*, vol. 51, pp. 271–275, Mar. 1983.
- [93] W. J. Stapor, J. P. Meyers, J. B. Langworthy, and E. L. Petersen, “Two parameter bendel model calculations for predicting proton induced upset,” *IEEE Trans. Nucl. Sci.*, vol. 37, no. 6, pp. 1966–1973, Dec. 1990.
- [94] Y. Cao, T. Sato, M. Orshansky, D. Sylvester, and C. Hu, “New paradigm of predictive mosfet and interconnect modeling for early circuit simulation,” in *Proc. IEEE Custom Integrated Circuits Conf.*, 2000, pp. 201–204.
- [95] W. Zhao and Y. Cao, “New generation of predictive technology model for sub-45 nm early design exploration,” *IEEE Trans. Electron Devices*, vol. 53, no. 11, pp. 2816–2823, Nov. 2006.
- [96] “Predictive technology model (ptm),” [Online] Available: <http://ptm.asu.edu>.
- [97] Semiconductor Industry Association (SIA), “International roadmap for semiconductors 2010 update,” 2010. [Online]. Available: <http://www.itrs.net>
- [98] J. S. Kauppila, A. L. Sternberg, M. L. Alles, A. M. Francis, J. Holmes, O. A. Amusan, and L. W. Massengill, “A bias-dependent single-event compact model implemented into BSIM4 and a 90 nm CMOS process design kit,” *IEEE Trans. Nucl. Sci.*, vol. 56, pp. 3152–3157, Dec. 2009.
- [99] R. Naseer, Y. Boughassoul, J. Draper, S. DasGupta, and A. Witulski, “Critical charge characterization for soft error rate modeling in 90 nm SRAM,” in *IEEE Symp. Circuits and Systems*, May 2007, pp. 1879–1882.

- [100] T. D. Loveless, M. L. Alles, D. R. Ball, K. M. Warren, and L. W. Massengill, “Parametric variability affecting 45 nm SOI SRAM single event upset cross-sections,” *IEEE Trans. Nucl. Sci.*, vol. 57, no. 6, pp. 3228–3233, Dec. 2010.
- [101] R. A. Weller, M. H. Mendenhall, R. A. Reed, R. D. Schrimpf, K. M. Warren, B. D. Sierawski, and L. W. Massengill, “Monte Carlo simulation of single event effects,” *IEEE Trans. Nucl. Sci.*, vol. 57, no. 4, pp. 1726–1746, Aug. 2010.
- [102] S. Agostinelli *et al.*, “G4—a simulation toolkit,” *Nucl. Instrum. Methods Physics Res. A*, vol. 506, no. 3, pp. 250–303, 2003.
- [103] M. H. Mendenhall and R. A. Weller, “An algorithm for computing screened coulomb scattering in Geant4,” *Nucl. Instrum. Methods Physics Res. B*, vol. 227, no. 3, pp. 420–430, 2005.
- [104] A. S. Kobayashi, D. R. Ball, K. M. Warren, R. A. Reed, N. Haddad, M. H. Mendenhall, R. D. Schrimpf, and R. A. Weller, “The effect of metallization layers on single event susceptibility,” *IEEE Trans. Nucl. Sci.*, vol. 52, no. 6, pp. 2189–2193, Dec. 2005.
- [105] K. M. Warren, B. D. Sierawski, R. A. Weller, R. A. Reed, M. H. Mendenhall, J. A. Pellish, R. D. Schrimpf, L. W. Massengill, M. E. Porter, and J. D. Wilkinson, “Predicting thermal neutron-induced soft errors in static memories using TCAD and physics-based Monte Carlo simulation tools,” *IEEE Electron Device Lett.*, vol. 28, no. 2, pp. 180–182, Feb. 2007.
- [106] Y.-K. Choi, K. Asano, N. Lindert, V. Subramanian, T.-J. King, J. Bokor, and C. Hu, “Ultrathin-body SOI MOSFET for deep-sub-tenth micron era,” *IEEE Electron Device Lett.*, vol. 21, no. 5, pp. 254–255, May 2000.
- [107] P. Oldiges, R. Dennard, D. Heidel, T. Ning, K. Rodbell, H. Tang, M. Gordon, and L. Wissel, “Technologies to further reduce soft error susceptibility in SOI,” in *IEEE Int. Electron Devices Meeting*, Dec. 2009, pp. 1–4.
- [108] W. Xusheng, Z. Shengdong, M. Chan, and P. Chan, “Design of sub-50 nm ultrathin-body (UTB) SOI MOSFETs with raised S/D,” in *IEEE Conf. Electron Devices and Solid-State Circuits*, Dec. 2003, pp. 251–254.
- [109] H. Kawasaki, V. S. Basker, T. Yamashita, C.-H. Lin, Y. Zhu, J. Faltermeier, S. Schmitz, J. Cummings, S. Kanakasabapathy, H. Adhikari, H. Jagannathan, A. Kumar, K. Maitra, J. Wang, C.-C. Yeh, C. Wang, M. Khater, M. Guillorn, N. Fuller, J. Chang, L. Chang, R. Muralidhar, A. Yagishita, R. Miller, Q. Ouyang, Y. Zhang, V. K. Paruchuri, H. Bu, B. Doris, M. Takayanagi, W. Haensch, D. McHerron, J. O'Neill, and K. Ishimaru, “Challenges and solutions of FinFET integration in an SRAM cell and a logic circuit for 22 nm node and beyond,” in *IEEE Int. Electron Devices Meeting*, Dec. 2009, pp. 1–4.